ABSTRACT

**VARIABLE RESOLUTION SMOOTHED PARTICLE
HYDRODYNAMICS SCHEMES FOR 2-D AND 3-D VISCOUS FLOWS**

by
Francesco Ricci

Smoothed Particle Hydrodynamics (SPH) is a Lagrangian particle-based method for the numerical solution of the partial differential equations that govern the motion of fluids. The main aim of this thesis work is to better enable the applicability of SPH to problems involving multi-scale fluid dynamics. In the first part of the thesis, the capability of the SPH method to simulate three-dimensional isotropic turbulence is investigated with a detailed comparison of Lagrangian and Eulerian SPH formulations. The main reason for this first investigation is to provide an assessment of the error introduced by the particle disorder on the SPH discrete operators when being purely Lagrangian. When the free decay of isotropic turbulence in a triple periodic box is studied, the Eulerian SPH formulation achieves a very good agreement with other well validated reference solutions, whereas Lagrangian SPH yields an inaccurate prediction of turbulent energy spectra. When considering linearly forced isotropic turbulence, the use of a Godunov-type SPH scheme becomes essential for the achievement of a stable solution. The efficacy of the particle shifting technique applied to turbulent SPH flows is also studied in this part of the thesis and numerical findings indicate that corrective terms derived from the arbitrary Lagrangian–Eulerian theory are essential for a proper estimation of turbulence characteristics. Subsequently, numerical analyses of a decaying isotropic turbulent flow are carried out for the first time using SPH schemes based on high-order kernels. A dramatic increase in the accuracy of the results is observed when high-order SPH is employed, especially for the description of the vorticity dynamics.

Motivated by the findings of the computational investigations above, the second part of this thesis focuses on the implementation and testing of a novel SPH variable-resolution algorithm. A domain-decomposition approach is adopted to partition the computational domain into regions having different particle resolutions. Each numerical sub-problem is then closed by appending buffer regions to every sub-domain, and populating these regions with particles whose physical quantities are obtained by means of interpolations over adjacent sub-domains. These interpolations are carried out using a second-order kernel correction procedure to ensure the proper consistency and accuracy of the interpolation process. The mass transfer among sub-domains is modeled by evaluating the Eulerian mass flux at the domain boundaries. Particles that belong to a specific zone are created/destroyed in the buffer regions and do not interact with fluid particles that belong to a different resolution zone.

The algorithm is implemented in the DualSPhysics open-source code [62] and optimized thanks to DualSPHysics' parallel framework. The algorithm is tested on a series of different fluid dynamics problems: a 2-D hydrostatic tank case, a flow past cylinder for different values of the Reynolds number, a flow past an oscillating cylinder in the cross-flow direction, and the propagation of regular waves across a rectangular tank. The present algorithm is able to simulate efficiently fluid dynamics problems characterized by a wide range of spatial scales, achieving a ratio between the coarsest and the finest resolution up to a factor equal to 256.

The investigation is then extended to 3-D fluid dynamics problems, such as the flow past a sphere with a Reynolds Number equal to 300 and 500, for which a SPH solution using a uniform resolution is unfeasible due to the high computational cost, showing a good agreement between the results obtained with the variable-resolution algorithm herein presented and relevant numerical investigations in the literature.

The work is then concluded with the simulation and validation of a 3-D dam-breaking flow impacting a cubic obstacle.

VARIABLE RESOLUTION SMOOTHED PARTICLE HYDRODYNAMICS SCHEMES FOR 2-D AND 3-D VISCOUS FLOWS

by
Francesco Ricci

A Dissertation
Submitted to the Faculty of
New Jersey Institute of Technology
in Partial Fulfillment of the Requirements for the Degree of
Doctor of Philosophy in Mechanical Engineering

Department of Mechanical and Industrial Engineering

August 2023

VARIABLE RESOLUTION SMOOTHED PARTICLE
HYDRODYNAMICS SCHEMES FOR 2-D AND 3-D VISCOUS FLOWS

Francesco Ricci

BIOGRAPHICAL SKETCH

Author: Francesco Ricci

Degree: Doctor of Philosophy

Date: August 2023

Undergraduate and Graduate Education:

- Doctor of Philosophy in Mechanical Engineering,
  New Jersey Institute of Technology, Newark, NJ, US, 2023

- Master of Science in Computational Fluid Dynamics,
  Cranfield University, Cranfield,UK, 2018

- Master of Science in Mechanical Engineering,
  Politecnico di Bari, Bari, Italy 2016

- Bachelor of Science in Mechanical Engineering,
  Politecnico di Bari, Bari, Italy, 2013

Major: Mechanical Engineering

Presentations and Publications:

F., P. A.S.F. Silva, P. Tsoutsanis, . F. Antoniadis, "Hovering rotor solutions by high-order methods on unstructured grids,," *Aerospace Science and Technology*, Volume 97, 2020.

F. Ricci, R. Vacondio, A. Tafuni; Direct numerical simulation of three-dimensional isotropic turbulence with smoothed particle hydrodynamics." *Physics of Fluids*, 2023; 35 (6): 065148.

F. Ricci, R. Vacondio and A. Tafuni, "A variable resolution SPH scheme based on independent domains coupling," *Proceedings of the 17th SPHERIC International Workshop*, Rhodes, 2023.

F. Ricci, R. Vacondio and . Tafuni, "High-order SPH schemes for DNS of turbulent flows," *Proceedings of the 2022 SPHERIC International Workshop*, Catania, 2022.

To my grandfather and my nephew

ACKNOWLEDGMENT

TABLE OF CONTENTS

Chapter   **Page**

LIST OF TABLES

LIST OF FIGURES

LIST OF FIGURES
(Continued)

Figure   **Page**

Figure   **Page**

LIST OF FIGURES
(Continued)

Figure   **Page**

CHAPTER 1

INTRODUCTION

1.1 Background and Motivation

The equations that model the motion of an incompressible viscous flow, i.e., the Navier-Stokes equations, are characterized by non-linear terms that make their mathematical treatment still an open challenge 100 years after their first derivation. Analytical solutions have been developed for specific cases by linearizing terms or reducing dimensionality, providing qualitative descriptions of flow in simple geometries. However, in order to obtain quantitative results, solving the Navier-Stokes equations numerically is crucial.

Computational Fluid Dynamics (CFD) is the computational science encompassing all numerical methods used to analyze fluid motion and serves two main purposes. From a scientific perspective, it helps better understand complex phenomena like turbulence, multiphase flows, and flow-induced noise. In industry, it reduces costs associated with experimental aspects of the design process by narrowing the range of variables in experimental runs, optimizing designs, and shortening the time from conceptual design to production in various sectors such as automotive, aerospace, and energy.

The earliest but still most popular numerical methods in CFD are mesh-based methods such as the Finite Difference Method (FDM) [92], the Finite Volume Method (FVM) [129], and the Finite Element Method (FEM) [284]. In mesh-based methods, the physical domain is discretized by computational nodes, which are topologically connected.

Generating the computational grid is a complex and crucial part of the numerical computation workflow. It is often the most time-consuming task and demands

expertise to ensure the proper placement of computational nodes, considering the physics of specific phenomena while maintaining grid quality. High-aspect ratio or entangled grid elements can negatively impact the accuracy and stability of the numerical solution, particularly in the presence of intricate geometrical features [73].

Before applying the discretization specific to a particular numerical technique, the first choice concern the kinematic description of the continuum. Usually, two different formulations are employed [64]: in the Eulerian description, the computational nodes remain fixed in space and time, and convective terms are added into the governing equation, while the continuum moves and deforms with respect to the mesh, as opposed to the Lagrangian description, where each computational element is associated to a material particle thus following it during its motion. Both formulations have their advantages and disadvantages, depending on the particular physics of the problem: for fluid dynamics flows, the Eulerian description is usually preferred because it is conceptually simpler. However, it is generally unable to describe accurately moving interfaces. The Lagrangian formulation is preferred when dealing with structural mechanics because it is implicitly able to track interfaces and deal with a time-dependent stress-strain relationship. However, as opposed to the Eulerian description, when there is large material deformation, the motion of the computational nodes can result in distorted or entangled elements that can deteriorate the accuracy and the convergence of the numerical methods.

Due to the successes in predicting aerodynamical flows, the CFD technique has also been extended to fluid-structure interaction (FSI) problems, where movable or deforming objects interact with surrounding fluid flows. This class of problems is characterized by strong non-linearities and a multi-physics nature, making the numerical solutions in a single mathematical framework rather challenging. The range of applications of FSI problems spans different engineering areas, including aeroelas-

ticity [104], bio-medical flows [96], biological flows [241], structural engineering [124], coastal and marine applications [278] among the others.

Many different CFD methods have been proposed to tackle FSI problems. Among those, the two most popular techniques are Arbitrary Lagrangian-Eulerian (ALE) [93] and the Immerse Boundary Method (IBM)[193].

The idea behind the Arbitrary-Lagrangian-Eulerian (ALE) description is to retain the advantages of both the Eulerian and the Lagrangian formulation while mitigating their drawbacks. Usually, in ALE methods, a body-fitted grid discretizes the solid domain, while an Eulerian description is employed for the fluid far region. Instead, near the interface, an arbitrary velocity is imposed on the mesh to avoid excessive mesh distortion, and convective fluxes account for this arbitrary motion in the governing equations. However, in the presence of large displacement, the re-meshing and remapping process is unavoidable, along with the associated computational cost and the challenges in remapping the solution over the new mesh, which can deteriorate the accuracy of the numerical solution.

In the Immersed Boundary Method, non-conformal meshes are used to tessellate the fluid and the solid region, which are usually described using a different kinematic description [159]. The ability to employ overlapping grids, avoid ALE methods' computationally cumbersome re-meshing process and greatly simplify the grid generation process. The coupling between the non-conformal meshing is usually achieved by adding a local volumetric force into the governing equations of the fluid part, using a smoothing function to redistribute the effect of the interface over a range of computational nodes. However, different strategies have been proposed [87]. Another coupling approach is the Cut-Cell Finite-Volume approach [275], which doesn't use a volumetric forcing and has better mass and momentum conservation properties. Nevertheless, two main drawbacks characterize the IBM: the first one, as discussed in [25], concerns the "added-mass" effect when dealing with a high

fluid-to-solid density ratio; the second one regards the simulation of a high Reynolds number flows, for which a mesh refinement procedure is required in order to ensure an adequate resolution near the solid boundaries [254].

Another class of problems that involve moving interfaces is free-surface and multiphase flows problems. In this case, two main strategies are used in mesh-based methods, front-capturing and front-tracking approaches [243].

The Volume of Fluid (VOF) technique [94] is the most popular front-capturing method. In the VOF, the interface between two fluids is represented by a color function, which value is based on the volume fraction of each phase in a particular computational element. The method is composed of two steps: in the first one, the interface is reconstructed from the value of the color function in each cell. Early studies used a Simple Line Interface Construction (SLIC) [181, 94], representing the interface by segments aligned with the mesh. Although it is very simple, this method leads to large interface smearing. More accurate approaches, such as the Piecewise Linear Interface Construction (PLIC) [207], significantly improve the method's accuracy. The color function is advected using the velocity field in the second part of the approach. Despite the mathematical formulation ensuring good conservation properties, the discontinuous reconstruction can lead to instabilities in the presence of high-curvature interfaces.

Another approach is the Level-Set method [190], in which the interface is represented by a smooth function that moves according to an advection equation. The advantage of the Level-set method is that with respect to the VOF, the function is smooth; however, it has a worse conservation mass property with respect to the former method.

In front-tracking techniques [244], instead, the boundaries between different phases are represented by a set of marker points that are connected and move along with the fluid. The drawbacks of these methods are the additional data structure to

describe the front and the explicit treatment that require the topology change of the interface.

Opposed to grid-based methods, in meshless-based methods the approximation of the governing equations is built upon a set of computational nodes for which grid connectivity is not specified. Among them, there are the Smoothed Particle Hydrodynamics (SPH) method [80], the Meshless local Petrov-Galerkin method [12], the Diffuse Element Method [180], the Element-Free Galerkin methods [19], and the Moving-particle semi-implicit method [116].

The SPH method is arguably the most popular for simulating incompressible viscous flows. In the SPH method, the Navier-Stokes equations are approximated upon a set of discrete particles that carry the physical properties of the fluid. The interpolation is based on the convolution with a kernel smoothing function. One of the advantages of the SPH method is its robustness; in fact, as demonstrated in [24], the SPH formulation is consistent with a variational approach, ensuring conservation of all relevant physical quantities. Moreover, due to the Lagrangian formulation, the fluid properties are advected exactly and able to implicitly describe interfaces, suach as free-surface.

The SPH rEsearch and Engineering International Community (SPHERIC) is an international organization that groups the community of SPH researcher and industrial practitioners. The main objective of SPHERIC is to steer the research focus on the SPH method. In fact, the steering committee has identified five different aspects of SPH that need to be addressed in order to encourage the widespread adoption of the method for CFD study. The SPH Grand Challenges are [245]: Convergence, consistency and stability, Boundary conditions, Adaptivity, Coupling to other models, Applicability to industry. One topic that has been poorly addressed by the SPH research and limits the range of applicability and the fidelity of the method concern the simulation of turbulent flows. In this work is studied the issue of the

inclusion of turbulence effects in the SPH method. In particular, a major focus is given to the relationship between turbulence modeling and the issue of adaptivity within the SPH method.

1.2   Aim and Objectives

The main goal of the present dissertation is to extend the range of applicability of the Smoothed Particle Hydrodynamics method, with a focus on turbulent flows. To this end, the present objectives are set:

1. Gain insight into the performance of the SPH method in the computation of turbulent flows.

2. Analyze the effect of the discretization error due to the discrete operator, the density diffusion term and the particle shifting on the numerical computation of isotropic turbulence.

3. Assess the performance of high-order kernel scheme in the numerical solution of isotropic turbulence

4. Develop a novel and highly-efficient variable-resolution approach for turbulence problems where high local resolution is required.

5. Implement the new algorithm in the DualSPHysics open-source code and validating across different test cases.

6. Extension and validation of the approach to the numerical computation of three-dimensional flows.

1.3   Structure of the Dissertation

This dissertation is structured as follows:

1. In Chapter 1 is presented an overview of the numerical approaches for the computation of flows characterized by moving interfaces

2. Chapter 2 present a literature review over the state of the art of the SPH method with a particular focus over the turbulence and its modeling within the SPH method and the issue of adaptivity.

3. Chapter 3 present the mathematical basis of the SPH along with the numerical technique adopted in this work.

4. In Chapter 4 the numerical computation of homogenous isotropic turbulence within the SPH method is adressed. The effect of the discrete operator over the accuracy is studied, and the effect of a Density Diffusion Term and the Particle Shifting Technique is assessed. The numerical simulation results with high-order SPH schemes of decaying isotropic turbulence are presented.

5. In Chapter 5 a novel highly-efficient variable-resolution algorithm is proposed. A set of validation test case are simulated and the results are compared against reference solution available in literature.

6. Chapter 6 describe the extension and the validation of the novel approach to the computation of three-dimensional flows.

CHAPTER 2

LITERATURE REVIEW

2.1 General Overview

The basic concept behind the Smoothed Particle Hydrodynamics method is to represent a fluid with material particles that carry extensive quantities, such as the mass and momentum, and intensive properties, such as velocity or density. From a mathematical point of view, these particles are computational nodes in which the underlying governing equations are discretized by applying two distinct mathematical operators: first, the scalar (or vector) field is averaged in space on a continuous level through a weighting function, then it is approximated by discrete Riemann sums over a set of particles. The mathematical formulation for the SPH method will be presented in detail in Chapter 3.

The advantages of the SPH method stem from its mesh-less Lagrangian nature. The absence of grid connectivity between particles confers to the method the natural ability to describe arbitrarily complex moving interfaces and simultaneously reduce the cost associated with the mesh generation. Moreover, due to the Lagrangian formulation, the fluid properties are advected without any diffusion, which makes the method particularly suitable for physical phenomena with short-time scale dynamics. Another attractive feature of the method is its robustness: as demonstrated by many authors [23, 24, 184], the SPH formulation is consistent with a variational formalism of the equations of motion, which results in the conservation of momentum and angular momentum, while the mass conservation is implicitly ensured because the it is associated with the computational nodes.

The SPH method was proposed originally for astrophysical application [80, 143], and since then has been widely used to study the dynamics of binary star system

[11], star formation [234], merging of white dwarfs [88, 276] and neutron star [183], among other studies. Open-source code such as the SWIFT [216] and the GADGET-2 code [233] (based on the TreeSPH code [91]) have been able, due to a massive parallelization, to handle more than 10^{10} particles in a single simulation.

However, due to its simple but robust and versatile formulation that can easily incorporate different physics, the SPH method has been then extended to different areas of engineering, for example, magnetohydrodynamics [197], biomedical flows [239, 227, 217, 172], heat transfer [40, 211, 41], high-velocity impact [101, 39, 146], crack propagation [17].

Among these different fields, it is in the computation of incompressible fluid flows where the SPH method has found its primary application, especially in the case of the presence of free-surface, which arise in many coastal and ocean engineering applications [144]. Apart from the natural advantages already mentioned above, together with the implicit verification of the free-surface boundary condition, as discussed in [42, 43], in the last two decades, important developments have been made to extend the SPH method to this general class of viscous flow. Among them:

- Improvement in the mathematical formulation of the method, addressing different sources of instability, e.g., tensile and pairing instability, high-frequency oscillation in the density field for the weakly-compressible SPH method, and techniques to improve the isotropic distribution of particles.

- Progress in the imposition of boundary conditions, especially for introducing inlet/outlet region and solid boundaries typically missing in astrophysical applications.

- The advent of Graphics Processing Units (GPUs) as the predominant technology for High-Performance Computing (HPC) has facilitated a seamless adaptation to the particle-based formulation inherent in the Smoothed Particle Hydrodynamics method.

The next section will review the state-of-the-art and the main application of the SPH method for incompressible viscous flow.

2.2 Incompressible Viscous Flow with SPH

2.2.1 General overview and applications

The first application of the SPH to free-surface flows was presented in Monaghan [165], where the key ingredient introduced was enforcing a weakly-compressible formulation through a stiff equation of state. The speed of sound was sufficiently large to enforce a near-constant density field while not excessively constraining the time step. One clear evident advantage was the implicit treatment of the free-surface, which didn't require the imposition of any explicit boundary condition, different from other computational techniques. Another important aspect of that work was the first attempt at modeling the solid boundary. The same author extended the SPH method to the computation of multi-phase flows [163].

Another landmark work was presented in Colagrossi and Ladrini[45], where the numerical simulation of interfacial flows with low-density ratio was tackled. Moreover, a first attempt was proposed to resolve the spurious oscillation that afflicted the weakly-compressible formulation based on the periodic re-initialization of the density field through a Moving Least Square filtering.

Since these early works, in the last two decades, the SPH method has made significant progress, and many review articles [167, 259, 280, 141, 245] and specialized monographs [138, 256] highlight its relevance in the field of numerical methods for CFD.

In particular, SPH has found its primary application in coastal and marine engineering applications, characterized by highly complex phenomena. As an example of a complex coastal applications, the SPH method has been assessed against experimental and analytical data in Altomare et al.[3] to study the interaction between periodic waves and an armored structure composed of cubic blocks with complex geometry. Furthermore, the SPH open-source code DualSPHysics has been used to study [2] the impact of an irregular wave train on two realistic coastal structures,

namely the Zeebrugge and Blankenberge port, and the numerical results have been compared against the experimental ones in terms of wave elevation and forces exerted on the structures. A similar study has been carried out in Altomare et al.[4] to study the structural failure of a bridge due to the impact loading during a violent storm. The maturity of the SPH method with respect to a well-established mesh-based method has been demonstrated in Gonzalez et al. [82] for predicting the wave propagation and collision of regular waves against a coastal structure. Furthermore, additional studies have focused on evaluating the impact of a tsunami wave on bridge piers [264, 263].

An additional application explored using the SPH method involves liquid sloshing in moving tanks. This phenomenon entails the intense interaction between the liquid interface and solid boundaries, particularly when dealing with low-filling ratios. Examples of two-dimensional studies within a SPH framework have been presented in [229, 218, 106, 56, 31] where both translational and rotational excitations are simulated. The ability of the SPH method to predict long-duration sloshing in rectangular tanks with a low-filling ratio has been assessed in Green et al. [83], while examples of three-dimensional studies have been presented in Green et al.[86] and in You et al. [277]. Multi-phase formulations have been used in [90, 153] to analyze the effect of air-cushioning in liquid sloshing.

In recent years, SPH modeling has been applied to study offshore renewable energy devices. The simulation of a real-scale oscillating water column (OWC), a device that exploits the change of the water level due to the wave's motion to generate energy, has been presented in Crespo et al. [47], where the SPH model has been validated against experimental results. Similar studies have also been proposed for oscillating wave surge converters in [151, 29, 282].

The SPH method can resolve FSI problems with deformable structures with either a monolithic or a partitioned approach. The former takes advantage of the

versatility of the SPH formulation, and both the fluid and the solid phase are solved using an SPH discretization. In the latter, the fluid and the solid phase are solved using different numerical techiniques, that are coupled in time using an appropriate coupling approach.

As noted in O'Connor et al. [191], the SPH modeling of a solid structure must face three different issues: inconsistency of the SPH interpolation, tensile instability, and rank deficiency. The first issue is resolved using the normalization technique [202]. The second issue has been addressed or stabilizing the solution by adding dissipative terms in the momentum equation [6, 201, 186], or using a Total-Lagrangian formulation [18] where an undeformed reference configuration is used. Using this approach, however, the SPH method encounter issue due to zero-energy modes due to the collocation nature of the method. To solve this issue, in [191, 279] is used the hourglass control proposed in Ganzenmuller[77]. Another important aspect regards the fluid-structure coupling: in the fluid-structure acceleration approach [186, 201, 111], the continuity of the normal stress at the interface is guaranteed by considering solid particles as moving wall boundary; meanwhile, in the Pressure Integration [6], the acceleration on the solid structure exerted by the fluid is calculated with a surface integration over the interface, with the pressure obtained with an SPH interpolation.

Regarding the partitioned approach for the FSI problem, the SPH method has been coupled with FEM methods [74, 130, 271], Discrete Element Method (DEM) [270, 176], and the Distributed Contact Discrete Element Method (DCDEM) [30]. The challenges associated with the coupling with other methods are a consistent coupling that ensures that no energy is being injected at the interface between the fluid and the solid phase due to an inaccurate transfer of information.

Recently, have been also proposed coupling of the SPH method with the FVM [154]. The idea behind this approach is to take advantage of the efficiency of the FVM discretization to accurately resolve the near-wall regions, while employing the SPH

approach where the flow is characterized by complex moving interface,e.g., free-surface or moving objects.

As previously discussed, one of the primary limitations of the Smoothed Particle Hydrodynamics (SPH) method, which initially hindered its broad application in engineering, is its high computational cost. This is due to a larger computational stencil (typically on the order of 30+ and 300+ particles for 2-D and 3-D simulations, respectively) compared to Finite Volume Method (FVM) or Finite Element Method (FEM). However, with the rise of massively parallel architectures, such as those based on Graphics Processing Units (GPUs), numerous in-house or open-source ([62, 21, 34]) codes have rapidly developed.

Originally, GPUs were utilized in graphics applications, such as image/video processing and video gaming. Their architecture is built around the Streaming Multiprocessor unit, composed of several Arithmetic Logic Units (also known as CUDA cores). The latest generations of GPUs have hundreds of streaming multiprocessors, enabling them to perform thousands of arithmetic operations simultaneously.

The SPH method, particularly in its Weakly-Compressible formulation utilizing an explicit time-scheme, is especially suited for such architectures. This is due to the high arithmetic intensity of particle-particle interaction calculations which, as noted in Dominguez et al. [59], generally represents the most computationally expensive operation in an SPH simulation.

In the SPH method, the computational stencil is computed through the creation of a neighbor list. Dominguez et al. [59] have discussed the primary techniques for creating this neighbor list, emphasizing the importance of particle reordering to ensure optimal coalesced memory access. Additionally, in Dominguez et al.[61], various optimizations are detailed to further enhance the efficiency of a GPU implementation of an SPH model.

2.2.2 Convergence and accuracy of SPH method

The discretization error in the SPH method is composed of two contributions: the first one is due to the smoothing procedure that, for a conventional smoothing kernel function, has an order of $\mathcal{O}(h^2)$, where h is the smoothing length. The second source of error is due to the discrete approximation and is a function of both the smoothing length and the number of neighbors N_b included in the kernel support.

Monaghan [164] conjectured that the SPH method because the discrete pressure gradient tends to arrange the particles in a glass-like configuration, presents more favorable convergence properties than Monte-Carlo methods. In Zhu et al. [283] is noted that to maintain constant the rate of convergence, one must have $h \to 0$, $N_b \to \infty$ and $N \to \infty$ simultaneously, and propose a power-law to relate h and N_b to the total number of particles N in the computational domain for a typical 2nd order smoothing kernel function as:

$$h \propto N^{-1/6}, N_b \propto N^{0.5} \tag{2.1}$$

The same conclusions were reached in [199], where the discretization error of a 1D SPH approximation was analyzed through a second Euler-McLaurin summation formula. The immediate consequence of these findings is that to preserve the second-order accuracy, the computational stencil, which is already large in comparison to mesh-based methods, must grow as h shrinks, increasing the computational cost.

Besides, early SPH practitioners run into the so-called "pairing instability" over a certain threshold of neighbors. As demonstrated in Dehnen and Aly[55], this phenomenon is caused by negative values in the Fourier transform of the smoothing kernel. For this reason, Wendland kernels [265] have become the standard in the SPH method.

Another widespread technique to decrease the inaccuracies due to a disorder distribution is the Particle Shifting Technique (PST) [136], which aims to restore a

more regular distribution by moving the position of the particles, typically modeling the displacement with a Fick's law based on the concentration gradient. A similar approach has also been proposed within the SPH-ALE formulation [187].

The PST has soon become a cornerstone when dealing with incompressible viscous flows, although it requires careful treatment in the presence of a free surface due to the zero-th error introduced in the SPH gradient operator by the truncated support. In this case, the formulation of the PST is usually modified by eliminating the normal component to the free surface of the shifting vector [136]. Different procedures have been proposed in order to identify the fluid particles that belong to the free-surface: in the method proposed in Lee et al.[125], the free-surface particles are identified through the value of the divergence of the position vector. A more computationally costly but accurate approach has been proposed in Marrone et al. [152], where the minimum value of the eigenvalues of the renormalization matrix [202] and an additional procedure, based on scanning the "umbrella-shaped" regions are used to determine the particles belonging to the free-surface. Recently, different works have addressed the inconsistency introduced at the free-surface from the shifting algorithm [109, 262, 145, 120].

Additionally, iterative explicit and implicit shifting algorithms [203] have also been proposed to ensure a better regularization of the particle distribution.

Another aspect closely related to the convergence property is the consistency of the SPH method, in particular in the presence of boundaries that truncate the support domain of the smoothing kernel. In that case, neither the zero nor the first-order consistency is ensured. Different numerical techniques have been proposed to correct the inconsistency: approach based on the renormalization matrix [202, 101], Moving Least-Square schemes [58], the Corrective Smoothed Particle Hydrodynamics Method (CSPH) [36], the Finite Particle Method [140] (FPM), the modified Smoothed Particle Hydrodynamics method (MSPH) [16].

The downside of these approaches is the computational cost associated with the solution of the linear system, which increases steeply with the dimensionality and the order of consistency required. Besides, most of these methods break the symmetricity of the particle interaction, with the loss of the conservation properties of the method, although some authors [185] suggest that this property can be relaxed.

Different strategies have been proposed in the last years to achieve a higher convergence rate. Using a Riemann-SPH scheme, in Avesani et al. [13] has been proposed a WENO-reconstruction where the polynomials are obtained through an MLS interpolation. The reconstruction stencils are defined by partitioning the support domain of the kernel into different sectors. This approach has been furtherly improved in Antona et al. [7], where the FPM method is used in place of the MLS scheme. This scheme has also been extended in Avesani et al. [14] to include a high-order space-time reconstruction with an ADER-WENO-SPH scheme. The drawbacks of this approach are that the convergence rate is still limited by the SPH approximation in the particle interaction and the computational cost associated with the MLS reconstruction that requires a matrix inversion for each stencil

Lind and Stansby [135] have shown that it is possible to achieve high-order convergence rates by employing high-order kernels. These kernels are obtained by relaxing the non-negative property of the smoothing kernel. The shortcoming of this approach is the kernel must be very well sampled, restricting the range of applicability to a uniform distribution of particles. Following this approach in Nasar et al. [178], high-order Dirichlet and Von Neumann boundary conditions are proposed, while in Nasar et al. [177], a new formulation based on a kernel consistency correction has been proposed to limit the smoothing error due to the discrete SPH operator when high-order kernels are employed.

2.2.3   Weakly-Compressible vs. incompressible SPH

There are two main approaches to treating incompressible flows in SPH: the Weakly-Compressible SPH (WCSPH) and the Incompressible SPH (ISPH).

The latter approach has been proposed firstly in Cummins and Rudman [52], where a Chorin's projection method is used to enforce an incompressibility of the flow through the solution of a pressure Poisson equation that arises from the divergence-free velocity field assumption. Alternative algorithms have been also proposed in Shao and Lo [221] and Hu and Adams[97]. Notably, it has been shown in [230, 231] that the ISPH and the moving particle semi-implicit (MPS) method are equivalent. The ISPH has been applied to free-surface flows [108, 107, 228, 128], offshore application [133], and multi-phase flow [132]. The advantages of the ISPH against the WCSPH are the ability to obtain a smoother pressure field, solve the well-known problems that afflict the WCSPH, and that is able to use a larger time step. However, while the latter approach is computationally efficient due to the explicit scheme that is more easily parallelizable, especially by exploiting a parallel framework with a SIMD paradigm, such as OpenMP and CUDA, the ISPH presents bottlenecks that limit the efficiency of the method. The lack of topological connectivity between computational nodes, one of the distinctive traits of the SPH method, forces the construction of the PPE matrix at every time step. Furthermore, because of the large computational stencil, the memory requirements for storing the PPE matrix are considerably larger than the WCSPH, and also, with respect to the latter formulation that enforces the free-surface boundary condition implicitly, the ISPH must rely on free-surface detection method for correctly apply the Dirichlet boundary conditions to close the PPE.

In the WCSPH the density and the pressure are coupled through a stiff equation of state, usually Tait's Equation. To avoid an excessive restriction of the time-step due to the CFL condition, the Mach number is taken around 0.1, which bound the

variation of the density within the 1%. The advantage of this approach is the ability to use an explicit time-stepping scheme.

One of the drawbacks of the WCSPH formulation is the presence of high-frequency oscillation that affects the smoothness of the density field. This aspect has been studied by several authors [112, 68], and its stems from the combination of two different factors: on the one hand, there is the employment of a stiff equation; on the other hand, there is the collocation nature of the SPH scheme.

Various technique have been proposed during the past two decades to address this issue. Several authors [255, 192, 98] have proposed an approach based on the definition of a local Riemann problem to solve the particle interaction. The Riemann-SPH method has been used with different limiters([200, 174, 99, 210, 117], however, for violent free-surface flow, this approach has revealed to introduce too much dissipation.

In Ferrari et al. [72], has been proposed a diffusive term obtained applying a Rusanov Flux to the Riemann-SPH approach, but introducing less dissipation with respect to the latter approach. One of the drawbacks of this term is that it is neither consistent, so that doesn't vanish for $h \to 0$, nor preserve the hydrostatic solution. To restore the consistency in Molteni and Colagrossi[162] is proposed a density diffusion term based on the discretization of the laplacian of the density field with the Morris formula, which has been improved in Antuono et al. [10], the so-called "δ-SPH scheme, in order to preserve the hydrostatic solution with a consistency correction at the free-surface based on the calculation of the renormalization matrix. In Green et al. [85] is presented a diffusive term based on the application of a Roe's approximating Riemann solver, and also it is shown that the δ-SPH can be viewed as a particular case of this model. More recently, in Fourtakas et al. [75], a new diffusive model is proposed, based on the neglection of the hydrostatic pressure in the calculation of the Laplacian, which is able to preserve the hydrostatic solution without relying on the calculation of the renormalization matrix, reducing the computational cost.

2.2.4 Boundary condition in SPH

The imposition of boundary conditions to close the numerical problem is a challenging topic within the SPH method, and it has been listed as one of the SPH "Grand Challenges" by the SPHERIC committee. Among the reasons are the lack of the Delta Kronecker property and the inconsistency of the SPH interpolation in the presence of boundaries that truncate the support domain of the smoothing length.

For the definition of inlet/outlet boundary conditions, the most popular approaches are based on the extension of the computational domain by "buffer regions" in which the fluid properties are imposed to enforce Dirichlet BC or extrapolated by the fluid domain for the definition of Neumann BC. They also model the inflow and outflow by generating or deleting fluid particles that enter the computational domain. Different strategies have been proposed based on this approach, most notably [122, 247, 69, 238].

Regarding solid boundary modeling, various approaches have been proposed in the literature, each with advantages and shortcomings. In Monaghan [165], the solid BC was imposed by means of solid particles that exerted a repulsive force over the fluid particles to enforce the no-penetration condition. The repulsive force was modeled based on the Lennard-Jones potential; however, this formulation was unable to simulate a smooth surface, imposing an implicit roughness with a spatial scale equal to the particle distance that results in a disordered configuration of the fluid particles close to the interface. A further modification to address this issue was proposed in [171, 170] based on the definition of the normals to the solid interface to ensure that a particle moves in the parallel direction of the solid boundary experience a constant force. The enforcement of the no-slip condition is then implicitly accounted for by including the viscous term in the calculation of the interaction forces between the fluid and solid particles.

A different strategy, the "Dynamic Boundary Conditions" method, has been proposed in Dalrymple and Knio [53], where typically one layer of particles is placed to describe the solid boundaries. The advantage of this method is its computational efficiency and capability to discretize complex domain because these solid particles behave as fluid particles when calculating their density value. As studied in Crespo et al. [50], the solid particles exert a force that depends on the distance and the pressure of the incident fluid particles. This approach has been used to simulate the interaction between incident waves and coastal study. The shortcomings of this approach are, however, the unphysical gaps between fluid and solid particles and the generation of large oscillations in the density field. Besides, the no-penetration condition is not explicitly enforced.

In the "Ghost Particle Approach" [149], as in the DBC, several layers of particles are created at the beginning of the simulation to represent the solid interface. To generate these boundary particles, the solid interface is represented by a piecewise linear function, usually a spline, and discretized by a set of particles with a spacing equal to the characteristic particle size of the problem. After the normal and the tangent to this interface are calculated, the first layer of solid particles and the associated interpolation points in the fluid domain are created by a simultaneous contraction and expansion of the solid surface. This process is repeated recursively to ensure a sufficient number of layers based on the width of the support domain of the kernel smoothing function. The fluid properties for the solid particles are then retrieved, interpolating over the fluid domain at the interpolation points defined in the procedure outlined above. In Marrone et al. [149], the interpolation is carried out using an MLS technique, while in English et al. [66], where the mDBC is proposed to address the issue with the DBC, the correction technique of Liu and Liu [140] to restore particle consistency is employed.

One shortcoming of the Ghost Particle method is that complex geometrical features, i.e., sharp angles, must be carefully treated to define the interpolation points in the fluid domain correctly. Moreover, in the case of submerged thin elements, this approach requires placing sufficient layers on both sides of the element, which can lead to an unacceptable number of particles without a variable-resolution approach. In Adami et al. [1], the pressure is assigned based on the force balance at the solid interface.

Another popular approach is the "mirroring ghost particles", where boundary particles are generated by mirroring with respect to the solid interface, the position of fluid particles close to the contours, that either carry the field properties or obtain their values through interpolation. However, this approach is more computationally cumbersome with respect to the "Ghost Particles approach" because the mirroring procedure must be executed at each time step. Moreover, it is difficult to handle complex 3-D geometries.

The Virtual Boundary Particle [72] uses a different strategy to ensure the consistency of the SPH interpolation at the boundaries. The solid interface is discretized by a set of boundary particles whose purpose is purely geometric. An interior fluid particle close to the solid contour generated a set of fictitious particles using a local point-symmetry instead of a plane-symmetry employed in the mirrored particle approach. This procedure has been further improved in [246, 76] to ensure that the local stencil resembles that of an interior particle with full support and to have a better definition of the local stencil near corner regions.

Based on this approach, in Fourtakas et al. [75], the Local-Uniform-Stencil boundary condition has been presented: for each interior particle, at the beginning of the simulation, a uniform stencil of virtual particles is created. This local stencil moves alongside the fluid particles associated. Triangular elements then discretize the solid interface, and at each time step, using a raycasting algorithm, the particles

of the uniform local stencil are identified in the boundary region. These particles are then activated and are used to enforce the solid boundary condition. A uniform stencil ensures a zero-th and first-order consistency.

Another alternative is based on accounting for the truncated kernel at the boundary using surface integrals. These integrals calculate a corrective factor that enters the governing equations. This approach, called "Semi-analytical wall boundary condition," was first proposed in Kulasegram et al. [121] and then developed in [148, 71, 155]. However, this approach is not suited for an efficient implementation on GPUs.

2.3   Turbulence and its Modeling in SPH

2.3.1   Turbulence and its statistical modeling

The study of turbulence is one of the most complex aspects of fluid dynamics. Its statistical rather than mathematical modeling is also crucial due to the ubiquitousness of turbulent flows in any real-life flows of practical interest.

Despite that the complex nature of turbulence makes a formal definition difficult, an attempt can be made to characterize a turbulent flow by the following properties:

1. chaotic
2. has a large and continuous spectrum of spatial and time scales
3. three dimensional
4. very sensible to change in initial and boundary conditions
5. intermittent
6. mixing and dissipation are enhanced with respect to laminar flows.

It must be stressed that the words "chaotic" and "random" are not synonymous to highlight that turbulence arises from a non-linear dynamical system, the Navier-Stokes equations, which is deterministic.

One of the first studies on the nature of turbulence was given by O. Reynolds [205] by investigating a flow in a pipe while injecting a dye streak. With the systematical analysis of the results, he identified an adimensional parameter that characterized the transition from laminar to turbulent flow. This adimensional number, the Reynolds Number Re, expresses the ratio between inertial and viscous forces:

$$Re = \frac{UL}{\nu} \tag{2.2}$$

where U and L are respectively the reference velocity and length, and ν is the kinematic viscosity. Reynolds was also able to study turbulence from a statistical point of view by first introducing the Reynolds decomposition and the Reynolds Averaged Navier-Stokes (RANS) equations.

Another important contribution was given by Richardson [206], who first proposed and formalized the concept of "energy cascade", which characterizes the transfer of energy from large to smallest scales until it is dissipated due to molecular viscosity.

This concept has been later extended by Kolmogorov [115] in his theory of isotropic turbulence, which represents a cornerstone in the statistical modeling of turbulence. His theory is based on three different hypotheses[196]:

1. For a Reynolds Number Re large, the small scale of motion are statistically isotropic.

2. For a Reynolds Number Re large, the characteristic of the smallest scale of turbulence is uniquely determined by ν and ϵ, where ϵ is the turbulent dissipation rate.

3. For a Reynolds Number Re large, the characteristic of the intermediate scales of turbulence is dependent only by ϵ

From these three hypotheses, it is possible to derive important results. For example, it is possible to define the length, velocity, and time scale of the smallest structures

in a turbulent flow as:

$$\nu = \left(\frac{\nu^3}{\epsilon}\right)^{1/4}$$

$$u_\nu = (\nu\epsilon)^{1/4} \tag{2.3}$$

$$\tau_\nu = \left(\frac{\nu}{\epsilon}\right)^{1/2}.$$

Also, from the third hypothesis is possible to derive the famous Kolmogorov 5/3 law, that defines the spectrum of the turbulent kinetic energy as:

$$E(k) = C\epsilon^{2/3}k^{-5/3} \tag{2.4}$$

where k is the wave number.

The Kolmogorov theory has been verified experimentally, for example, in [213], and although some aspects, for example, the phenomenon of local intermittency, have requested a further revisitation [182, 114], it provides a justification for many assumptions that are made in the numerical modeling of turbulence.

2.3.2   Turbulence modeling in CFD

From a computational point of view, three different approaches are used in order to simulate turbulent flows: Direct Numerical Simulation (DNS), Reynolds Averaged Navier-Stokes (RANS) models, and the Large Eddy Simulation approach.

Direct Numerical Simulation is the simplest approach for simulating turbulent flows and consists in solving all the spatial and time scales of motion. It doesn't require any turbulence model, so the Navier-Stokes equations are left unchanged; however, the computational cost is very high. Assuming the Kolmogorov theory is valid, from a dimensional analysis, it can be found that the ratio between the energy-containing eddy length scale l (which is of the same order of magnitude as the domain length L) and the Kolmogorov scales (η) is proportional to $Re^{9/4}$.

If it is also considered that the time-step size is dependent on the spatial resolution Δx by the CFL condition, and also considering the total time of the simulation T, the number of computational operations N_o is proportional to:

$$N_o \approx \left(\frac{TU}{l}\right)\left(\frac{L}{l}\right)^3 Re^3. \tag{2.5}$$

However, it must be noted that if the assumption of homogeneous turbulence is discarded, a different estimation can be found, for example, in Choi and Moin[38] where the grid requirement for solving a turbulent boundary layer is calculated as proportional to $Re^{33/12}$. The preferred numerical approaches for DNS are finite-difference methods or pseudo-spectral methods [209], due to their high-order accuracy and computational efficiency. However, their extension to complex geometries is rather difficult. For these reasons, at the moment, the DNS approach can't be extended to flows with industrial applications in the foreseeable future. However, from a scientific perspective, DNS has been an invaluable tool for gaining insight into turbulence, shifting its study from a statistical to a structural point of view [100]. In fact, despite some recent progress in experimental techniques, such as Particle Image Velocimetry, the numerical solution can provide an unmatched amount of data while also having strict control over initial and boundary conditions.

The RANS approach assumes that the turbulent field can be decomposed into two different contributions, the mean velocity field and the turbulent fluctuations. With this decomposition, a new term that represents the contributions of the turbulent fluctuations over the mean velocity field, the Reynolds stresses, appears in the governing equations. In order to solve the RANS equations, a proper modeling of the Reynolds stresses must be introduced in order to close the numerical problem.

The most popular turbulence models for the RANS technique are based on the turbulent viscosity approach. As noted in Pope [196], this hypothesis can be split into two assumptions: on the first hand, the Reynolds-stress is a function of the

mean velocity gradients, on the other hand, this relation is analogous to the relation between the deformation strain tensor and the viscous stresses. The RANS approach is very convenient from a computational point of view because both the laminar and the turbulent viscous terms can be treated in the same way.

Early RANS models were based on the simple mixing length approach, where the turbulent viscosity is a function of a reference length and the strain tensor. For the calculation of attached boundary layers, this approach gave satisfactory results, although this model is considered incomplete because the reference length must be specified explicitly and is dependent on the particular computational problem to be solved. A more complex approach, but still dependent on the definition over the mixing length, is the one-equation model based on the solution of an additional transport equation for the turbulent kinetic energy k.

The completeness issue has been resolved with two-equation models, such as the $k - \epsilon$[103, 123] and the $k - \omega$ [266] turbulent models, that don't rely on the specification of flow-dependent variable such as the mixing length. In fact, in these models, additional transport equations are defined for two turbulence quantities: for the $k - \epsilon$ model, the from the turbulence kinetic k and the dissipation rate ϵ a length-scale can be formed. In the $k - \omega$, instead, the transported quantity is $\omega = k/\epsilon$. For both models, the transport equations for the second quantity depend on constants whose value is found empirically and adjusted depending on the particular application. With respect to the $k - \epsilon$, the $k - \omega$ is better for describing the region near boundary walls, while the $k - \epsilon$ is superior in the prediction of non-turbulent free-stream boundaries. To limit the shortcomings of both models, Menter [157] has proposed a hybrid model that blends the $k - \omega$, employed close to the wall, with the $k - \epsilon$ model, that is used in the outer region.

Although algebraic models are very popular and computationally cheap and are included in almost every CFD commercial code, they predict accurate results

only for a narrow range of flows; for example, two-dimensional shear flows where streamlines curvature effects are small. For flows characterized by strong swirl, an alternative is represented by Reynolds-stress models, in which the turbulent viscosity hypothesis is disregarded, and transport equations are solved for each component of the Reynold-stress tensor. However, these models require a more complex numerical treatment and an additional computational cost. On top of that, it is known that the RANS models poorly performs in case of three-dimensional turbulence and in high unsteady flows such as flows past bluff bodies [232]. In this case, a time-resolving RANS formulation (URANS) can improve the results, although it relies on the implicit argument that there is a large separation of length and time scales, which is almost always a fallacious assumption.

The Large Eddy Simulation approach is an intermediate numerical modeling between DNS and RANS. In fact, the basic idea of LES is to resolve the mean flow and the large energy-containing eddies while modeling, with an appropriate closure, the small-scale structures. This is achieved by filtering the Navier-Stokes equation: the filter can be explicit, e.g., a Gaussian filter, or applied implicitly by the minimum grid resolution equivalent to a box filtering. This approach is motivated by the results of the statistical theory of turbulence: the energy cascade model indicates that the information flows from large to small eddies so that the large eddies will not be influenced by non-resolving small-scale structures. Moreover, the Kolmogorov theory suggest that the smallest eddies have a universal character, so the assumption is that they are all modeled from a single closure model.

The oldest and simplest LES closure is the Smagorinsky model, which consist of a linear eddy-viscosity model that related the residual stress to the rate of strain of the resolved scale. The eddy-viscosity is a function of a constant, the *Smagorisnky Coefficient* C_S, the filter width and the filtered rate of strain. The shortcomings of this model are the poor prediction in the limit case of laminar flows and in the

near-wall region, which led some authors [161] to use a damping function to clip the value of the residual viscosity. Moreover, there isn't a specific value *Smagorisnky Coefficient* C_S that has a general application. To address this issue, the dynamic model [79, 131] has been proposed on the idea of using a double filtering procedure to obtain the optimal local value of C_S.

A complete review of the mathematical and numerical aspects of the LES approach can be found in Sagaut [214], where other closure models are presented.

From a computational point of view, the LES modeling is generally considerably cheaper than DNS, except for boundary layers, which need an adequate resolution in order to resolve the viscous sublayer correctly. In this case, an estimation of the grid points requirement for a wall-resolving LES is given in Choi and Moin[38] as $Re^{13/7}$, while if instead the near-wall region is modeled, the requirement scales linearly with the Re.

2.3.3 Turbulence modeling in SPH

One of the earliest contributions to the development of a turbulence model specifically designed for the SPH method is presented in Monaghan (2002)[166], where an adaptation of the Lagrangian-Averaged Navier-Stokes (LANS) α-model by Holm (1999) [95] has been proposed for SPH. Therein, the velocity is smoothed based on an average across the neighboring particles, while preserving the flow invariants. In Monaghan (2011)[168], this formulation is then presented as the ϵ-model and later on validated for the cases of a cylindrical stirrer [251], and the decay of turbulence in a square box [169], where two-dimensional turbulence is driven by a moving cylinder.

One of the first attempts of including Reynolds-Averaged Navier-Stokes (RANS) modeling into SPH can be found in Violeau et al. (2002) [258], where a mixing model and a stochastic approach named the Generalize Langevin Model (GLM) have been implemented to study turbulent Poiseuille flow, showing a good correlation of the

numerical results with the log-wall of the turbulent boundary layer. In Violeau and Issa (2007) [257], approaches such as the k-ϵ and the Explicit Algebraic Reynolds Stress Models (EARSM) have been investigated to address the simulation of dam-breaking flows. Therein, the authors report a good qualitative agreement against experimental results, especially for the EARSM model, which is more suited to study regions with high distortion near the free surface. Future contributions led to a k-ϵ model combined with the semi-analytical wall boundary conditions for Weakly Compressible SPH (WCSPH) in Ferrand et al. (2013) [71] and Incompressible SPH (ISPH) in Leroy et al. (2014) [128], showing good agreement with the Finite-Volume Method (FVM) for a fish-pass flow. The k-ϵ model has also been used with the ISPH to investigate wave overtopping [219] and breaking [220] and more recently solitary[260] and periodic waves[261].

In later years, a switch to Large Eddy Simulation (LES) has been observed, trying to exploit the analogy between the LES filtering procedure and the SPH interpolation. One of the pioneering contributions to LES applied to SPH can be found in Lo and Shao (2002) [142], where turbulent solitary beach waves have been studied with a focus on turbulence during the breaking phase. This model has then been extended to WCSPH by Dalrymple and Rogers (2006)[54], providing validation against numerical experiments for cases of wave overtopping and beach waves in 2-D and dam breaking flow in 3-D.

In Mayrhofer (2015) [156], a LES approach in SPH has been coupled with the semi-analytical wall boundary conditions for studying turbulent channel flow, however, results therein have shown an overprediction of the streamwise velocity. The authors pointed out that this is probably due to insufficient resolution when capturing the vortex. More recently, the LES approach has been employed in the simulation of turbulent open channel flows over and within natural porous gravel beds [105] and in the modeling of oil spill[225] using the ISPH formulation.

In Di Mascio et al. (2017) [57] and Antuono et al. (2021) [9], a new approach to LES modeling in SPH is presented. The key idea of these contributions is to use a time-space filtering procedure, where the SPH kernel operator acts as a spatial filter while time filtering is implicitly accounted for with additional terms in the governing equations. This strategy offers a consistent approach to LES while interpreting the δ-SPH by Molteni and Colagrossi (2009) [162] from a LES perspective, i.e., the delta coefficient as the deviatoric strain of the mean flow. The δ-LES model has also been employed for studying gravity waves [158] and dam-break flow [158].

From a Direct Numerical Simulation (DNS) perspective, Robinson and Monaghan (2012) [208] have attempted the DNS of two-dimensional decaying turbulence, although 2-D turbulence is fundamentally different from 3-D because of the inverse energy cascade phenomena [22, 119]. Notable contributions have been made in Mayrhofer et al. (2015) [156], where a wall-bounded flow is simulated, and a lower bound in terms of the number of particles per vortex is suggested.

From the presented literature review, it is evident that several crucial aspects remain to be addressed concerning turbulence modeling in SPH. The initial consideration involves determining the most suitable approach for turbulence modeling. While the RANS modeling appears to be a more favorable choice, given the high computational cost associated with the SPH method, it seems to lack the necessary theoretical foundations for its application in the typical SPH domain, which includes free-surface flows with considerable non-stationarity and distortions.

LES modeling appears to be the most suitable approach, but there are still problematic aspects related to the SPH method that require further investigation. The first issue concerns the method's order of accuracy: LES modeling demands a high degree of accuracy to ensure that the numerical dissipation introduced by the numerical scheme does not compromise the fidelity of the results. However, this conflicts with the current convergence order of the SPH method, which is

at most second-order in optimal situations, while under normal conditions, due to the truncation error caused by the irregular distribution of particles, it ranges between 1 and 2. Although approaches for achieving a convergence order higher than second-order have been proposed, as previously discussed, they do not yet seem to be mature enough for broader application.

The second aspect pertains to the computational cost of the method. As previously discussed, a turbulent flow is characterized by a wide spectrum of spatial and temporal scales. In grid-based methods, this aspect is addressed by increasing the resolution in areas where vortex development is expected, particularly near solid surfaces. The introduction of variable resolution in SPH encounters challenges arising from the method's particle-based Lagrangian formulation. In the following section, these aspects will be discussed, and an overview of the state-of-the-art for multi-resolution in the SPH method will be provided.

2.4 Adaptivity within the SPH Method

One weakness of the SPH approach is that adopting a multi-resolution formulation is more challenging than in mesh-based method. There are several reasons:

- As previously illustrated, in order to preserve the convergence property, the ratio between the smoothing length and the mean particle size must be kept at least constant. This means that in order to increase the numerical accuracy, the value of the kernel smoothing length cannot be reduced without increasing the total number of particles in the simulation.

- The interaction between particles with different smoothing lengths must be treated carefully. Different approaches have been proposed in the literature, and some of them are derived trying to preserve the variational consistency [24, 26]. Nevertheless, the smoothed formulation of the method prevents a sharp variation of the particle size.

- The symmetricity of the smoothing kernel function, a cornerstone of the SPH formulation, implies the isotropic distribution of the computational nodes, as opposed to grid-based methods that can exploit the anisotropy of the flow by using different spacing depending on the spatial coordinate. A typical example is the inflation layers used to discretize the near-wall region, where the spatial resolution in the wall-normal direction is usually one order of magnitude lower than in the streamwise or spanwise direction.

Historically, early attempts for the introduction of adaptivity in the SPH method were focused on the introduction of a variable smoothing length formulation coupled with the definition of regions with different particle sizes at the beginning of the simulations, for example in Bonet and Paz [24] for the collapse of a circular dam over a surface, cylindrical water blast [26], wedge water entries [184], heaving cylinder and cone in traveling waves [188][189]. However, these approaches were limited to problems with a short time scale and were unfeasible for cases in which the motion of the computational nodes highly distorted the initial configuration of particles.

Instead, later efforts aimed to dynamically increase the particle resolution by introducing a dynamic refinement process under the constraints of conserving mass, momentum, and angular velocity and minimizing the error in the estimation of the density with different splitting patterns [70, 204]. The basic concept is to minimize, in a least squares sense, the error in the SPH estimation of the density field between the original particle distribution and the refined one. A parametric study on the optimal splitting pattern, along with the optimal value of the weight of each particle size λ_i, their smoothing length value h_i, and the distance with respect to the original particle ϵ_i, has been presented in Vacondio et al. [248]. The dynamic splitting procedure has been coupled in Vacondio et al. [249] to a de-refinement process based on coalescing pairs of particles with similar sizes and extended to 3-D in Vacondio et al. [250]. A similar approach is used in Yang et al. [272] for the computation of multi-phase [273] and free-surface [274] flows, where the splitting criterion is not based on the geometric definition of a fixed refinement region, but instead on the position with respect to the free-surface or interface between different phase.

However, one weakness of this approach is the loss of computational efficiency with the increase of the refinement ratio. In fact, as discussed in Vacondio et al. [248], in order to minimize the error introduced by the splitting procedure, the value of

the smoothing length between the coarse and the fine particles remains almost equal, while the particle size decreases due to the splitting procedure (typically hexagonal or square). This means that the computational stencil increase along with the resolution, introducing an important source of inefficiency of the method, which is even more serious in three-dimensional applications. Moreover, the coalescing procedure is only performed pairwise, so less frequent with respect to the splitting procedure, which causes an unnecessary overhead in terms of the number of particles. In [175] [89], this issue is tackled by taking as kernel smoothing length, instead of the optimal value prescribed by the least square minimization, the average value in the support domain of the kernel, and results are presented for the computation of flow past bluff bodies.

A different approach is proposed in Barcarolo et al. [15]: as in the splitting-coalescing procedure, a particle is split into fine particles when entering the refinement region. However, in this approach, the original particle, instead of being deleted, is retained and it is ipotetically advected. A weight function governs the transition between the two zones to avoid pressure discontinuities at the interface. The same approach has been improved in Chiron et al. [37] by resolving the interaction between coarse and refined particles with the definition of buffer zones that avoid the interaction between particles of different sizes. Using this approach, in Sun et al. [235], results are presented for flows past bodies with various shapes, coupling the multiresolution algorithm with a Tensile Instability Control (TIC) term, while in Sun et al. [236] the method is employed to study water entry of circular cylinders. In Gao et al. [78], a block-based adaptive particle refinement algorithm is proposed for dynamically changing the particle refinement domain coupled with a regularization process similar Particle Shifting Technique (PTS) [136] to obtain an isotropic distribution of the refined particle in the transition zone.

However, one of the weaknesses of the Adaptive Particle Refinement approach is the decoupling of the position between coarse and fine (daughter) particles, which

in highly distorted flows, as detailed in Chaneac et al. [35], results in an over-creation of particles which eventually leads to unstable solutions.

In the domain-decomposition method, the computational domain is subdivided into many computational sub-problem, and are advanced in time with an appropriate coupling strategy. An approach based on this formulation has been proposed in Bian et al. [20]. However, the results presented only two levels of refinement, and the density formulation wasn't able to treat free-surface flows. In Shibata et al. [224] a similar strategy based on inlet/outlet boundary conditions is introduced for the coupling of different resolution zones in the context of the MPS method. Multi-resolution approaches, mainly devoted to Fluid-structure problems in which different resolutions are defined between the fluid and the solid phase, have been proposed in Zhang et al. [281] and Khayyer et al. [110]. However, these approaces are limited only to fluid-structure problem and allow a very small variation in the particle size between the different phases.

CHAPTER 3

NUMERICAL FRAMEWORK

This chapter presents the basis of the mathematical treatment in the SPH method alongside the computational techniques that represent the state-of-the-art of the SPH methodology and that have been used in this work.

3.1 Basis of the SPH Methodology

3.1.1 SPH continuous interpolation

The mathematical treatment of the SPH interpolation method starts from the convolution of a field function and the Dirac's Delta function $\delta(\mathbf{x} - \mathbf{x}')$:

$$f(\mathbf{x}) = \int_\Omega f(\mathbf{x}')\delta(\mathbf{x} - \mathbf{x}')d\mathbf{x}'. \tag{3.1}$$

An approximation of the previous identity is obtained by substituting the δ function with a smoothing kernel function $W(\mathbf{x} - \mathbf{x}', h)$:

$$\langle f(\mathbf{x})\rangle = \int_\Omega f(\mathbf{x}')W(\mathbf{x} - \mathbf{x}', h)d\mathbf{x}', \tag{3.2}$$

where h is the *smoothing length*, a parameter that defines the size of the kernel support Ω.

The properties of the kernel smoothing function W influence the convergence, accuracy, and stability of the SPH interpolation and will be discussed in the next section.

Expressing the derivative of (3.2) with respect to $\mathbf{x}'$ and using integration by parts, it can be derived the expression for the SPH gradient operator:

$$\nabla\langle f(\mathbf{x})\rangle = \int_\Omega \nabla f(\mathbf{x}')W(\mathbf{x} - \mathbf{x}', h)d\mathbf{x}' - \int_\Omega f(\mathbf{x}')\nabla W(\mathbf{x} - \mathbf{x}', h)d\mathbf{x}' =$$
$$= \int_{\partial\Omega} f(\mathbf{x}')W(\mathbf{x} - \mathbf{x}', h) \cdot \bar{\mathbf{n}}dS - \int_\Omega f(\mathbf{x}')\nabla W(\mathbf{x} - \mathbf{x}', h)d\mathbf{x}'. \tag{3.3}$$

The first integral is obtained by applying the Gauss theorem to pass from a volume to a surface integral and, assuming that the kernel function has compact support and this is not truncated, this term is equal to zero, and the following identity is obtained:

$$\nabla \langle f(\mathbf{x}) \rangle = - \int_{\Omega} f(\mathbf{x}') \nabla W(\mathbf{x} - \mathbf{x}', h) d\mathbf{x}'. \tag{3.4}$$

Moreover, if the smoothing kernel $W(\mathbf{x} - \mathbf{x}', h)$ is an even function, the last expression can be rewritten as:

$$\langle \nabla f(\mathbf{x}) \rangle = \int_{\Omega} f(\mathbf{x}') \nabla W(\mathbf{x}' - \mathbf{x}, h) d\mathbf{x}'. \tag{3.5}$$

where the differential operator ∇ is referred to $\mathbf{x}$.

From here on, the bracket notation to identify the SPH approximation will be omitted.

3.2 Properties of the Smoothing Kernel Function

There is a set of properties there are desirable for the kernel smoothing function:

1. Unity:
$$\int_{\Omega} W(\mathbf{x} - \mathbf{x}', h) d\mathbf{x}' = 1. \tag{3.6}$$

2. Even function:
$$W(\mathbf{x} - \mathbf{x}', h) = W(\mathbf{x}' - \mathbf{x}, h). \tag{3.7}$$

3. Compactely supported:
$$W(\mathbf{x} - \mathbf{x}', h) = 0 \text{ if } |\mathbf{x} - \mathbf{x}'| > ah. \tag{3.8}$$

4. Positivity:
$$W(\mathbf{x} - \mathbf{x}', h) \geq 0, \forall\, \mathbf{x}'. \tag{3.9}$$

5. Delta function:

$$\lim_{h \to 0} W(\mathbf{x} - \mathbf{x}', h) = \delta(\mathbf{x} - \mathbf{x}'). \tag{3.10}$$

6. Monotonically decreasing

7. Smoothness

The first condition ensures that the SPH interpolation has a C^0 consistency when the support domain of the kernel function is far from the boundaries and is able to reproduce a constant function exactly .

Together with the requirement that the smoothing kernel is an even function, it can be demonstrated that the SPH interpolation in Equation (3.2) is converging with a 2nd order convergence rate. In fact, expanding a field function $f(\mathbf{x}')$ in Taylor series:

$$f(\mathbf{x}') = f((\mathbf{x}) + f'(\mathbf{x})(\mathbf{x}' - \mathbf{x}) + \frac{1}{2}f''(\mathbf{x})(\mathbf{x}' - \mathbf{x})^2 + \mathcal{O}(\mathbf{x}' - \mathbf{x})^3, \tag{3.11}$$

and multiplying the previous equation by Equation (3.2), it is obtained:

$$f(\mathbf{x}) = f(\mathbf{x}) \int_{\Omega} W(\mathbf{x} - \mathbf{x}', h)d\mathbf{x}' - f'(\mathbf{x}) \int_{\Omega} (\mathbf{x} - \mathbf{x}')W(\mathbf{x} - \mathbf{x}', h)d\mathbf{x}'$$
$$+ \frac{1}{2}f''(\mathbf{x}) \int_{\Omega} (\mathbf{x}' - \mathbf{x})^2 W(\mathbf{x} - \mathbf{x}', h)d\mathbf{x}' + \int_{\Omega} \mathcal{O}(\mathbf{x}' - \mathbf{x})^3 d\mathbf{x}'. \tag{3.12}$$

From the previous identity it can be seen that in order to ensure that the approximation has a 2nd order of accuracy, the first two moment M_k must be equal to 0:

$$M_0 = \int_{\Omega} W(\mathbf{x} - \mathbf{x}', h)d\mathbf{x}' = 1, \tag{3.13}$$

$$M_1 = \int_{\Omega} (\mathbf{x} - \mathbf{x}')W(\mathbf{x} - \mathbf{x}', h)d\mathbf{x}' = 0. \tag{3.14}$$

It can be observed that these two conditions are fulfilled if the smoothing kernel $W(\mathbf{x} - \mathbf{x}', h)$ verifies the Unity and the Even properties in Equations (3.6) and (3.7).

Moreover, it can also be demonstrated that all odd moment M_k are identically equal to 0.

Regarding the other properties: the smoothing function is chosen to have compact support to reduce the numerical stencil and the computational cost; the positivity condition, rather than a mathematical requirement, is based on the physical admissibility of hydrodynamical states, i.e., density and energy. This condition also prevents the vanishing of the even-order moments of the smoothing function so that the SPH approximation has, at most, a 2nd-order accuracy. The Delta function in Equation (3.10) properties ensure that the smoothing function recovers the Dirac distribution as the smoothing length h tends to zero. The sixth property is based on the assumption that closer value must have a bigger influence over the SPH estimation, while the last property improves the accuracy of the interpolation [199].

Another interesting property that derives from the symmetric condition, is that the kernel function can be expressed as a function of the distance between spatial points:

$$W(\mathbf{x} - \mathbf{x}', h) = W(|\mathbf{x} - \mathbf{x}'|, h). \tag{3.15}$$

Furthermore, the kernel function can be written in dimensionless form as:

$$W(|\mathbf{x} - \mathbf{x}'|, h) = W(q), \tag{3.16}$$

where q is obtained operating the following change of variable:

$$q = \frac{|\mathbf{x} - \mathbf{x}'|}{h}. \tag{3.17}$$

Therefore, a general expression of kernel function is:

$$W(q) = \frac{\alpha_d}{h^d} f(q), \tag{3.18}$$

where d is the space dimension, and α_d is a scaling factor, which is obtained from the Unity condition.

Moreover, the derivative of the kernel function can be written as:

$$W(|\mathbf{x} - \mathbf{x}'|, h) = \frac{\alpha_d}{h^d}\nabla f(q) = \frac{\alpha_d}{h^{d+1}}f'(q)\frac{\mathbf{x} - \mathbf{x}'}{|\mathbf{x} - \mathbf{x}'|}. \tag{3.19}$$

The most popular choices for smoothing kernel functions are the Gaussian, B-Splines, and Wedland kernels. In this work, apart from when explicitly stated, a quintic Wedland kernel function is used:

$$W(q) = \frac{\alpha_d}{h^d}(2q + 1)\left(1 - \frac{q}{2}\right)^4; \quad 0 \leq q \leq 2. \tag{3.20}$$

The normalization coefficient α_d is equal to $\frac{7}{4\pi}$ in two dimension and $\frac{21}{16\pi}$ in a three-dimensional space.

Following Lind and Stansby [135], a high-order kernel can be obtained with the vanishing of the even-order moments. A general form of the kernel that satisfies this condition is:

$$W_n = \sum_{m}^{n-1} A_{2m}q^{2m}W, \tag{3.21}$$

where n is the order of accuracy and W is the base kernel, and the coefficients A_{2m} are obtained by imposing the normalization condition and the vanishing of the M_n moments.

Therefore, 4th and the 6th order kernel schemes are obtained starting from the W_{2C6} kernel [265]:

$$W_{2C6} = (1 - \frac{q}{2})^8(4q^3 + 6.25q^2 + 4q + 1). \tag{3.22}$$

The 4th order scheme has the form:

$$W_{4C6} = (A + Bq^2)W_{2C6}, \tag{3.23}$$

39

and for the 6th order:

$$W_{6C6} = (A + Bq^2 + Cq^4)W_{2C6}. \tag{3.24}$$

In Figure 3.1, the quintic Wedland kernel, the W_{4C6} and W_{6C6} are shown along with their derivative. It can be noted that the high-order kernels have a negative regions that can lead to instabilities due to inadmissible values in the density estimation. For this reason, in this work, the high-order kernels will be used only coupled with an Eulerian formulation that ensures a well-sampled support domain.
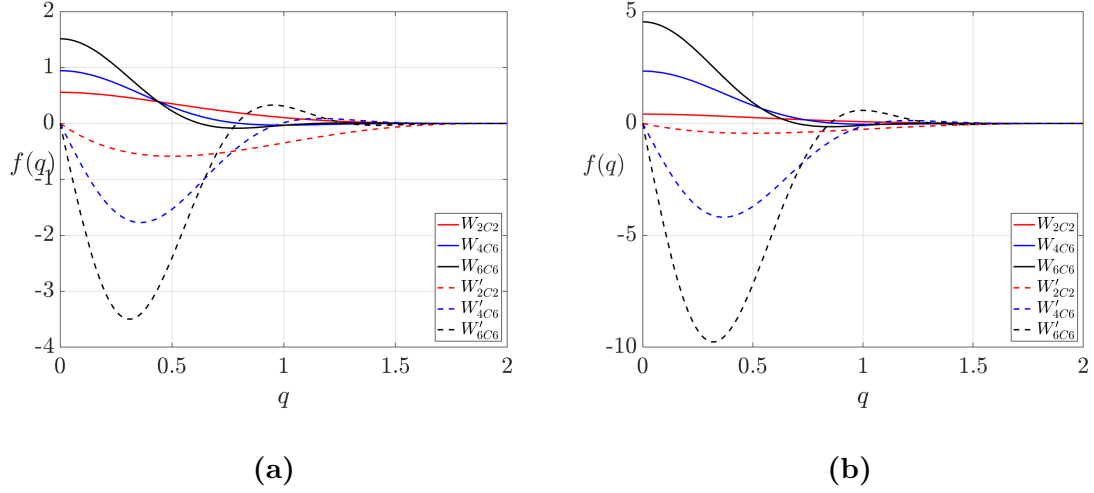
Figure 3.1 Graphs of the kernels and their derivatives used in this work in 2-D and 3-D (b).

3.3 Discrete approximation

The final expression of the SPH interpolation is obtained by approximating the integral operator in Equation (3.2), through a Riemann sum over a discrete set of particles:

$$f(\mathbf{x}) = \int_\Omega f(\mathbf{x}')W(\mathbf{x} - \mathbf{x}', h)d\mathbf{x}' \approx \sum_{b=1}^{N_b} V_b f(\mathbf{x}_b)W_{ab}, \tag{3.25}$$

where $W_{ab} = W(\mathbf{x_a} - \mathbf{x_b}, h)$ and N_b is the number of neighboring particles included in the support domain of the kernel smoothing function.

These particles have a dual role, acting as both interpolation points and carrier of physical quantities such as velocity, pressure, and mass. In fact, the particle volume can be expressed as:

$$V_a = \frac{m_a}{\rho_a}, \tag{3.26}$$

and consequently can also be defined the particle size:

$$dr = V^{1/d}. \tag{3.27}$$

Because, as seen later, the density variation is small under a weakly-compressible formulation, this size remains approximately constant.

This also allows the definition of another important quantity, the ratio between the smoothing length h and the initial interparticle distance h/dr. Usually, depending on the particular application, a value between $1 - 2$ is chosen.

Knowing the h/dr value, the number of neighbors N_b in Equation (3.25), can also be derived:

$$N_b \approx \frac{2\pi^{n/2}}{n\Gamma\left(\frac{n}{2}\right)} \left(\frac{qh}{dr}\right)^d, \tag{3.28}$$

which gives for the Wedland kernel with $h/dr = 2.0$ a number of particles approximately equal to 50 in 2-D and 200 in 3-D.

Applying Equation (3.25) to Equation (3.5), the SPH gradient and divergence operators can be defined as follows:

$$\nabla f(\mathbf{x}_a) = \sum_b V_b A_b \nabla W_{ab}, \tag{3.29}$$

$$\nabla \cdot f(\mathbf{x}_a) = \sum_b V_b A_b \cdot \nabla W_{ab}. \tag{3.30}$$

However, the former expressions don't ensure the conservation of momentum and angular momentum when applied to the governing equations of fluid dynamics. For this reason, a different formulation is preferred.

Starting from the following identities:

$$\nabla f(\mathbf{x}) = \rho^k \nabla \frac{f(\mathbf{x})}{\rho^k} + \frac{f(\mathbf{x})}{\rho^k} \nabla \rho^k \tag{3.31}$$

$$\nabla \cdot f(\mathbf{x}) = \rho^k \nabla \cdot \frac{f(\mathbf{x})}{\rho^k} + \frac{f(\mathbf{x})}{\rho^k} \cdot \nabla \rho^k, \tag{3.32}$$

$$\nabla f(\mathbf{x}) = \frac{1}{\rho^k} \nabla (f(\mathbf{x})\rho^k) - \frac{f(\mathbf{x})}{\rho^k} \nabla \rho \tag{3.33}$$

$$\nabla \cdot f(\mathbf{x}) = \frac{1}{\rho^k} \nabla \cdot (f(\mathbf{x})\rho^k) - \frac{f(\mathbf{x})}{\rho^k} \cdot \nabla \rho^k, \tag{3.34}$$

the symmetric operator SPH derivative operator can be defined as:

$$\nabla f(\mathbf{x}_a) = \sum_b V_b \frac{\rho_b^{2k} f(\mathbf{x}_a) + \rho_a^{2k} f(\mathbf{x}_b)}{(\rho_a \rho_b)^k} \nabla W_{ab}, \tag{3.35}$$

$$\nabla \cdot f(\mathbf{x}_a) = \sum_b V_b \frac{\rho_b^{2k} f(\mathbf{x}_a) + \rho_a^{2k} f(\mathbf{x}_b)}{(\rho_a \rho_b)^k} \cdot \nabla W_{ab}. \tag{3.36}$$

In the same way, the antisymmetric operator is defined as:

$$\nabla f(\mathbf{x}_a) = -\sum_b V_b (\rho_a \rho_b)^k (f(\mathbf{x}_a) - f(\mathbf{x}_b)) \nabla W_{ab}, \tag{3.37}$$

$$\nabla \cdot f(\mathbf{x}_a) = -\sum_b V_b (\rho_a \rho_b)^k (f(\mathbf{x}_a) - f(\mathbf{x}_b)) \cdot \nabla W_{ab}, \tag{3.38}$$

where k is a constant that is usually taken equal to 0 or to 1.

For $k = 0$ are obtained the following operators:

$$\nabla f(\mathbf{x}_a) = \sum_b V_b (f(\mathbf{x}_a) + f(\mathbf{x}_b)) \nabla W_{ab} \tag{3.39}$$

$$\nabla \cdot f(\mathbf{x}_a) = \sum_b V_b (f(\mathbf{x}_a) + f(\mathbf{x}_b)) \cdot \nabla W_{ab}, \tag{3.40}$$

$$\nabla f(\mathbf{x}_a) = -\sum_b V_b (f(\mathbf{x}_a) - f(\mathbf{x}_b)) \nabla W_{ab} \tag{3.41}$$

$$\nabla \cdot f(\mathbf{x}_a) = -\sum_b V_b (f(\mathbf{x}_a) - f(\mathbf{x}_b)) \cdot \nabla W_{ab}. \tag{3.42}$$

It must be noted that the symmetric operators defined in Equations (3.35)-(3.36) don't provide a zero value when applied to a constant function. Instead, the antisymmetric operator in Equations (3.37)-(3.38) possesses the zero order consistency.

3.4 Weakly-Compressible Navier Stokes Equations and SPH Discretization

3.4.1 Governing equations

The weakly Navier-Stokes equations in Lagrangian form are written as:

$$
\begin{aligned}
\frac{d\rho}{dt} &= -\rho \nabla \cdot \mathbf{v}, \\
\frac{d\mathbf{v}}{dt} &= -\frac{\nabla P}{\rho} + \mathbf{g} + \Gamma, \\
\frac{d\mathbf{x}}{dt} &= \mathbf{v},
\end{aligned}
\tag{3.43}
$$

where ρ is the density, $\mathbf{x}$ is the position vector, $\mathbf{v}$ is the velocity vector, $\mathbf{g}$ is the gravity vector, P is pressure and Γ represents the viscous term that depends on the particular formulation employed.

The same set of equations in Eulerian form are instead:

$$
\begin{aligned}
\frac{\partial \rho}{\partial t} &= -\rho \nabla \cdot \mathbf{v} - \mathbf{v} \cdot \nabla \rho, \\
\frac{\partial \mathbf{v}}{\partial t} &= -\nabla \cdot (\mathbf{v} \otimes \mathbf{v}) - \frac{\nabla P}{\rho} + \mathbf{g} + \Gamma,
\end{aligned}
\tag{3.44}
$$

where the need of an advection equation is not present since particles are not moving in time.

For the computation of the pressure field, in this work the Weakly-Compressible SPH (WCSPH) approach is adopted, in which the pressure and the density are related by a stiff equation of the form:

$$
P(\rho) = B \left[\left(\frac{\rho}{\rho_0} \right)^{\gamma} - 1 \right],
\tag{3.45}
$$

where ρ_0 is the reference density, $B = c_0^2 \rho_0 / \gamma$ with c_0^2 is the nominal speed of sound, and γ is the polytropic constant. In this work, following [81], the reference values adopted are $\rho_0 = 1000$ and $\gamma = 7$. The speed of sound is not chosen following the physical properties of the water, which would result in very small time steps. Therefore, to enforce a weakly compressible regime by keeping the density variations around 1% of the reference value, the speed of sound $c_0 = 10\mathbf{v}_{max}$, where $\mathbf{v}_{max}$ is the maximum flow velocity.

3.4.2 SPH discretization

Applying operators in Equations (3.39)-(3.42) to the set of Equations ((3.43)), we obtain the WCSPH governing equations in Lagrangian form:

$$\frac{d\rho_a}{dt} = \sum_b m_b \mathbf{v}_{ab} \cdot \nabla_a W_{ab} + \mathcal{D}_a, \tag{3.46}$$

$$\frac{d\mathbf{v}_a}{dt} = \sum_b m_b \left(\frac{P_b + P_a}{\rho_a \rho_b} \right) \nabla_a W_{ab} + \Gamma_a, \tag{3.47}$$

$$\frac{d\mathbf{x_a}}{dt} = \mathbf{v_a}. \tag{3.48}$$

Similarly, for the Eulerian formulation in Equations ((3.44)) one obtains:

$$\frac{\partial \rho_a}{\partial t} = \sum_b m_b (\rho_a \mathbf{v}_a - \rho_b \mathbf{v}_b) \cdot \nabla_a W_{ab} + \mathcal{D}_a, \tag{3.49}$$

$$\frac{\partial \mathbf{v}_a}{\partial t} = \sum_b m_b \left(\frac{P_b + P_a}{\rho_a \rho_b} \right) \nabla_a W_{ab} - \sum_b (\mathbf{v}_a \otimes \mathbf{v}_a + \mathbf{v}_b \otimes \mathbf{v}_b) \cdot \nabla_a W_{ab} V_b + \Gamma_a. \tag{3.50}$$

In the previous sets of equations, $\mathcal{D}_a$ and Γ_a are the diffusive terms, respectively, in the continuity and the momentum equation, that are added to stabilize the system or model the effect of dissipative terms, such as viscous stresses.

Furthermore, it must be noted that for discretizing the momentum equation, the symmetric SPH gradient operator has been preferred. Despite, as previously mentioned, this term is not able to reproduce exactly the derivative of a constant function in case of a non-uniform particle distribution, it is preferred.Infact, as

discussed in [198], this discretization ensure a more isotropic particle arrangement and avoid the clumping of particles. Besides, as shown in [259], the set of discrete operators chosen is consistent with a variational formulation, ensuring the proper conservation of the linear and angular momentum.

Nevertheless, some authors have proposed alternative formulation [235, 185], based on using both the antisymmetric and symmetric SPH operator in the discretization of the momentum equation, depending on the sign of the pressure. However, these approaches don't explicitly preserve momentum conservation.

3.5   Viscosity Models

3.5.1   Artificial viscosity

The artificial viscosity model has been introduced in the SPH method for ensure the stability of the numerical solution in the presence of strong shocks [164]. In this model, a dissipative term Φ_a, similar to the Von Neumann-Richtmyer viscosity, is added into the momentum equation:

$$\Gamma_a = \begin{cases} -\alpha \frac{h\bar{c}_{ab}\mu_{ab}}{\bar{\rho}_{ab}} \nabla_a W_{ab}, & \text{if } \mathbf{v}_{ab} \cdot \mathbf{r}_{ab} \leq 0 \\ 0, & \text{otherwise} \end{cases} \tag{3.51}$$

with μ_{ab}:

$$\mu_{ab} = \frac{\mathbf{v}_{ab} \cdot \mathbf{r}_{ab}}{\mathbf{r}_{ab}} \tag{3.52}$$

The parameter α is a tunable coefficient usually taken in the range between $0.1 - 0.01$, and $\bar{c}_{ab}$ and $\bar{\rho}_{ab}$ define the average values of the speed of sound and the density. The advantages of this model is that it preserve the conservation of the angular momentum. As demonstrated in [67], the value of α can be related to the physical kinematic viscosity nu as:

$$\nu = \frac{\alpha h c_0}{2(D+2)} \tag{3.53}$$

where D is the dimensionality of the problem.

3.5.2 Laminar viscosity

The laminar viscosity model start from the SPH discretization of the viscous term for an incompressible flow

$$\Gamma = \mu \nabla^2 \mathbf{v}. \tag{3.54}$$

Instead of discretizing using an SPH spatial operator which would be very sensitive to the particle disorder [256], an SPH and a finite-difference first derivative operator are mixed [173]in order to obtain the following discretization of the viscous stress tensor [142]:

$$(\mu \nabla^2 \mathbf{v})_a = 4m_b \frac{\nu \mathbf{r}_{ab} \cdot \nabla_a W_{ab}}{(\rho_a + \rho_b)r_{ab}^2} \mathbf{v}_{ab}. \tag{3.55}$$

With respect to the artificial viscosity model, this model derives directly from the discretization of the viscous term in the governing equations, although it doesn't conserve the angular momentum.

3.5.3 Density diffusion terms

One of the drawbacks of the Weakly-Compressible Smoothed Particle Hydrodynamics is the presence of spurious oscillation in the density field at the spatial scale of particles.This issue has been adressed by adding a diffusion term in the continuity equation. In this section, the Density Diffusion Terms used in the present works are presented.

δ-**SPH model** [8]   Molteni and Colagrossi [162] have proposed a diffusive term based on the discretization of the Laplacian of the density field in the form :

$$\mathcal{D}_a = 2hc_0\delta \sum_b \phi_{ab} \frac{\mathbf{r}_{ab} \cdot \nabla W_{ab}}{r_{ab}^2} V_b, \tag{3.56}$$

where $\phi_{ab} = (\rho_a - \rho_b)$ and δ is a tunable parameter that usually is taken in the range $0.3 - 0.1$. This term is consistent, because it goes to 0 as the smoothing length $h \to 0$ and preserves the mass conservation. However, because of the singularity of the Morris formula in the case of truncated support, it diverges in the presence of a free surface. As remedy, in [8] the δ-SPH model has been proposed, suggesting the following expression for ϕ_{ab}:

$$\phi_{ab} = (\rho_a - \rho_b) - \frac{1}{2}\left(\nabla\rho_a^L + \nabla\rho_b^L\right) \cdot \mathbf{r}_{ba}, \tag{3.57}$$

with the renormalized density $\nabla\rho_a^L$ given by:

$$\nabla\rho_a^L = \sum_b (\rho_a - \rho_b)\mathbf{L}_a\nabla_a W_{ab}. \tag{3.58}$$

The renormalization matrix is defined $\mathbf{L}_a$:

$$\mathbf{L}_a = \left[\sum_b (\mathbf{x}_b - \mathbf{x}_a) \otimes W_{ab}\right]^{-1}, \tag{3.59}$$

and restore the first-order consistency also in the presence of boundaries or free-surface that truncate the support. Neverthless, it require the inversion of a matrix 2x2 in 2-D and 3x3 in 3-D for every particles in the computational domain, so the additional computational cost is not negligible.

Green et al. DDT [86] A different approach to stabilize the density field has been proposed in [84] and is used in this work. The basic idea behind this model is to apply a Godunov SPH scheme to the continuity equation and employing a Roe's approximate solver for the Riemann problem at the interface of each neighboring particle. A limiter function is then applied to values of the density obtained in this fashion, so to preserve the monotonicity of the scheme and avoid oscillations in the density field. The diffusive term can ben written as:

$$\mathcal{D}_a = 2c_0 \sum_b \frac{\phi_{ab}}{||\mathbf{x}_a - \mathbf{x}_b||} \frac{\partial W}{\partial q}V_b. \tag{3.60}$$

ϕ_{ab} is now defined as:

$$\phi_{ab} = B_{ab} \left[(\rho_a - \rho_b) - \frac{1}{2}(\xi_{ab}\nabla\rho_a^C + \xi_{ba}\nabla\rho_b^C)(\mathbf{x}_a - \mathbf{x}_b) \right], \qquad (3.61)$$

where:

$$B_{ab} = \frac{||\mathbf{x}_a - \mathbf{x}_b||}{h} \frac{2\rho_a}{\rho_a^r + \rho_b^r}. \qquad (3.62)$$

With respect to Equation (3.57), the tuning parameter δ is now absent and the magnitude of the diffusion introduced in the governing equations is now automatically adjusted by the definition of reconstructed density values:

$$\rho_a^r = \rho_a + \frac{1}{2}\xi(\eta)\nabla\rho_{ab}^C \cdot (\mathbf{x}_b - \mathbf{x}_a), \qquad (3.63)$$

where $\nabla\rho_{ab}^C$ is a corrected SPH approximation of the density gradient and $\xi(\eta)$ is the limiter function, with η defined as:

$$\eta = \frac{\nabla\rho_{ab} \cdot (\mathbf{x}_a - \mathbf{x}_b)}{\rho_b - \rho_a}. \qquad (3.64)$$

Following the indications in [84], the limiter function chosen in this work is the Van Albada [252]:

$$\xi(\eta) = \frac{\eta^2 + \eta}{\eta^2 + 1}. \qquad (3.65)$$

It can be seen that, assuming $\xi_{ab} = \xi_{ba} = 1.0$ and noticing that $B_{ab} \approx 0.5$, this formulation is very similar to Equation 3.57.

Fourtakas et al. DDT [75] Fourtakas et al. [75] have proposed a new density diffusion model that is able to maintain the hydrostatic solution while avoiding the computation of the renormalized density gradient. The main concept is to compute the Laplacian of the density field by neglecting the hydrostatic contribution. In fact:

$$\mathcal{D}_a = \delta h c_0 \sum_b \psi_{ab} \cdot \nabla_a W_{ab} V_b \qquad (3.66)$$

where ψ_{ab} is equal to:

$$\psi_{ab} = 2(\rho_{ba}^T - \rho_{ab}^H)\frac{\mathbf{x}_{ab}}{||\mathbf{x}_{ab}||}, \tag{3.67}$$

where the superscript T and H refers to the total and to the hydrostatic part of the density. The hydrostatic density difference can be obtained by:

$$\rho_{ab}^H = \rho_0 \left(\sqrt[\gamma]{\frac{P_{ab}^H + 1}{C_B}} - 1 \right) \tag{3.68}$$

where P_{ab}^H is the hydrostatic pressure difference:

$$P_{ab}^H = \rho_0 g z_{ab} \tag{3.69}$$

and $C_B = \frac{c_0^2 \rho_0}{\gamma}$.

3.6   Particle Shifting

An important issue of the SPH method is the formation of *void* regions, especially in the presence of strong vortex structures, that can affect the stability and accuracy of the numerical solution.

This problem has been addressed in [134], where the Particle Shifting Technique (PST) has been proposed: the basic concept is to shift the position of the particles to ensure a more uniform distribution by modelling the shifting $\delta\mathbf{x}$ applied to the particle position with a Fickian law based on the gradient of the concentration C, in the form:

$$\delta\mathbf{x} = -D\nabla C \tag{3.70}$$

where D is the diffusion coefficient defined as:

$$D = Ah^2. \tag{3.71}$$

Here, A is a dimensionless constant that is tuned based on the particular problem, and h is the smoothing length.

The gradient of concentration ∇C is calculated using an SPH discretization of the gradient given by:

$$\nabla C = \sum_b \frac{m_b}{\rho_b} \nabla_a W_{ab}. \tag{3.72}$$

In the presence of a free surface, the SPH discretization in Equation (3.72) is inaccurate due to the truncated support, resulting in an upward motion of the particles from the bulk of the flow. To address this issue, in [134], only the tangential component is retained at the free surface while the particle shifting is neglected in the normal direction:

$$\delta \mathbf{x} = \begin{cases} 0 & \nabla \cdot \mathbf{r} \leq A_{FSM}, \\ (\bar{\bar{\mathbf{I}}} - \bar{\mathbf{n}} \otimes \bar{\mathbf{n}}) \delta x & A_{FST} \leq \nabla \cdot \mathbf{r} \leq A_{FSM}, \\ \delta x & \nabla \cdot \mathbf{r} \geq A_{FST}, \end{cases} \tag{3.73}$$

In the previous expression, $\bar{\bar{\mathbf{I}}}$ is the second order identity tensor and $\bar{\mathbf{n}}$ is the normal at the free surfaces estimated as:

$$\bar{\mathbf{n}} = -\frac{\nabla C}{||\nabla C||}. \tag{3.74}$$

For detecting the free-surface interface, the method proposed by [125], based on the particle position divergence, is used:

$$\nabla \cdot \mathbf{r}_a = \sum_b V_b \mathbf{r}_{ab} \cdot \nabla_a W_{ab} \tag{3.75}$$

with A_{FSM} and A_{FST} equal respectively to 1.1 and 1.7 in 2-D and 2.1 and 2.8 in 3-D.

ALE corrective terms The shifting formulation with the ALE corrective terms is given by [237]:

$$\frac{d\rho_a}{dt} = \sum_b \left[\frac{\rho_a}{\rho_b} m_b (\mathbf{v}_{ab} + \delta\mathbf{v}_{ab}) \cdot \nabla\mathbf{W}_{ab} + \frac{m_b}{\rho_b}(\rho_a\delta\mathbf{v}_a + \rho_b\delta\mathbf{v}_b) \cdot \nabla\mathbf{W}_{ab} \right] - \mathcal{D}_a, \quad (3.76)$$

$$\frac{d\mathbf{v}_a}{dt} = \sum_b \left[m_b \left(\frac{P_b + P_a}{\rho_a\rho_b} \right) \nabla\mathbf{W}_{ab} + (\mathbf{v}_a \otimes \delta\mathbf{v}_a + \mathbf{v}_b \otimes \delta\mathbf{v}_b) \cdot \nabla\mathbf{W}_{ab} + \right.$$

$$\left. + \mathbf{v}_a(\delta\mathbf{v}_a - \delta\mathbf{v}_b) \cdot \nabla\mathbf{W}_{ab} \right] + \Gamma_a, \tag{3.77}$$

$$\frac{d\mathbf{x_a}}{dt} = \mathbf{v}_a + \delta\mathbf{v}_a. \tag{3.78}$$

3.7 Solid Boundary Treatment

In this work are used the modified Dynamic Boundary Condition (mDBC), proposed in [66], for the definition of solid boundary conditions. This approach is a modification of the Dynamic Boundary Condition (DBC) to address the issue of the unphysical gap between the dummy particles and the fluid particles. In the DBC formulation, a set of dummy particles that represent the solid interface are placed in the computational domain. Their velocity is set to zero, while their density is evolved by using the SPH continuity equation. In this way, when fluid particles come closer to the solid particles, the density and the pressure of the former increase, generating a repulsive force over the fluid particles. However, as discussed in [60], this repulsive mechanism creates a gap in the order of the smoothing length so that there is an incorrect definition of the solid interface that either must be considered prior to placing the solid boundary particles, or after when the in the post-processing of the results.

In the mDBC, as in the Ghost Particle approach [149], for each boundary particle, a ghost node is created by mirroring the position of the solid boundary along the solid-fluid interface (Figure 3.2). Once the position of the ghost node is defined, the density and its gradient are computed at the ghost node adoption a corrected SPH operator [140]. This operator consist in the solution opf the following
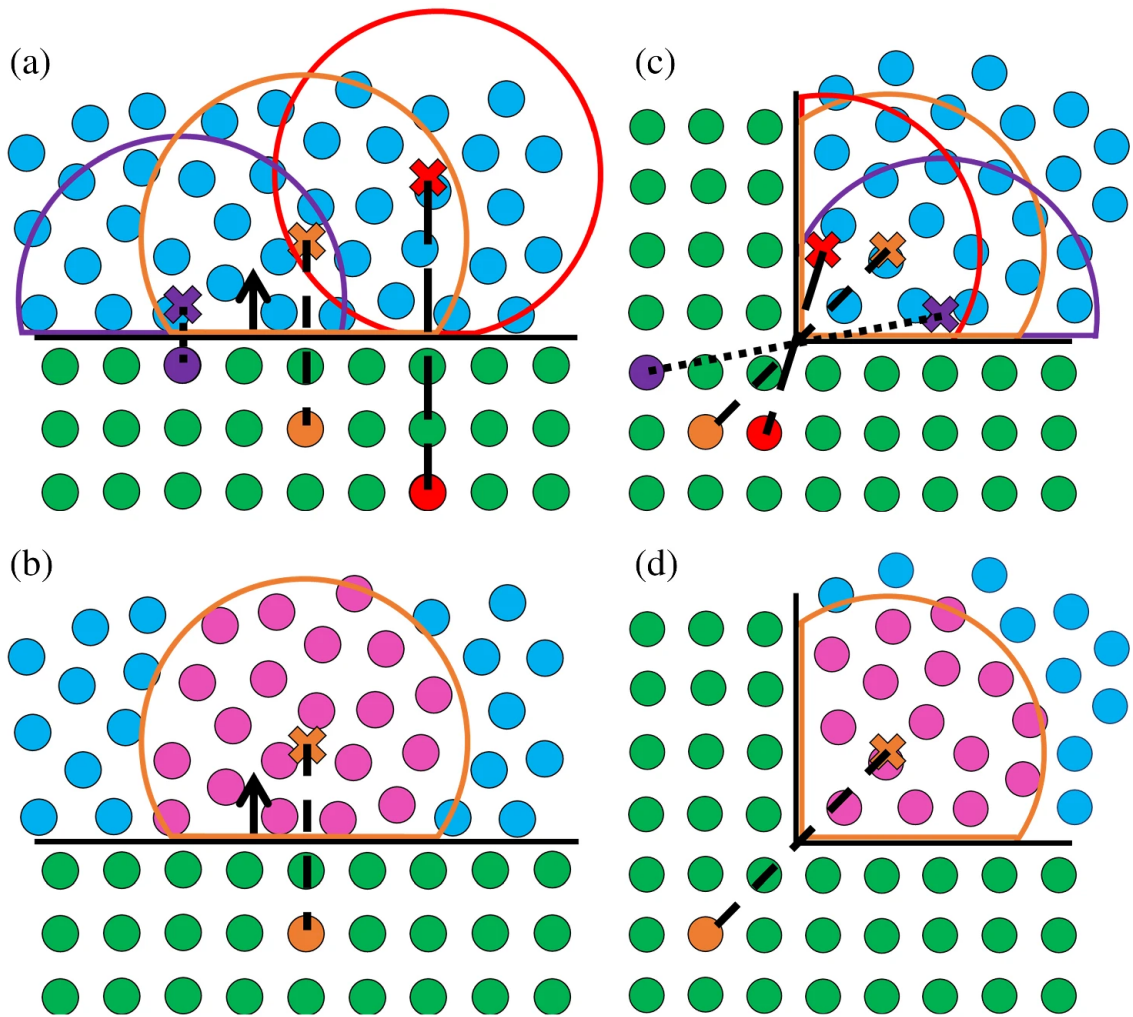
Figure 3.2 Mirroring of ghost nodes (crosses) and the kernel radius around the ghost nodes for boundary particles in a flat surface (a) and a corner (c). Fluid particles (pink) included in the kernel sum around ghost nodes for boundary particles in a flat surface (b) and a corner (d) [66].

linear system

$$\mathbf{A f} = \mathbf{b}$$

$$b_m = \sum_b f_b w_m V_b$$

$$A_{mn} = \sum_b w_m r_n V_b$$

$$w_m = \begin{bmatrix} W_{gb} & W_{gb}^x & W_{gb}^y & W_{gb}^z \end{bmatrix}$$

$$r_n = \begin{bmatrix} 1 & x_{gb} & y_{gb} & z_{gb} \end{bmatrix}$$

$$\mathbf{f} = \begin{bmatrix} \rho_g & \rho_g^x & \rho_g^y & \rho_g^z \end{bmatrix}$$

(3.79)

where ρ_g and ρ_g^i are the density and its gradient at the ghost node g.

Then, the density at the boundary particle is found through:

$$\rho_b = \rho_g + (\mathbf{r}_b - \mathbf{r}_g) \cdot \begin{bmatrix} \rho_g & \rho_g^x & \rho_g^y & \rho_g^z \end{bmatrix}$$

(3.80)

In case the matrix $\mathbf{A}$ is ill-conditioned, due to an insufficient number of particles, instead of Equation (3.79), the density is calculated with a Shepard correction:

$$\rho_g = \frac{\sum_b \rho_g W_{gb} V_b}{\sum_b W_{gb} V_b}$$

(3.81)

For the velocity $\mathbf{u}_b$, are enforce no-slip condition by an symmetric reflection along the solid interface:

$$\mathbf{u}_b = 2\mathbf{u}_s - \mathbf{u}_g$$

(3.82)

where $\mathbf{u}_s$ is the velocity of the solid interface, and $\mathbf{u}_g$ is the velocity at the ghost node calculated as:

$$\mathbf{u}_g = \frac{\sum_b \mathbf{u}_g W_{gb} V_b}{\sum_b W_{gb} V_b}.$$

(3.83)

3.8 Time Stepping Scheme

In this work presented later, a second-order symplectic predictor-corrector [127] is employed as time scheme:

$$
\begin{aligned}
\rho_a^{n+\frac{1}{2}} &= \rho_a^n + \frac{\Delta t}{2} M_a^n, \\
\mathbf{v}_a^{n+\frac{1}{2}} &= \mathbf{v}^n + \frac{\Delta t}{2} F_a^n, \\
\mathbf{x}_a^{n+\frac{1}{2}} &= \mathbf{x}^n + \frac{\Delta t}{2} \mathbf{v}_a^n, \\
\rho_a^{n+1} &= \rho_a^n \left(\frac{2-\epsilon}{2+\epsilon} \right) ; \epsilon = -\Delta t \left(\frac{M_a^n}{\rho_a} \right)^{\frac{1}{2}}, \\
\mathbf{v}_a^{n+1} &= \mathbf{v}^n + \frac{\Delta t}{2} F_a^{n+\frac{1}{2}}, \\
\mathbf{x}_a^{n+1} &= \mathbf{x}^n + \frac{\Delta t}{2} (\mathbf{v}_a^n + \mathbf{v}_a^{n+1}) + \delta x,
\end{aligned}
\tag{3.84}
$$

where δx is the particle shifting obtained with Equation (3.70).

The time-step is chosen according to the following CFL condition:

$$
\Delta t = C_{\text{CFL}} \min(\Delta t_f, \Delta t_{cv}),
\tag{3.85}
$$

where:

$$
\Delta t_f = \min_a \sqrt{\frac{h}{F_a}},
\tag{3.86}
$$

$$
\Delta t_{cv} = \min_a \frac{h}{c_0 + \max_b \left| h \frac{(\mathbf{v}_b - \mathbf{v}_a) \cdot (\mathbf{x}_b - \mathbf{x}_a)}{(\mathbf{x}_b - \mathbf{x}_a)^2} \right|}.
\tag{3.87}
$$

CHAPTER 4

SPH SOLUTION OF TURBULENT FLOWS

This chapter addresses the numerical simulation of isotropic turbulence with the SPH schemes.

After a brief assessment of the order of accuracy of the Eulerian SPH formulation, a decaying isotropic turbulent flow in a triple periodic box, the well-known three-dimensional Taylor Green Vortex (TGV), is simulated using a Direct Numerical Simulation approach. The focus has been directed toward two aspects that have been poorly addressed in the literature:

- the influence of the discretization error on the accuracy of the solution. To perform this study, the Lagrangian and the Eulerian formulation, introduced in Chapter 3, are compared. The Eulerian model, using a uniform fixed particle arrangement fixed in time, is free from the error introduced by the discrete SPH operator.

- The effect of a Density Diffusive Term [84] on the accuracy.

In the second part of the chapter, forced isotropic turbulence in a triple periodic is studied to assess the accuracy of SPH schemes for sustained turbulence flow. The focus is shifted towards the impact of different Particle Shifting Techniques over the numerical solution.

In the final section, the three-dimensional Taylor-Green vortex is once again simulated to explore and assess high-order SPH schemes for the numerical computation of turbulence flows.

4.1 Accuracy of the Eulerian SPH formulation

A two-dimensional Taylor-Green Vortex is simulated to investigate the order of accuracy of the Eulerian SPH method. The analytical solution for the velocity and the pressure field is:

$$u = e^{-8\pi^2 \nu t} U_\infty \sin(2\pi x) \cos(2\pi x),$$

$$v = -e^{-8\pi^2 \nu t} U_\infty \cos(2\pi x) \sin(2\pi y), \tag{4.1}$$

$$p = e^{-16\pi^2 \nu t} \frac{1}{2} (\cos(4\pi x) + \cos(4\pi y).$$

The Reynolds number is set to $\mathrm{Re} = U_\infty L / \nu = 100$ by using a reference velocity $U_\infty = 1$, reference length $L = 1$ and a kinematic viscosity $\nu = 0.01$. The smoothing length to particles ration is equal to $h/\Delta x = 2$, the CFL numnber is 0.1 and no DDT is applied. Figure 4.1(a) shows the velocity magnitude for time $t = 1$ and Figure 4.1(b) highlights the convergence ratio through the L_1 error norm for the horizontal component of the velocity. From the latter result, it is possible to confirm that the Eulerian SPH method adopted is indeed second-order accurate in agreement with previous predictions [136], with the exception of the highest resolution case wherein an expected kernel saturation occurs [199].

4.2 Three-dimensional Taylor Green Vortex

The 3-D Taylor-Green vortex (TGV) problem is a well-known flow that simulated the free decay of isotropic turbulence in a triple periodic box. It has been used extensively as a benchmark for the validation of numerical schemes and turbulence models. This choice is mainly motivated by two reasons:

- the extensive availability of literature results on the subject [28, 226, 65, 222].

- The simple geometry that doesn't involve solid boundaries and, due to the periodicity of the computational domain, is very suitable for numerical scheme that are formulated in a Fourier's space.
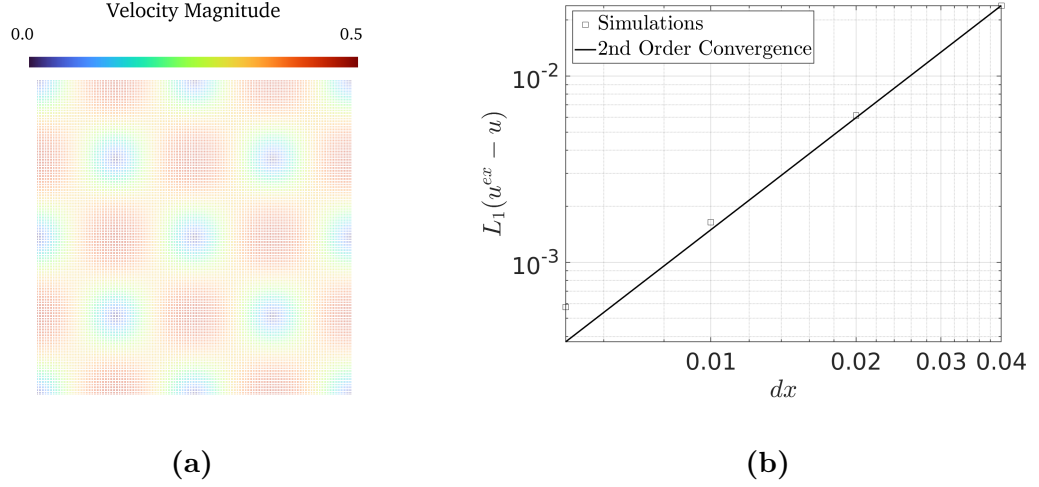
Figure 4.1 (a) Contours of dimensionless velocity magnitude, and (b) convergence analysis for the two dimensional Taylor-Green Vortex with Re=100 at t=5s.

In this work the initial conditions for the velocity and pressure fields are [253]:

$$
\begin{aligned}
u &= U_0 \sin(x/L) \cos(y/L) \cos(z/L), \\
v &= -U_0 \cos(x/L) \sin(y/L) \cos(z/L), \\
w &= 0, \\
p &= \frac{1}{16}(\cos(2x/L) + \cos(2y/L))(\cos(2z/L) + 2),
\end{aligned}
\tag{4.2}
$$

with $x, y, z \in [-\pi L, \pi L]$.

For the assessment of the results, the following integral quantities have been studied:

- The time history of the kinetic energy defined as:

$$
E_k = \frac{1}{\rho_0 \Omega} \int_\Omega \rho \frac{\mathbf{v} \cdot \mathbf{v}}{2} d\Omega
\tag{4.3}
$$

- The dissipation rate of the kinetic energy:

$$
\epsilon = -\frac{dE_k}{dt}
\tag{4.4}
$$

- The time history of the enstrophy:

$$\mathcal{E} = \frac{1}{\rho_0 \Omega} \int_\Omega \rho \frac{\boldsymbol{\omega} \cdot \boldsymbol{\omega}}{2} d\Omega \tag{4.5}$$

where $\boldsymbol{\omega}$ is the vorticity and Ω is the support domain.

For incompressible flow, a relationship between the dissipation rate and the enstrophy exists as:

$$\epsilon = -2\nu \mathcal{E} \tag{4.6}$$

The time is non-dimensionalized as $\frac{L}{U_0}$, the kinetic energy by dividing by U_0^2 and the enstrophy as ϵ by $\frac{U_0^2}{L^2}$.

The evolution of the three-dimensional Taylor-Green Vortex flow is shown in Figure 4.2, where the iso-contours ($Q = 1$) of the Q-criterion are reported. The initial vortex distribution shown in Figure 4.2(a) is followed by the vortex roll-up in Figure 4.2(b), until the maximum dissipation rate is reached during the breakdown of the vortices [Figure 4.2(c)]. The flow then evolves and becomes fully turbulent, with the creation of smaller turbulent structures [Figure 4.2(d)-4.2(f)].

4.3   Isotropic Turbulence Decay

4.3.1   Case setup

A great challenge when simulating a TGV with Lagrangian SPH is encountered during the breakdown of the initial vortex distribution, during which the particles are displaced anisotropically, leading to a loss of accuracy of the SPH interpolation.

Figure 4.3 shows the velocity magnitude for the Taylor-Green Vortex at Re=1600, with an initial interparticle particle distance set to $0.01L$. If particles are initially placed on a Cartesian lattice, as for example in Figure 4.3(a), large voids appear in the early stage of the flow [Figure 4.3(c)] that subsequently lead to a noisy velocity field [Figure 4.3(e)]. To overcome this issue, we adopted a pseudo-random

(a) $t = 0$ **(b)** $t = 4$

(c) $t = 8$ **(d)** $t = 12$

(e) $t = 16$ **(f)** $t = 20$
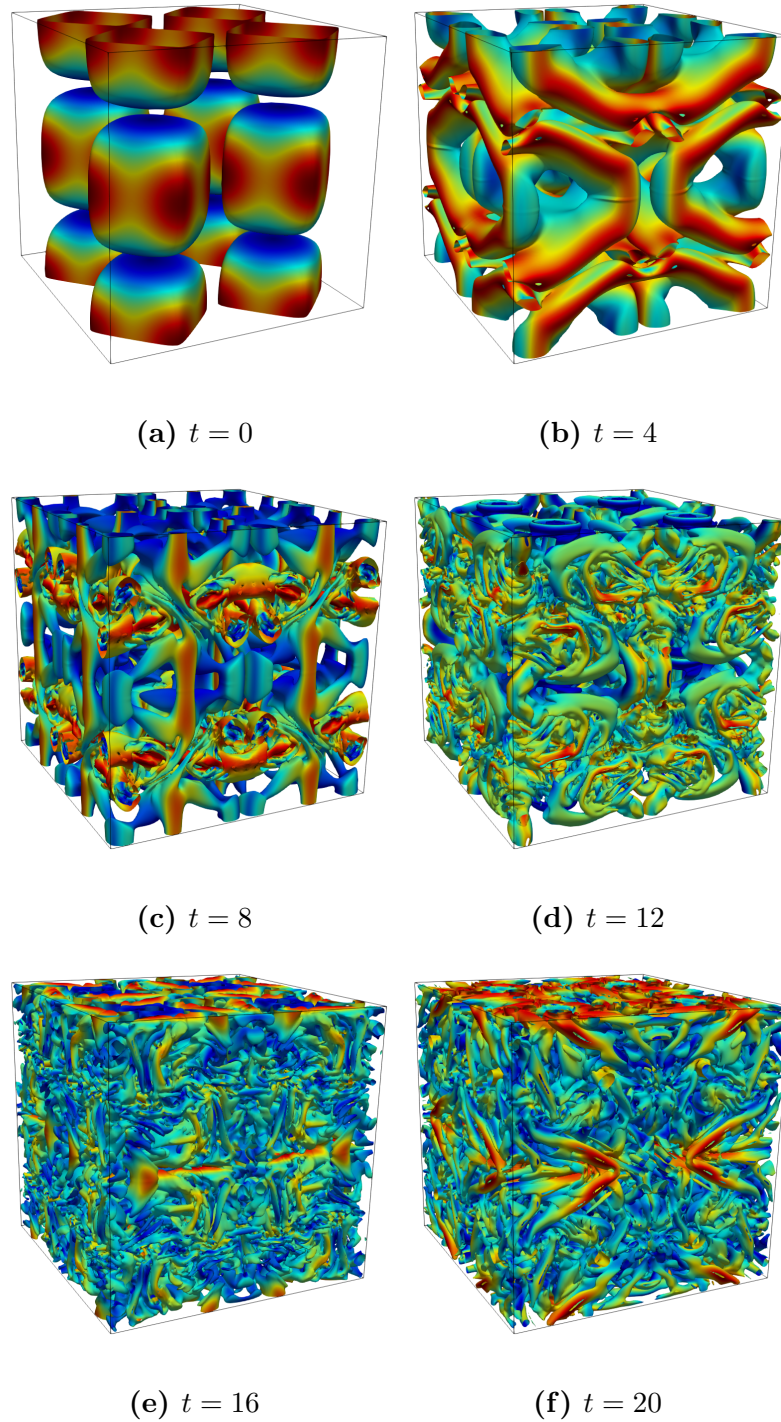
Figure 4.2 3-D Taylor-Green Vortex at $\mathrm{Re} = 1600$ simulated with an Eulerian SPH resolution of 100 particles per initial vortex length. The isocountours represent the Q-criterion $Q = 1$ colored by the velocity magnitude for $t = 0, 4, 8, 12, 16, 20$.
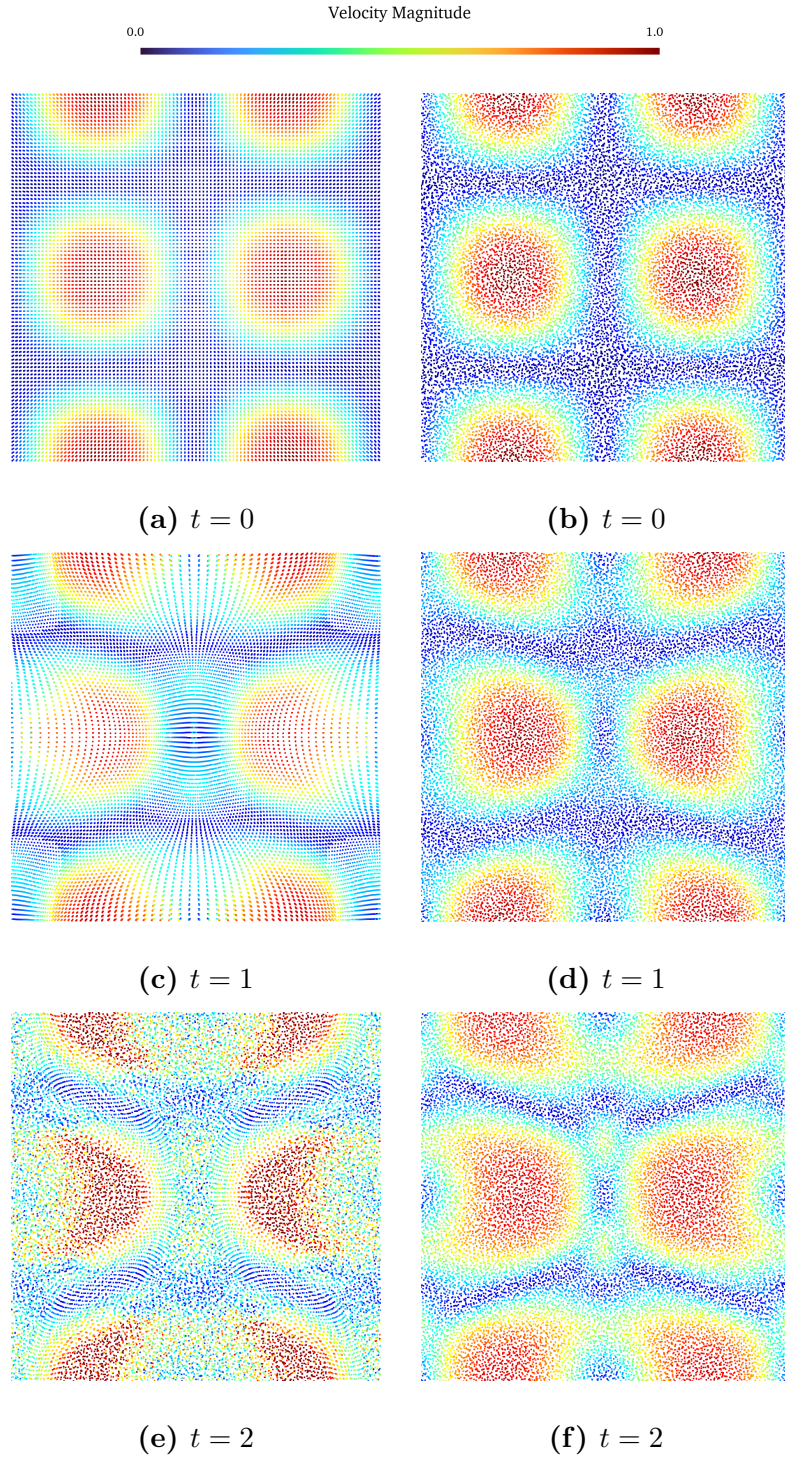
Figure 4.3 Dimensionless velocity magnitude for the Taylor-Green Vortex at Re = 1600 using Lagrangian SPH. (a), (c), (e) Particles initialized on a Cartesian lattice at $t = 0, 1, 2$, respectively. (b), (d), (f) Particles initialized with a random-like distribution at $t = 0, 1, 2$, respectively.

initial particle distribution generated by a preliminary simulation of the same test case. This approach is similar to the one proposed by Colagrossi et al. [44]. This initialization, shown in Figure 4.3(b), allows to bypass the aforementioned problems and to obtain a much smoother velocity field [Figure 4.3(d),4.3(f)]. Specifically, when using a random-like initial distribution over a Cartesian one, a smaller dissipation is observed at the beginning of the simulation as shown in Figure 4.4(a). This difference between the two initializations seems to lose significance with increasing values of the kernel support. However, using a larger kernel support leads to a larger smoothing error for the SPH spatial operators, therefore this could be detrimental in the latter stages when turbulent structures become much smaller and are at risk of being smoothed out artificially. To verify this and to ultimately choose an optimal initial setup, a sensitivity analysis is performed to assess the effect of the smoothing-length-to-particle-spacing ratio, h/dp, on the numerical solution. The results are depicted in Figure 4.4(b) and indicate that values of $h/dp > 1.5$ produce worse results for a given dp, especially for $t > 5$ when the initial vortices are broken into smaller structures. For this reason, a value of $h/dp = 1.5$ is chosen and kept fixed in all simulations hereafter. Moreover, to satisfy the weakly compressibility assumption, the speed of sound is chosen to be $c_0 = 10 \cdot v_{\text{max}}$, limiting the density variations to 1% of the reference density.

4.3.2 Eulerian SPH

Figure 4.5(a) shows the history of the kinetic energy for Re = 1600 with the Eulerian SPH model deprived of any diffusive terms in the continuity equation, i.e., Equation (3.49), and for 64^3, 128^3, 256^3 and 512^3 computational nodes. It is remarked that for this Reynolds number, a rough estimation of the ratio between the Kolmogorov length [Equation (2.3)] scale and the reference length gives $L/\eta \approx 250$, indicating that the two finest resolutions adopted in this study are able to resolve the smallest
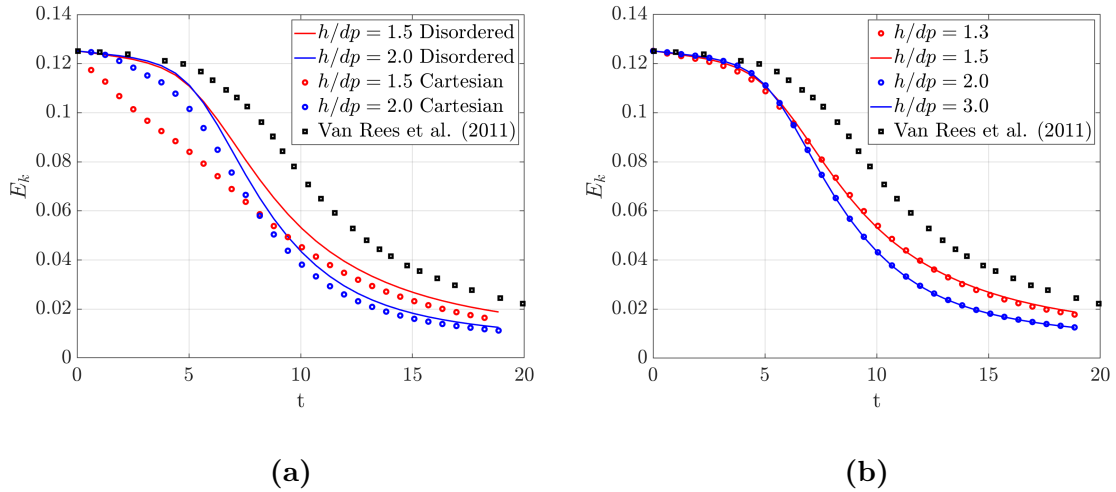
Figure 4.4 (a) Effect of the initial particle distribution on the decay of the kinetic energy for the 3-D Taylor-Green Vortex at Re = 1600 with two values of the smoothing-length-to-particle-spacing ratio, i.e., $h/dp = 1.5$ and 2.0. (b) Effect of the smoothing-length-to-particle-spacing ratio on the decay of the kinetic energy for the 3-D Taylor-Green Vortex at Re = 1600 with a random-like particle initial distribution.

scales of motion. Results are in good agreement with the high-order pseudo-spectral solution by Van Rees et al. (2011) [253], especially for the finest resolution, for which the grid independence is almost achieved. In Figure 4.5(b), the time history of the enstrophy is reported for the same set of simulations. It is possible to observe that the numerical solution is converging towards the reference solution with the increase of the resolution.

4.3.3 Lagrangian SPH

The same test case as in the previous section is simulated here using Lagrangian SPH without any diffusive terms added to the continuity equation. Looking at the kinetic energy decay in Figure 4.6(a), the solution is also converging, however, an excessive dissipation is observed when the process of vortex roll-up starts, i.e., for $3 \leq t \leq 6$. A comparison with the previous Eulerian SPH results suggests that this over-diffusion could be due to the disorder in the SPH particle distribution, which leads to low accuracy of the SPH spatial operators. This over-diffusion causes the
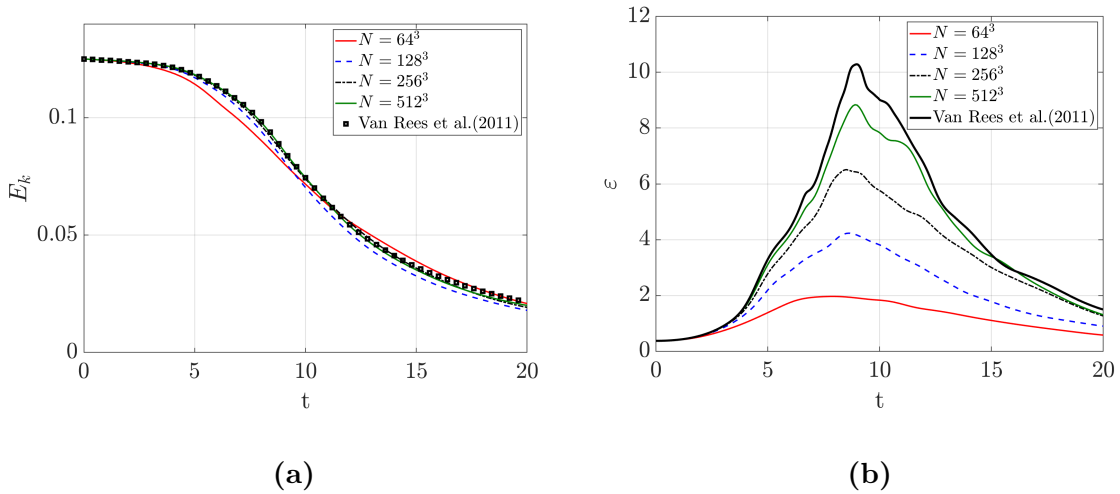
Figure 4.5 (a) Time history of the kinetic energy and (b) time history of the enstrophy for the 3-D Taylor-Green Vortex at Re = 1600 simulated with Eulerian SPH using 64^3, 128^3, 256^3 and 512^3 particles. SPH results are compared to the reference solution in Van Rees et al. (2011) [253].

early breakdown of the initial vortices, and a discrepancy with the reference solution is thus observed [Figure 4.6(a)]. As can be seen in Figure 4.6(b), this also causes a poor agreement between SPH and the DNS solution in Van Rees et al. (2011) [253] for what concerns the time evolution of the enstrophy. When comparing the Eulerian and Lagrangian results from Figures 4.5(b) and 4.6(b), respectively, the latter severely underestimates the peak value, remarking the lower order of accuracy of Lagrangian SPH due to the poorer particle distribution.

4.3.4 Influence of the dissipation model

Additional simulations of the same 3-D Taylor-Green Vortex case are presented here with the adoption of the density diffusion term (DDT) by Green et al. (2019) [84] in the Lagrangian SPH simulations. In Figure 4.7(a), the solutions with and without the DDT are compared for 512^3 particles in the computational domain, revealing a negligible effect of the diffusion term from the standpoint of the time history of the flow kinetic energy. However, when looking at the time evolution of the enstrophy [Figure 4.7(b)], the addition of the Green et al. (2019) [84] DDT in the continuity
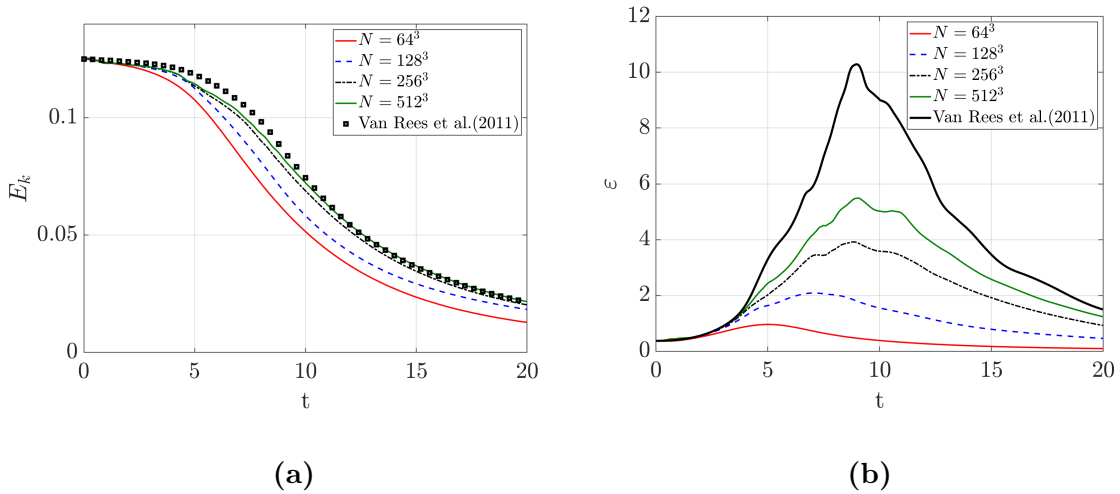
Figure 4.6 (a) History of the kinetic energy and (b) of the enstrophy for the Taylor-Green Vortex at $Re = 1600$ for resolutions of 64^3, 128^3, 256^3 and 512^3 particles with the Lagrangian SPH formulation. Numerical results are compared to the reference solution in Van Rees et al. (2011) [253].

equation is able to yield a higher peak value with respect to the standard Lagrangian SPH, likely due to the less noisy density field which leads to an improvement of the accuracy for this test case.

This is confirmed when looking at the contours of the density field in Figure 4.8(a), where it can be clearly seen that when using a Lagrangian SPH model without any dissipation, the density field appears dominated by strong numerical noise. Instead, when the Green et al. (2019) [84] DDT is enabled [Figure 4.8(b)], a much smoother density field is obtained. This effect can also explain the differences between the turbulent energy spectra displayed in Figure 4.9, where for wave numbers in the range of the kernel radius size, the Lagrangian SPH without any DDT shows a spurious flattening, which is instead significantly reduced when the DDT is enabled. Moreover, the Eulerian SPH is capable of computing the spectrum correctly across the whole range of frequencies.
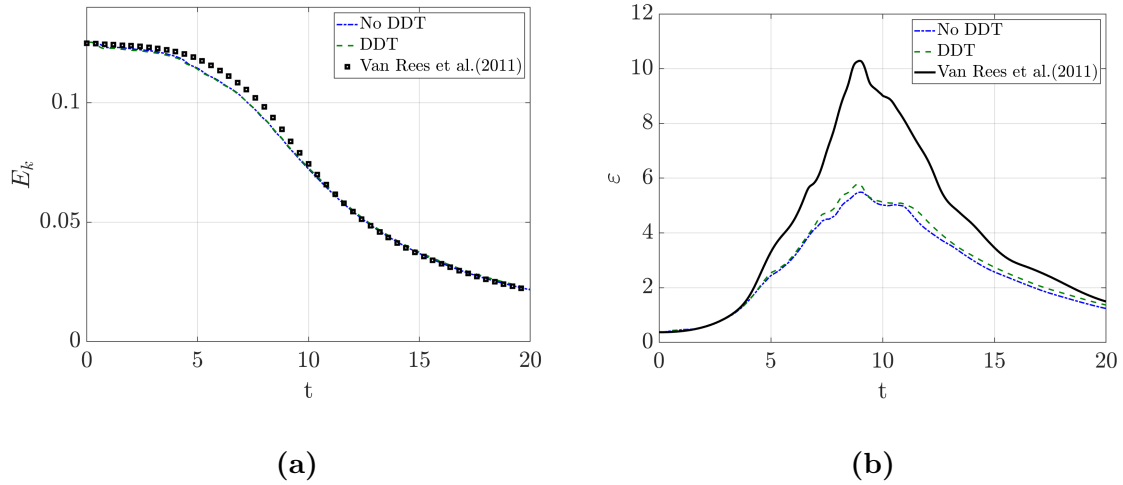
Figure 4.7 (a) Time history of the kinetic energy and (b) time history of the enstrophy for the 3-D Taylor-Green Vortex at $Re = 1600$ simulated with 512^3 particles and with a Lagrangian SPH formulation with and without the Green et al. (2019) [84] diffusive term. Numerical results are compared against the reference solution in Van Rees et al. (2011) [253].
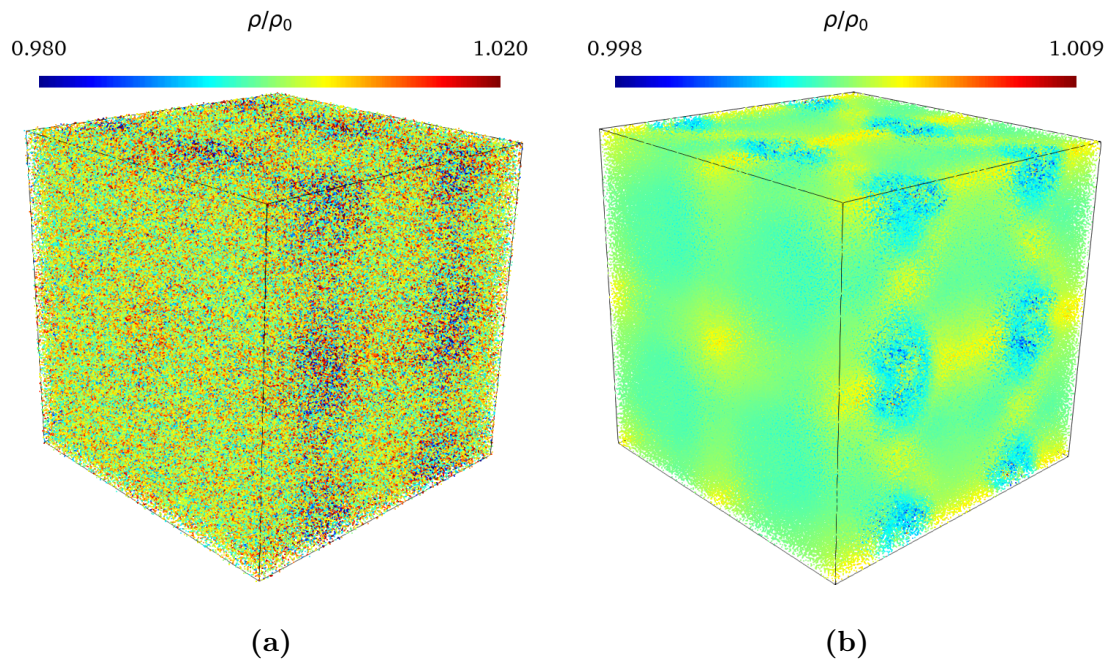
Figure 4.8 Density field at $t = 7$ for 3-D Taylor-Green Vortex at Re = 1600: (a) Lagrangian SPH with no dissipation; (b) Lagrangian SPH with the Green et al. (2019) [84] diffusive term enabled.
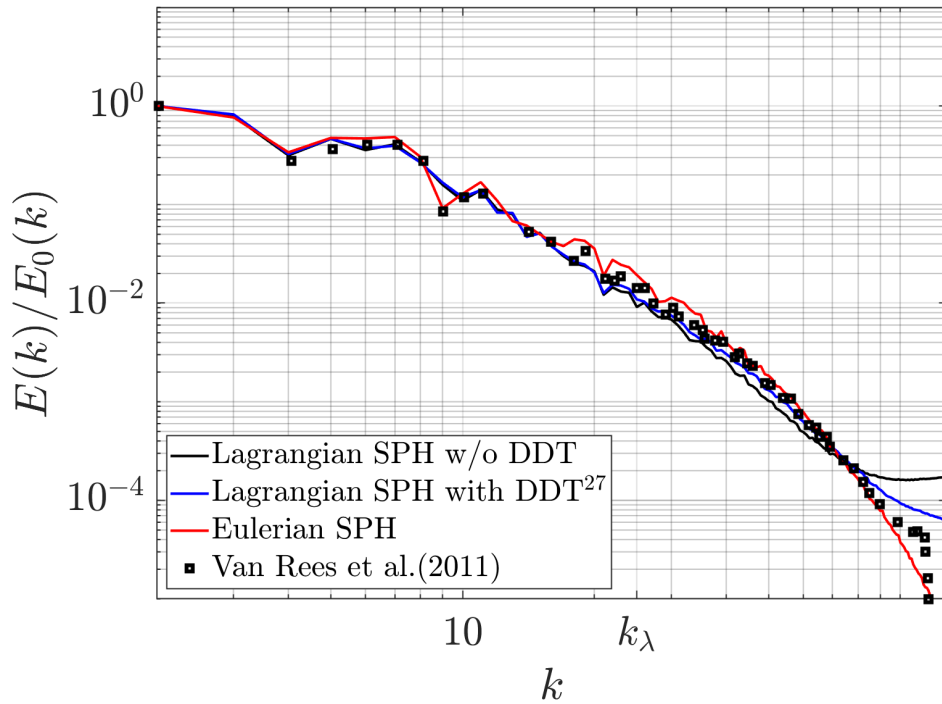
Figure 4.9 Turbulent energy spectra for the 3-D Taylor-Green Vortex at Re = 1600 with 512^3 particles in the domain and with Eulerian SPH, and Lagrangian SPH with and without the Green et al. (2019) [84] dissipation term. Numerical results are compared against the reference solution in Van Rees et al. (2011) [253].

4.4 Forced Isotropic Turbulence

The performance of the above models is evaluated here for an isotropic turbulent flow in a triple periodic box with a linear forcing term added to the momentum equation:

$$\frac{d\mathbf{v}}{dt} = -\frac{\nabla P}{\rho} + \nu\nabla^2\mathbf{v} + A\mathbf{v}, \tag{4.7}$$

where A is the forcing constant. This particular test case is chosen to assess the stability and robustness of the above schemes when simulating long periods of physical time, which has been possible to solve mainly thanks to the highly parallel performance of the DualSPHysics code [62]. When compared to a more traditional band-limited forcing, a linear forcing injects energy at all scales of motion but is capable of achieving a stationary state with an energy spectrum as good as band-limited forcing [212]. A solenoidal velocity field peaking at a wavenumber of $k_0 = 2$ has been chosen as the initial condition [212]. As discussed by Rosales and Meneveau (2005) [212], the initial velocity field has no influence over the stationary solution which depends only on the A constant of Equation (4.7) and on the size do the domain. As for the previous test case, simulations have been performed with both the Lagrangian and Eulerian SPH schemes with and without the density diffusion term of Equation (3.60). A rough estimation of the kolmogorov scales gives $L/\eta \approx 200$, so a resolution with 256^3 is chosen. A list of the different simulations that have been run together with details about the SPH formulation, density diffusion scheme and value of the coefficient A used are summarized in Table 4.1. A resolution of 256^3 particles is used for all cases and the fluid kinematic viscosity is set to $\nu = 9.9471 \times 10^{-5}$

4.4.1 Role of the density diffusion term

Upon tackling the forced isotropic turbulence problem with an Eulerian SPH scheme without any density diffusion term, simulation results have shown to be unstable due to the insurgence of strong oscillations in the density field [Figure 4.10(a)]. This

Table 4.1 Simulation parameters for the Forced Isotropic Turbulence Problem

Case	SPH Formulation	DDT	A
1a	Eulerian	Green et al. (2019)[84]	0.1
2a	Lagrangian	Green et al. (2019)[84]	0.1
3a	Eulerian	Green et al. (2019)[84]	0.3
4a	Lagrangian	Green et al. (2019)[84]	0.3
4b	Lagrangian	Green et al. (2019)[84] + Shift. ALE	0.3
4c	Lagrangian	Green et al. (2019)[84] + Shift.	0.3

numerical noise was not detected in the previous TGV case, and it is probably due to the longer simulation times which bring to light the stability issues of a centered-collocated numerical scheme. To overcome this issue, two different dissipation models have been included in the continuity equation and investigated: the δ-SPH by Antuono et al. (2010)[8] and the Green et al. (2019) [84] models. The contours of the density field obtained with the δ-SPH model[8] with $\delta = 0.1$ are depicted in Figure 4.10(b): a higher level of noise can be seen when compared to the solution obtained with the Green et al. (2019)[84] model [Figure 4.10(c)]. This is also highlighted by the probability distributions of density values in Figure 4.11(a), while the density energy spectra for these three solutions in Figure 4.11(b) indicate that δ-SPH is unable to reproduce the low-mid range scales. Although this issue could be partially mitigated by increasing the value of the δ parameter according to the magnitude of the forcing term, the Green et al. (2019) [84] model appears to be the better choice due to its ability to automatically adjust the amount of introduced dissipation based on local flow conditions. For this reason, this model is included in the continuity equation for all Eulerian and Lagrangian SPH simulations henceforth.
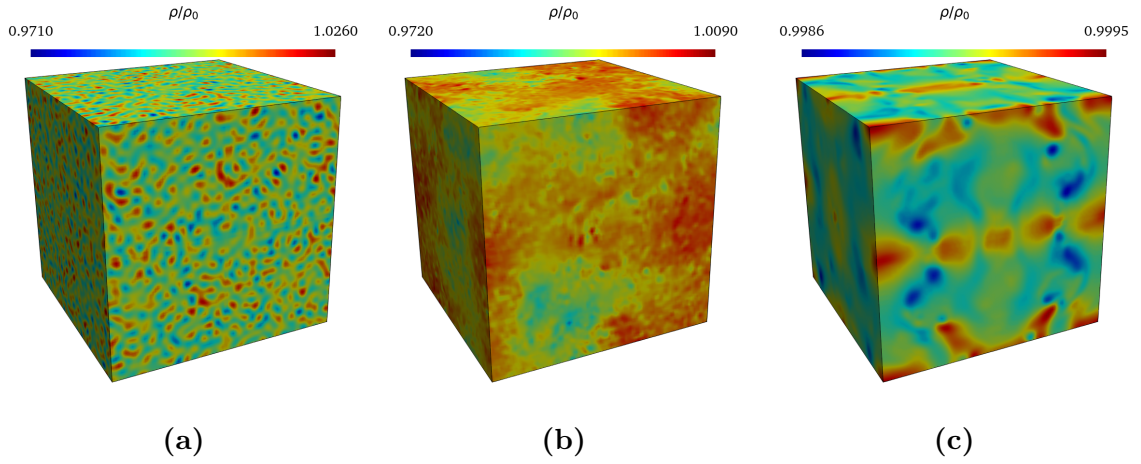
Figure 4.10 Contours of the density field at $t = 9$ for the forced isotropic turbulent cases with $A = 0.1$: (a) Eulerian SPH; (b) Eulerian SPH with the Antuono et al. (2010)[8] dissipation model; (c) Eulerian SPH with the Green et al. (2019)[84] dissipation model.
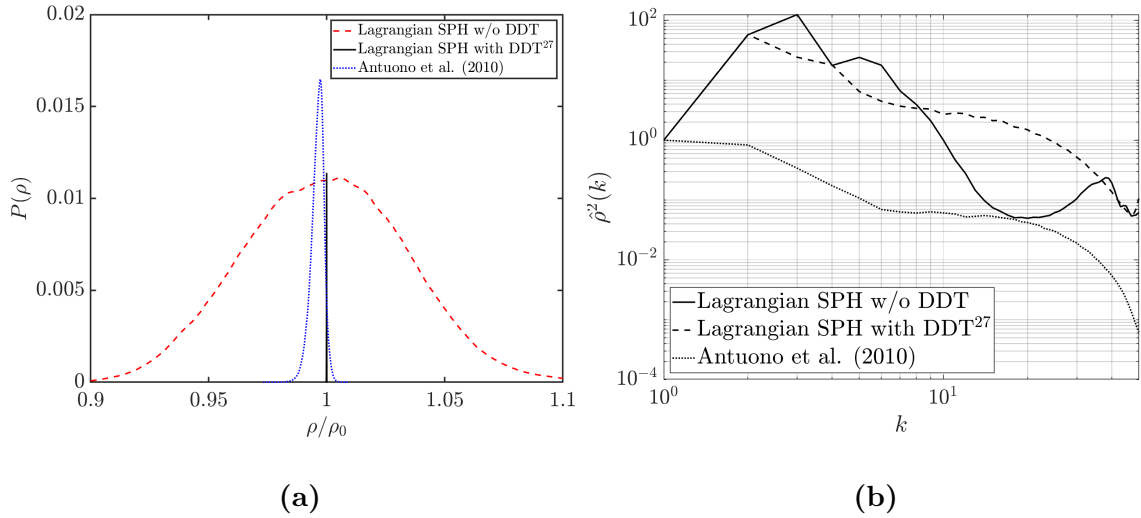
Figure 4.11 Forced isotropic turbulent problem: (a) Probability distribution of the density field, and (b) energy spectra at $t = 9$ for Eulerian SPH, Lagrangian SPH with the Antuono et al. (2010)[8] dissipation model and Lagrangian SPH with the Green et al. (2019)[84] dissipation model.
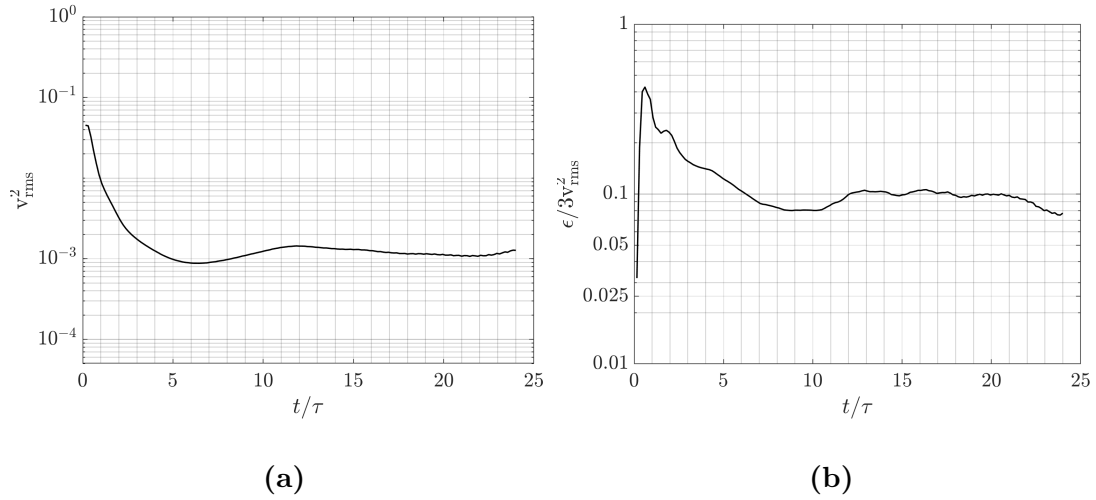
Figure 4.12 (a) Time history of v_{rms}^2, and (b) time history of $\epsilon/3v_{rms}^2$ for Eulerian SPH results of the forced isotropic turbulent problem (case 1a).

4.4.2 Differences between Eulerian and Lagrangian approaches

Two global quantities are defined to investigate the stationary behavior of the problem: the mean square value of the velocity fluctuations, $v_{rms}^2 = \langle \mathbf{v} \cdot \mathbf{v} \rangle /3$, and the eddy turnover time, $\tau = v_{rms}^2/\epsilon$, where $\epsilon = -\nu \langle \mathbf{v} \cdot \nabla^2 \mathbf{v} \rangle$ is the mean dissipation rate. As can be seen in Figure 4.12(a), v_{rms}^2 reaches a stationary value for $t/\tau > 5$ up to 20 eddy turnover times in all the different cases. From the kinetic energy balance of a steady state problem, it is known that the ratio $\epsilon/3v_{rms}^2$ must lie around the value of the parameter A specified in the governing equations. This is corroborated by the time history of $\epsilon/3v_{rms}^2$ in Figure 4.12(b), where the correct value of $A = 1$ is retrieved.

In Figures 4.13(a) and 4.13(b), the results for the same set of simulations are shown when Lagrangian SPH is employed. It can be seen that v_{rms}^2 is slightly less oscillatory for the Lagrangian scheme. This notwithstanding, the differences between the two approaches are not significant and the final values of the mean square value of the velocity fluctuations are almost identical when the stationary solution is reached. As with the Eulerian SPH, also Lagrangian SPH predicts the correct value of $\epsilon/3v_{rms}^2$ well, with a stable result for $t/\tau > 8$ Figure 4.13(b)).
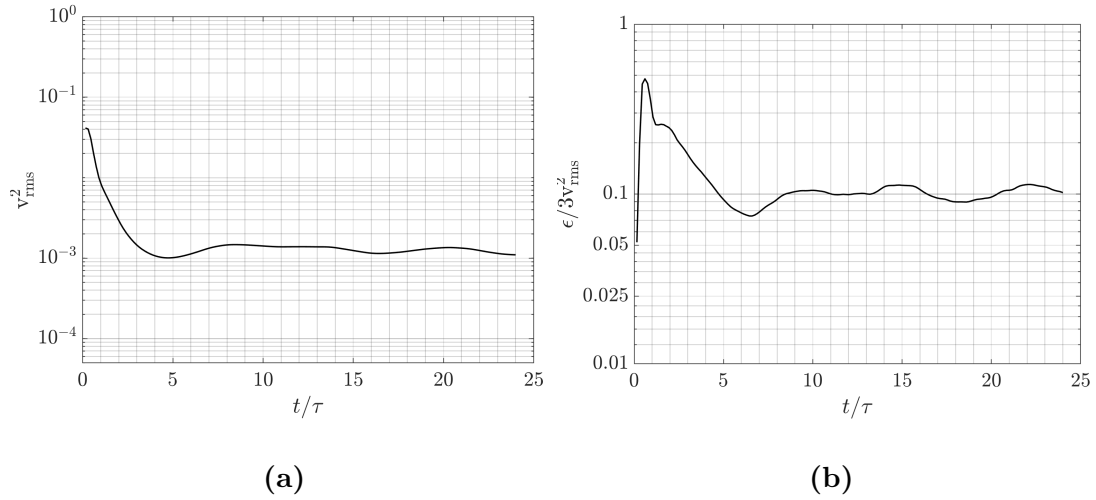
Figure 4.13 (a) Time history of v_{rms}^2, and (b) time history of $\epsilon/3v_{rms}^2$ for Lagrangian SPH results of the forced isotropic turbulent problem (case 2a).

Comparing the density field of cases 1a [Figure 4.14(a)] and 2a [Figure 4.14(c)], it can be noticed how Eulerian SPH returns a smoother density distribution across the domain, and the coherent structures are more distinguishable. However, the noisier density field of Lagrangian SPH simulations is not an obstacle for the correct prediction of the turbulent structures, as seen in Figures 4.14(b) and 4.14(d). The consistency of the two approaches is elucidated in Figure 4.15(a), where the energy spectra are plotted. Cases 1a and 2a are almost identical, although only the Eulerian simulation has an acceptable outcome at high wavenumbers, while the particle disorder in the Lagrangian case causes a spurious flattening. We remark that the Reynolds number based on the Taylor micro-scale λ is $Re_\lambda = 37$, which is too low to show an inertial range. Nonetheless, both SPH curves seem to approach the -5/3 law predicted by the Kolmogorov theory.

4.4.3 Effect of the particle shifting technique and ALE corrective terms

Our last investigation focuses on the performance of Eulerian and Lagrangian SPH models in more critical conditions. This is done by tripling the magnitude of the linear forcing coefficient, i.e. $A = 0.3$. In Figure 4.16(a), the iso-contours of ∇C are
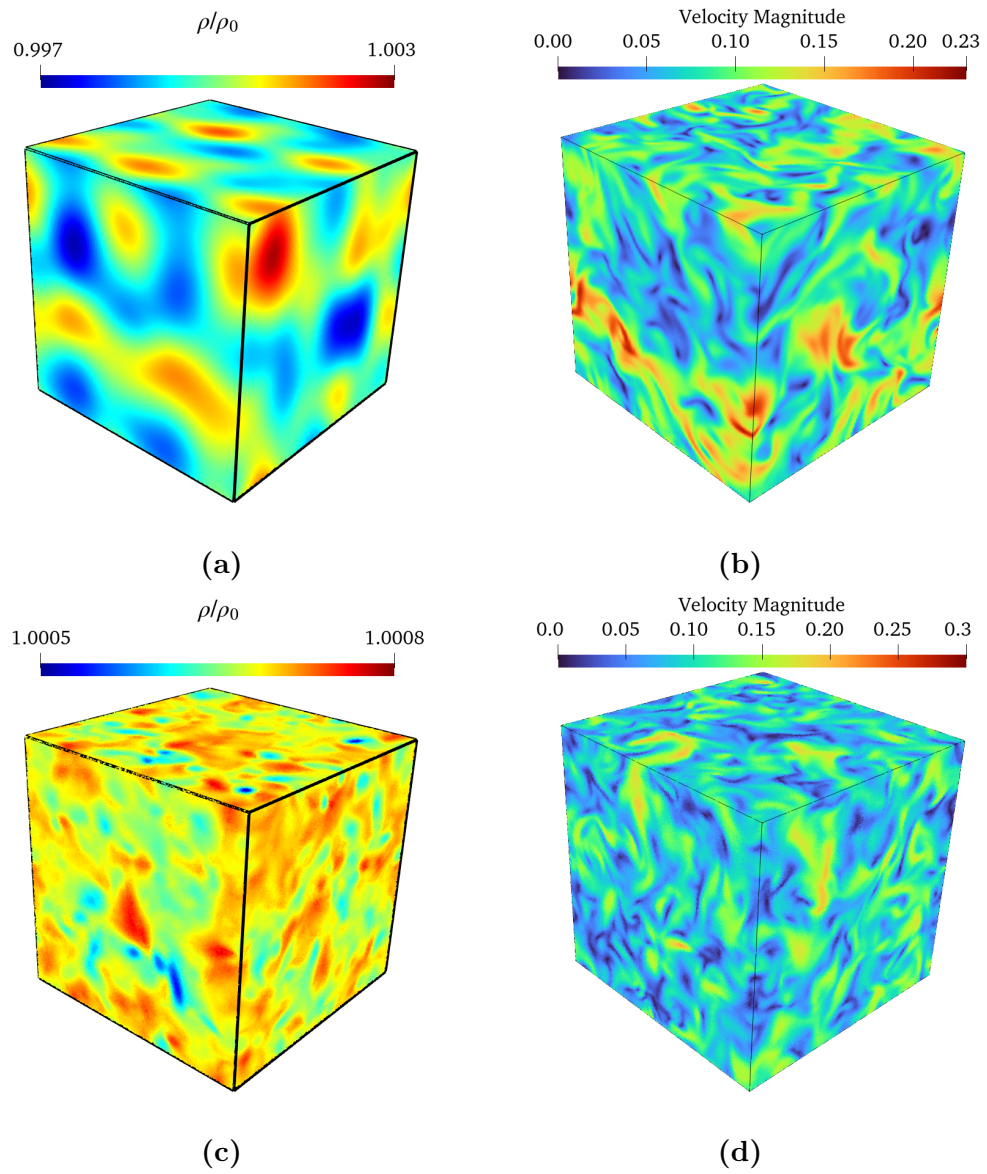
Figure 4.14 Eulerian (top panels, case 1a) and Lagrangian (bottom panels, case 2a) density (a), (c) and velocity (b), (d) field contours.
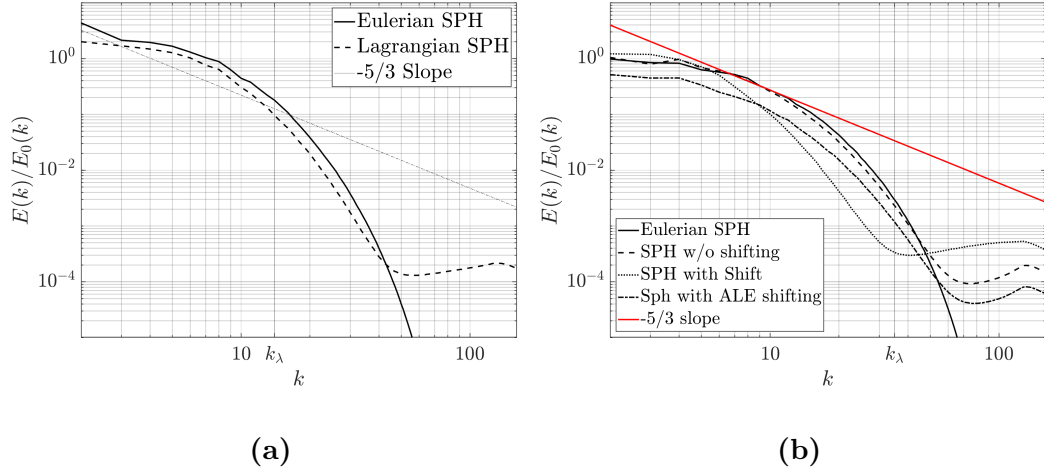
Figure 4.15 Turbulent energy spectra. (a) Cases 1a and 2a. (b) Cases 3a, 4a, 4b, and 4c.

presented, where C is the concentration of SPH particles. These iso-contours show regions in which ∇C reaches high values, suggesting that particles in these regions have a low number of neighbors, which could be detrimental to the consistency and accuracy of the SPH interpolation. To regularize the particle distribution and thus to avoid the creation of "voids", the PST is introduced and the effect of the Arbitrary Lagrangian-Eulerian corrective terms is also assessed.

Figure 4.16(c) shows the effect of employing the PST with the ALE terms (Section 3.6) on the particle concentration: values of ∇C are significantly reduced, though regions with an irregular particle distribution are still observed. If the ALE terms are turned off [Figure 4.16(e)], the particle distribution becomes more uniform throughout the domain. Looking at the iso-countours of the velocity [Figures 4.16(b), 4.16(d), 4.16(f)], the regularization of the particle distribution without the ALE correction comes with the drawback of damping the mid-range scales of motion, resulting in an inaccurate description of the turbulent inertial range. This is also visible in Figure 4.15(b), where the turbulent energy spectra for this set of simulations are shown. The solution obtained with the ALE correction [Figure 4.16(d)] is in good agreement with the simulation obtained without PST [Figure 4.16(b)], indicating
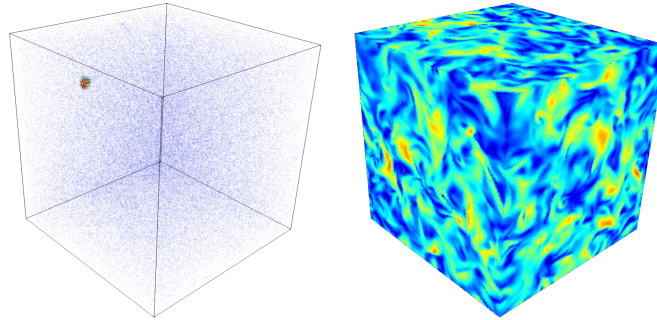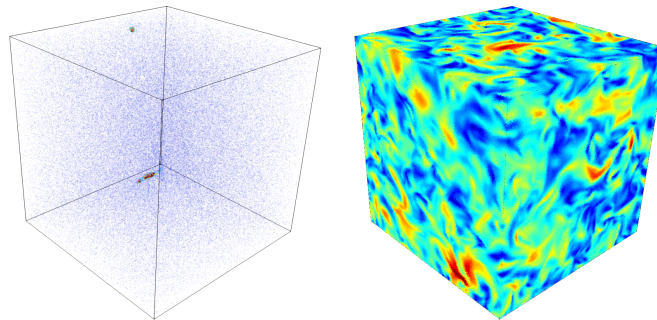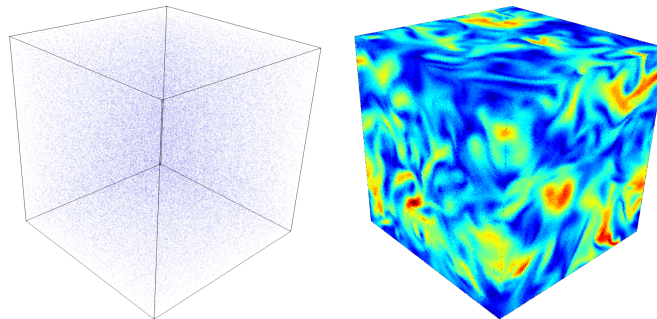
Figure 4.16 Contours of ∇C (left) and velocity (right) at $t = 11$ for the forced isotropic turbulent cases with $A = 0.3$. (a), (b) Lagrangian SPH; (c), (d) Lagrangian SPH with PST and ALE terms; (e), (f) Lagrangian SPH with PST and without ALE terms.

that the corrective terms in the continuity and momentum equations are essential for capturing turbulent flow features well when using the particle shifting technique. Moreover, aside from a spurious flattening at the high wavenumbers as also seen with the case $A = 0.1$, Lagrangian SPH is in good agreement with Eulerian SPH when considering the turbulent energy spectra [Figure 4.15(b)]. When compared to the $A = 0.1$ case, the $A = 0.3$ case shows an extended inertial range that follows the -5/3 Kolmogorov law more closely.

4.5 Decaying Isotropic Turbulence with High-Order SPH Schemes

Once again, the three-dimensional Taylor-Green Vortex, is herein used to assess the performance of SPH schemes based on high-order smoothing kernels.

In Figures (4.17(a))-(4.17(c)), the history of the kinetic energy for the 2nd, 4th, and 6th order schemes is presented with 64^3, 128^3, and 256^3 particles uniformly distributed over a Cartesian grid. With the 2nd order scheme, the coarsest resolution is unable to describe the evolution of the kinetic energy accurately because of the early transition from laminar to turbulent flow that translates into a sudden over-dissipation, also visible by looking at Figure 4.18(b), where the dissipation rate is shown. Increasing the resolution leads to an improvement of the results, although the peak for ϵ is under-predicted even at the highest resolution. When switching to a 4th-order interpolation, it can be seen that the overall accuracy improves. Although the coarsest resolution is still far from the reference solution in terms of the time evolution of the kinetic energy, with an over-prediction of the peak value of the dissipation rate, a correct shape for the time evolution of ϵ is recovered with respect to the 2nd order solution [Figure 4.18(d)]. Further increasing the resolution leads to improvements in the accuracy of the simulation. Specifically, the peak value for the dissipation rate is predicted exactly when using 256^3 particles, with some minor discrepancies seen only for $t > 10$.

When compared to the 4th order, the 6th order scheme with $N = 64^3$ particles is over-dissipative, but this is due to the larger size of the kernel support domain, which results in the inclusion of more noise in the discrete interpolation, especially when the characteristic size of the vortex decreases. However, increasing the resolution leads to results that are comparable to the 4th-order scheme in terms of accuracy. When considering the time evolution of the enstrophy, it can be seen that only the 4th and the 6th order SPH scheme are able to match the reference solution [Figure 4.18(a)-4.18(e)]. Interestingly, the 6th order scheme performs better than the 4th order in the computation of the vorticity, indicating that this particular flow characteristic is better described by increasing the order of accuracy. Another aspect to be considered from Figures 4.18(a)-4.18(e) is the difference between the time history of the dissipation rate ϵ of the kinetic energy and the enstrophy $\mathcal{E}$, which for an incompressible flow are closely related. Disregarding any compressibility effects due to their absence in such simulations, our possible explanation of these discrepancies is the numerical diffusion introduced by the SPH interpolation.

The higher accuracy of high-order schemes with respect to the 2nd-order scheme is also visible in Figure 4.19(a)-4.19(d), where the vorticity contours are compared to the reference solution in a subset of a slice at $x = -0.5$ with $N = 256^3$ particles. Moreover, for the sake of completeness, the turbulent energy spectra for the simulations with $N = 256^3$ particles are also reported in Figure 4.20. The better performance of the 4th and 6th order schemes is confirmed here, too, with a satisfactory degree of accuracy achieved when comparing against the reference data.
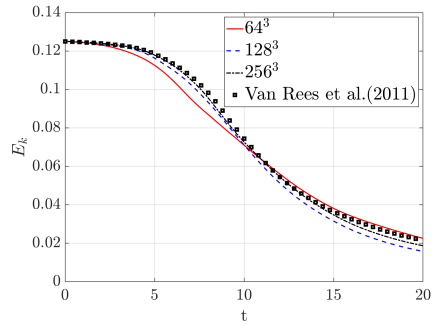
(a)
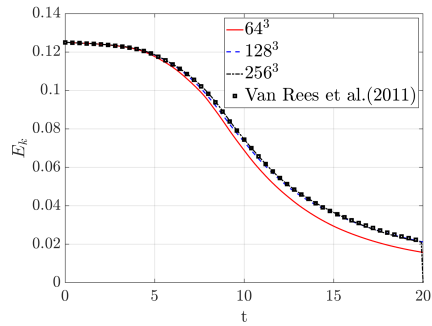
(b)
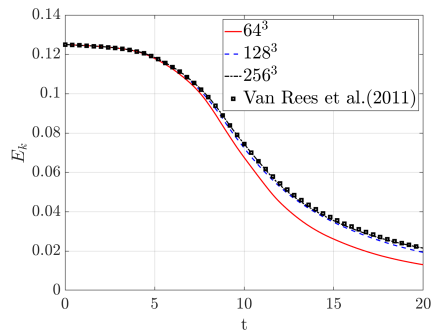
(c)

Figure 4.17 History of the kinetic energy for the (a) 2nd, (b) 4th and (c) 6th order schemes for the Taylor-Green Vortex at Re=1,600. Numerical results are compared to the reference solution in [253].
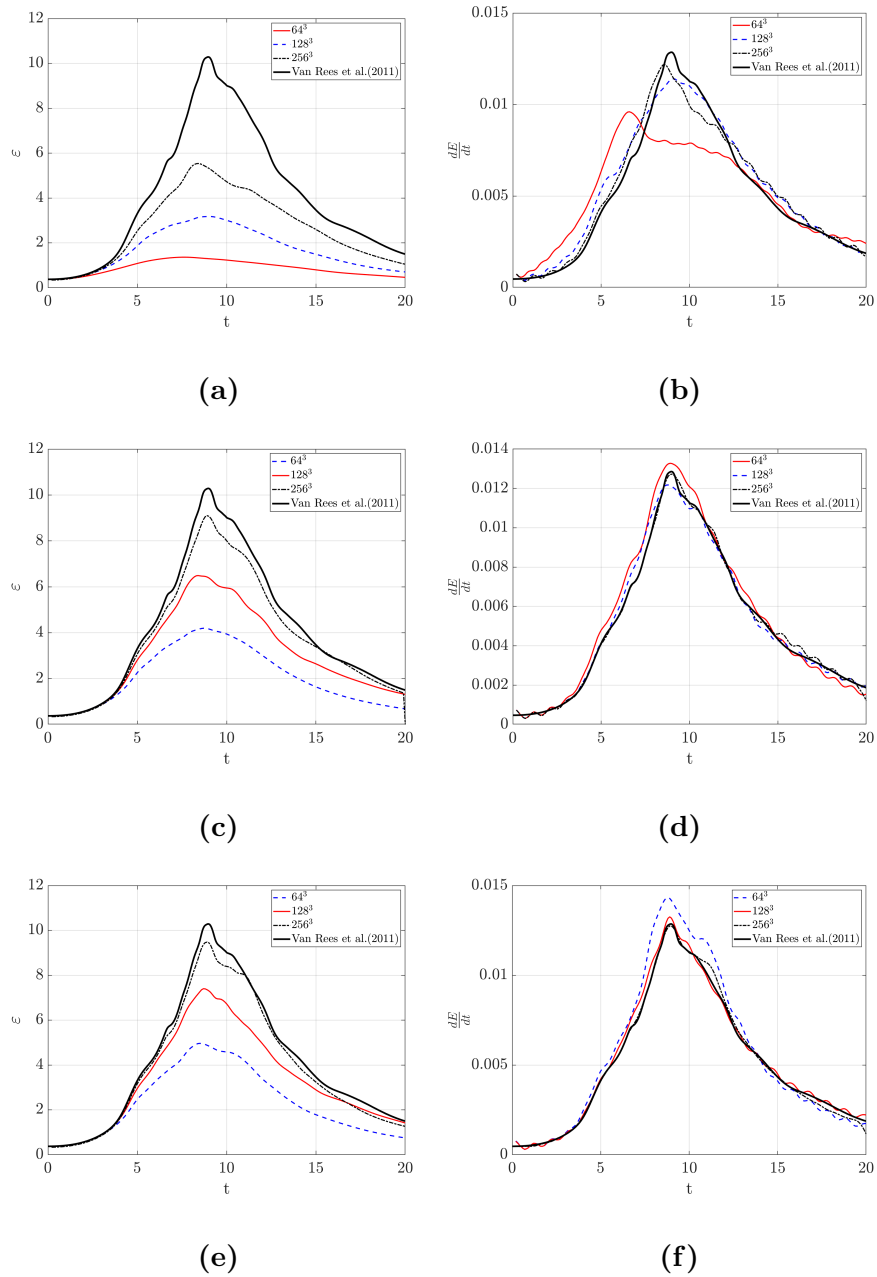
Figure 4.18 Time evolution of the enstrophy and kinetic energy dissipation rate for the (a)-(b) 2nd, (c)-(d) 4th and (e)-(f) 6th order schemes for the Taylor-Green Vortex at Re=1,600. Numerical results are compared to the reference solution in [253].
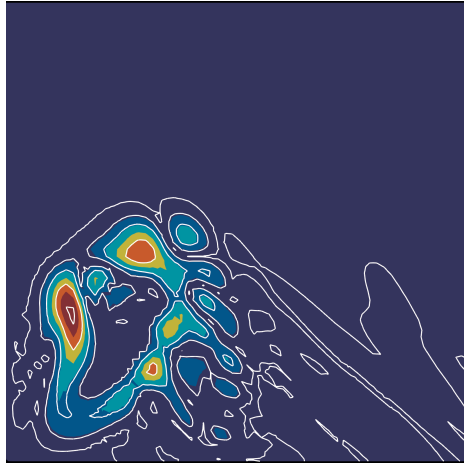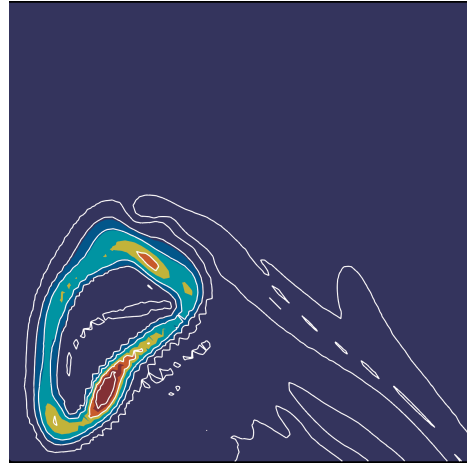
(a)   (b)
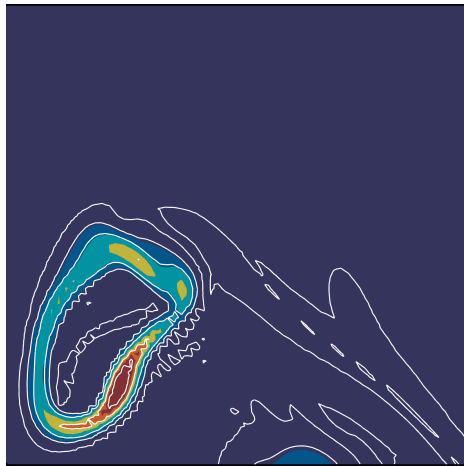
(c)   (d)

Figure 4.19 Vorticity contours for $\boldsymbol{\omega} = 1, 5, 10, 20, 30$ at $x = -0.5$ for the (a) 2nd, (b) 4th and (c) 6th order schemes for the Taylor-Green Vortex at Re=1,600. (d) Reference solution in [253] .
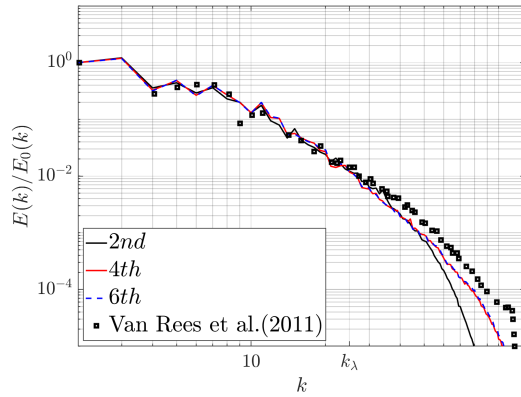
Figure 4.20 Turbulent energy spectrum 2nd, 4th and) 6th order schemes for the Taylor-Green Vortex at Re=1,600 with $N = 256^3$ particles. Numerical results are compared to the reference solution in [253].

CHAPTER 5

MULTI-RESOLUTION ALGORITHM

In the present chapter, an adaptive resolution algorithm for SPH is presented. The scheme presented herein is based on the decomposition of the computational domain into different sub-domains, each with its own characteristic particle size and smoothing length. At each time step, the computational problem is solved in every sub-domain independently, and the sub-domain closure is provided by a buffer region that acts as a Dirichlet boundary condition. Coupling between the different sub-domains is obtained by interpolating the physical quantities in the buffer region using information available at the fluid particles lying in adjacent domains.

5.1 Multi-Resolution Algorithm

The main idea behind the variable resolution algorithm of this study is based on a decomposition of the computational domain, Γ, into a set of N sub-domains, Γ_i with $i = 1, \ldots, N$, such that $\Gamma = \bigcup_{i=1}^{N} \Gamma_i$ [Figure 5.1(a)]. Each sub-domain is characterized by its own characteristic particle size, dp_i, and smoothing length, h_i. To solve the computational problem from t^n to t^{n+1}, a closure Dirichlet boundary condition must be provided at the boundaries of each sub-domain. To this end, each sub-domain Γ_i is extended by appending a buffer region, $\partial \Gamma_i$, with width $l_{\partial \Gamma_i} = 2h_i$ and such that $\partial \Gamma_i \in \Gamma_j$ and $\partial \Gamma_j \in \Gamma_i$. The latter condition allows establishing a bijective topological connection between two sub-domains, formalized with the notation $\partial \Gamma_i^j$, i.e., the buffer region of sub-domain i is coupled with the sub-domain j.

Every buffer region is populated by special SPH particles following a strategy similar to the one adopted in [238] for open boundary conditions. The "buffer" particles are distinct from regular fluid particles as they are not updated using the governing equations of motion. Instead, at the beginning of each time step, a buffer
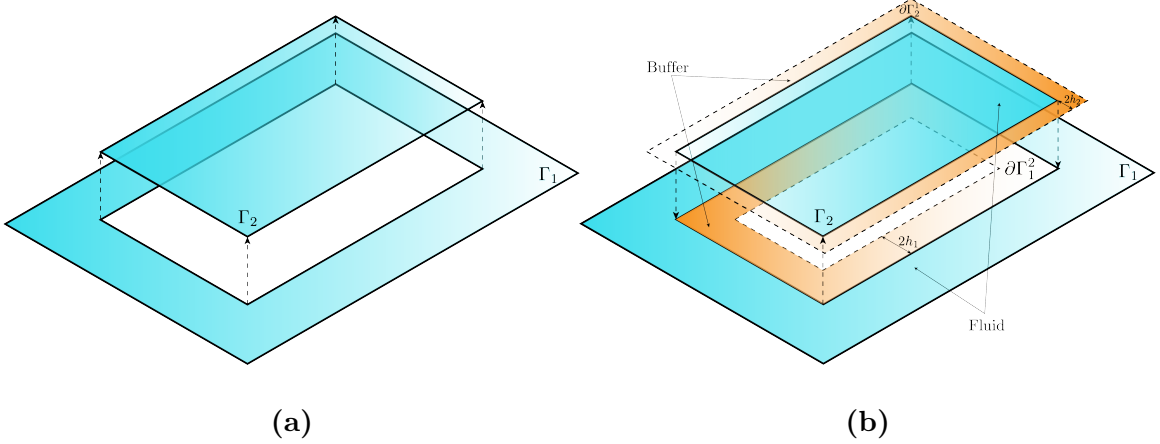
Figure 5.1 (a) Example of two sub-domains Γ_1 and Γ_2. (b) Buffer regions $\partial\Gamma_1^2$ and $\partial\Gamma_2^1$ with widths $l_{\partial\Gamma_1^2} = 2h_1$ and $l_{\partial\Gamma_2^1} = 2h_2$ are appended to their respective sub-domains.

particle $a \in \partial\Gamma_i^j$ obtains its physical properties from a spatial interpolation over fluid particles in Γ_j, as shown in Figure 5.2. Buffer particles located close to the interface have a truncated support, therefore the corrected SPH interpolation proposed in [139] is employed to ensure consistency.

The procedure for restoring particle consistency proposed in [139] starts from a multi-dimensional Taylor series expansion of a field function $f(\mathbf{x})$ multiplied by the kernel function and its derivative up to the desired order of consistency. In this work, a second-order consistency condition is enforced, which in two dimensions results in
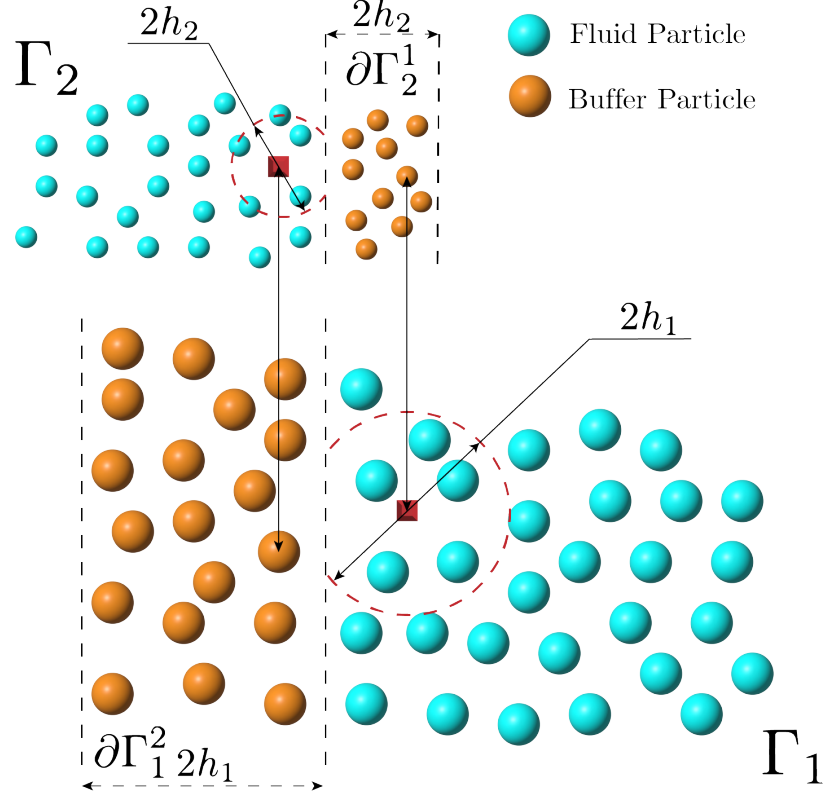
Figure 5.2 Coupling procedure between sub-domains Γ_1 and Γ_2. Buffer particles (orange) interpolate their properties over the fluid particles (light blue) in the coupled subdomain.

the following linear system for the generic buffer particle $a \in \partial\Gamma_i^j$:

$$\mathbf{A}\mathbf{f} = \mathbf{b} \tag{5.1}$$

$$b_m = \sum_{b \in \Gamma_j} f_b w_m V_b \tag{5.2}$$

$$A_{mn} = \sum_{b \in \Gamma_j} w_m r_n V_b \tag{5.3}$$

$$w = \begin{bmatrix} W_{ab} & W_{ab}^x & W_{ab}^y & W_{ab}^{xx} & W_{ab}^{xy} & W_{ab}^{yy} \end{bmatrix} \tag{5.4}$$

$$r = \begin{bmatrix} 1 & x_{ab} & z_{ab} & \frac{x_{ab}^2}{2} & x_{ab}y_{ab} & \frac{y_{ab}^2}{2} \end{bmatrix} \tag{5.5}$$

$$\mathbf{f} = \begin{bmatrix} f_a & f_a^x & f_a^y & f_a^{xx} & f_a^{xy} & f_a^{yy} \end{bmatrix} \tag{5.6}$$

where W is the kernel smoothing function, $\mathbf{x}_{ab} = [(x_a - x_b), (y_a - y_b)]$ is the inter-particle distance, and V is the volume. Once the properties are obtained through the
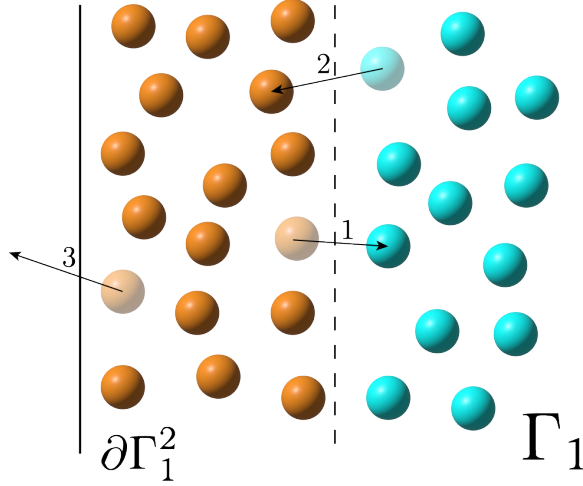
Figure 5.3 A buffer particle that moves into the fluid domain is transformed into a fluid particle (process 1). A fluid particle that enters the buffer region is transformed into a buffer particle (process 2). A buffer particle that moves outside the extended subdomain $\partial\Gamma_i^j \cup \Gamma_i$ is deleted (process 3).

interpolation procedure, the position of the buffer particle a is updated in time using a simple Euler time integration scheme:

$$\mathbf{x}_a^{n+1} = \Delta t \mathbf{v^n}_a. \tag{5.7}$$

where $\mathbf{x}_a^{n+1}$ is the position of the particles at time-step t^{n+1}, and $\mathbf{v^n}_a$ is the velocity at t^n.

To handle the exchange of mass among the different sub-domains, the following conditions are checked at the beginning of each time step:

1. If a buffer particle moves into the fluid domain, it is converted to a fluid particle (Figure 5.3, process 1).

2. If a fluid particle enters the buffer region, it becomes a buffer particle (Figure 5.3, process 2).

3. If a buffer particle moves outside the extended subdomain $\partial\Gamma_i^j \cup \Gamma_i$, this particle is deleted (Figure 5.3, process 3).

Figure 5.4 depicts the procedure of particle insertion into a given sub-domain. The external boundary of the generic sub-domain Γ_i is divided into mass segments of length dp_i and the Eulerian mass flux across the segments is calculated at each time step using the mid-point rule:

$$\dot{m}_a = \max(0, -\rho_{m_a}(v_{m_a} - v_{b_f}) \cdot \mathbf{n} \, dp_i \, dt) \tag{5.8}$$

where $\dot{m}_a$ is the mass flux during the time step dt, ρ_{m_a} and v_{m_a} are the density and the velocity calculated at the mass accumulation point using the same corrected interpolation employed for buffer particles, and v_{b_f} is the velocity of the interface in case of a moving subdomain. After $\dot{m}_a$ is added to m_a, if $m_a \geq (dp)^D / \rho_0$, where D is the number of problem dimensions, a particle is inserted in the buffer region at a distance $dp/2$ in the normal direction to the interface, as shown in Figure 5.4. In presence of free-surface, this procedure has to be adjusted to prevent a non-zero mass flux at the accumulation point above the water level. The following formulation based on the free-surface detection method proposed in [125] is employed for the computation of the mass-flux at the interface:

$$\dot{m}_a = \begin{cases} \max(0, -\rho_{m_a}(v_{m_a} - v_{b_f}) \cdot \mathbf{n} \, dp_i \, dt) & \text{if } \nabla \cdot \mathbf{r} \geq \nabla \cdot \mathbf{r}_{th} \\ 0 & \text{if } \nabla \cdot \mathbf{r} < \nabla \cdot \mathbf{r}_{th}; \end{cases} \tag{5.9}$$

where $\nabla \cdot \mathbf{r} = \sum_b \frac{m_b}{\rho_b} \cdot \nabla W_{ab}$ and $\nabla \cdot \mathbf{r}_{th}$ is a threshold value equal to 1.5 in 2-D and 2.75 in 3-D.

Therefore, because buffer particles move with a Lagrangian velocity which is not obtained from the governing equations directly but from an interpolation over fluid particles in adjacent sub-domains, they do not benefit from the regularization effect of the pressure gradient discretization [198]. These issues can yield an irregular particle distribution in the buffer regions, which eventually affects the correct enforcement of boundary conditions for the sub-domains. A solution to this problem is found
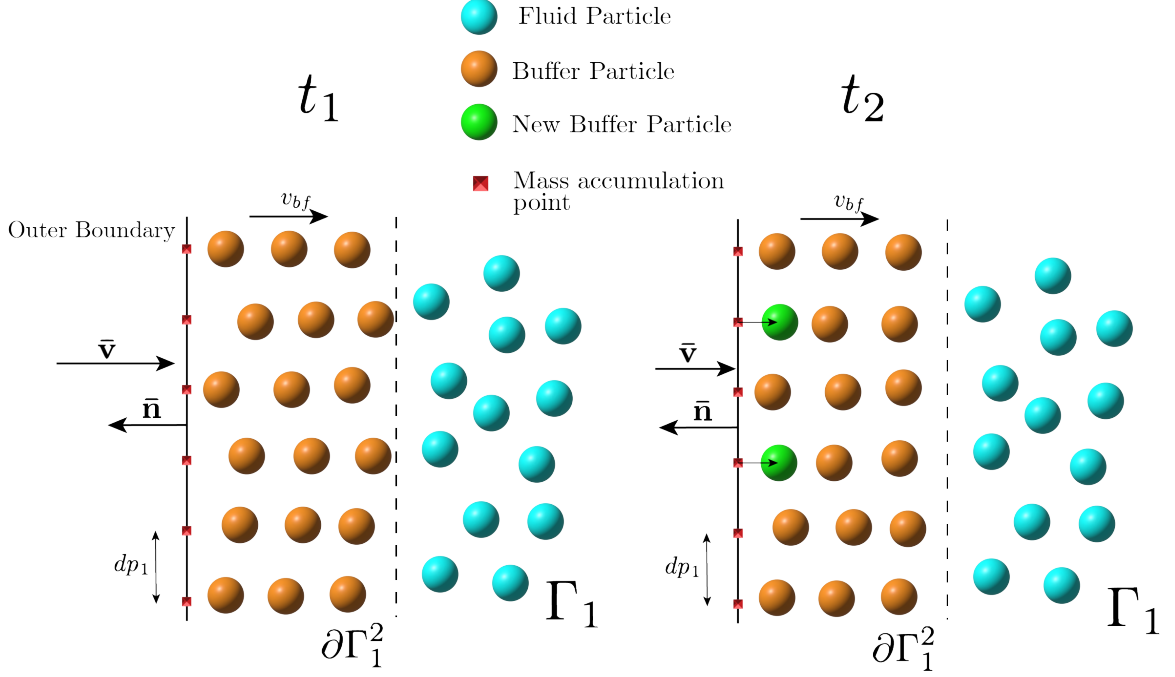
Figure 5.4 Particle insertion procedure: at each time step, the normal mass flux at the outer boundary of the sub-domain is calculated and added to the mass accumulation points (red squares). When the mass at the accumulation points reaches the reference particle mass, new particles (green) are created.

by using the Particle Shifting Technique (PST) in the buffer regions, with special attention to avoid shifting the buffer particles toward the edges of the sub-domain. The latter risk is mitigated by surrounding the edges of the buffer regions with layers of "fixed particles" which have a fixed position in space and constant density ρ_0. Other than these two physical variables, fixed particles do not have any other physical quantity associated and they interact with buffer particles only with the sole purpose of computing the shifting correction. In contrast to the shifting formulation adopted for fluid particles, buffer particles are shifted only in the direction tangential to the interface between the buffer and the fluid region to avoid inaccuracies when computing the mass flux at the interface. Moreover, because normal vectors are ill-defined in the corner regions, the shifting is disabled in these areas (Figure 5.5).

Algorithm 1 shows a pseudo-code of the proposed multi-resolution strategy including all the salient steps of the simulation.
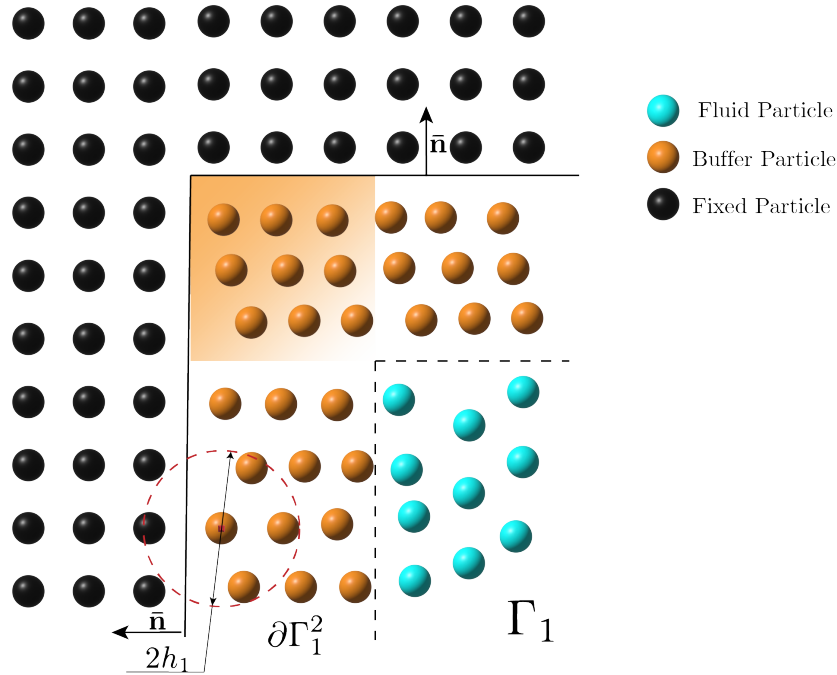
Figure 5.5 Sketch of the regularization procedure for buffer particles. The shifting correction is applied only in the direction tangential to the interface, while neglected in the normal direction **n**. In the corner region, this procedure is deactivated.

5.2 Implementation

5.2.1 The DualSPHysics project

Work herein has been carried out using and modifying the version 5.2 of the DualSPHysics code [62]. DualSPHysics is a weakly-compressible SPH Navier–Stokes solver made of a collection of algorithms written in C++ and CUDA programming languages that is able to exploit the computational acceleration of both CPU (with a shared memory OpenMP approach) and GPU hardware to resolve real-life engineering applications. The project is a collaboration between Universidade de Vigo, the University of Manchester, the University of Lisbon, Università di Parma, Flanders Hydraulics Research, Universitat Politécnica de Catalunya, and the New Jersey Institute of Technology.

The project provides a dedicated set of pre- and post-processing tools (Table 5.1) for the generation and the visualization of test cases in an accessible way while being freely available under GNU Lesser General Public License (LGPL).

Algorithm 1 Main Loop for N sub-domains

1: **begin**

2: **for** $t = 0$ **to** t_{max} **do**

3:     **begin**

4:     **for** $i = 1$ **to** N **do**

5:         **begin**

6:         Calculate fluxes at mass segment;

7:         Insertion and Deletion buffer/fluid particles;

8:         **end**

9:     **for** $i = 1$ **to** N **do**

10:         **begin**

11:         Interpolation buffer particles to obtain ρ and $\mathbf{v}$;

12:         **end**

13:     **for** $i = 1$ **to** N **do**

14:         **begin**

15:         Calculate interaction between particles;

16:         Advance in time ρ and $\mathbf{v}$;

17:         calculate Δt^{n+1} for next step;

18:         **end**

19:     $t = t + t_{global}^{n}$;

20:     $\Delta t_{global}^{n+1} = \min(\Delta t_{i}^{n+1})$;

21:     **end**

22: **end**

Table 5.1 Main Pre- and Post-Processing Tools in the DualSphysics Package

Tool	Description
GenCase	Generate the initial distribution of particles starting from a configuration file.
PartVTK	Read the output binary files and generate paraview format files for visualization of the results.
BoundaryVTK	Read the output binary files and generate paraview format files for visualization of the boundary shape.
MeasureTool	Compute the physical quantities at a set of points defined by the user.
MeasureTool	Compute the force exerted by the fluid onto a boundary object..
FloatingInfo	Obtain different data of the floating objects such as linear velocity, angular velocity, displacement of the center, motions and angles of rotation.
IsoSurface	Create a polygonal mesh for visualization of isosurfaces.
FlowTool	Compute the inflow and the outflow into a specified domain.

5.2.2 DualSPHysics GPU implementation

The DualSPHysics implementation can be divided into three main steps: the creation of the neighbor list (NL), the particle-particle interaction (PI), and the system update (SU):

Neighbor list. In the NL task, the data structures are prepared for an efficient computation of the particle interaction. For the creation of the neighbor list, a cell-linked list approach is used, as discussed in [59]. The computational domain is subdivided into cubic cells with a size equal to the size of the support domain of the kernel smoothing function, usually $2h$. Following the indication in [49],

the arrays that store the physical properties of the particles are reordered in order to ensure coalesced memory access. The last step is paramount to reduce the number of global memory access in the GPU, which can be a significant bottleneck due to the lower bandwidth with respect to the register memory access.

Particle interaction. In the particle interaction, the right-hand side of the governing equations is computed in order to advance the solution. For each particle, a CUDA kernel loops through the neighboring particles in the adjacent cells. To improve the performance of the code and avoid inefficiencies due to code divergence, two different CUDA kernels are used for the fluid-fluid and fluid-solid interaction.

System Update. In the system update, the physical properties of the particles are updated.

In order to avoid the bottleneck due to the limited memory bandwidth between the CPU and GPU memory, all particle data is stored in GPU memory from the beginning to the end of the simulation and these these three steps are all executed in the GPU.

DualSPHysics is written in the C++ programming language and is structured according to the principles of object-oriented programming. The GPU implementation is instantiated in the JSphGpuSingle class derived from the JSphGpu class. The flow of the code is controlled by the JSphGpuSingle::Run() routine, which can be divided into three steps:

1. Configuration: with the creation of initial particle distribution and the allocation of the memory (Table 5.2).

2. Main loop: the solution is advanced in time, following the structure outline previously (Table 5.3).

Table 5.2 Initialization Functions and their Description

Function	Description
SelecDevice	Initialises CUDA device.
LoadConfig	Loads the configuration of the execution.
LoadCaseParticles	Loads particles of the case to be processed.
ConfigConstants	Configures value of constants.
ConfigDomain	Configuration of the current domain.
AllocGpuMemoryFixed	Allocates memory in GPU for arrays with a fixed size.
AllocGpuMemoryParticles	Allocates memory in GPU of main data of particles.
AllocCpuMemoryParticles	Allocates memory in CPU of main data of particles.
ReserveBasicArraysGpu	Arrays for basic particle data in GPU.
ParticlesDataUp	Uploads particle data to the GPU.
ConstantDataUp	Uploads constants to the GPU.
ConfigBlockSizes	Calculates optimum blocksize.
RunCellDivide	Generates neighbour list.
ConfigRunMode	Configures execution mode in GPU.
InitRun	Initialisation of arrays and variables for the execution.
SaveData	Generates file with particle data of the initial instant.

3. Conclusion of the simulation and data saving.

5.2.3 Implementation of the variable-resolution algorithm

The DualSPHysics code is able to tackle a broad range of applications, with different formulations available and coupling with third-party multiphysics libraries. This is reflected in the complexity and size of the source code. Moreover, thanks to the work
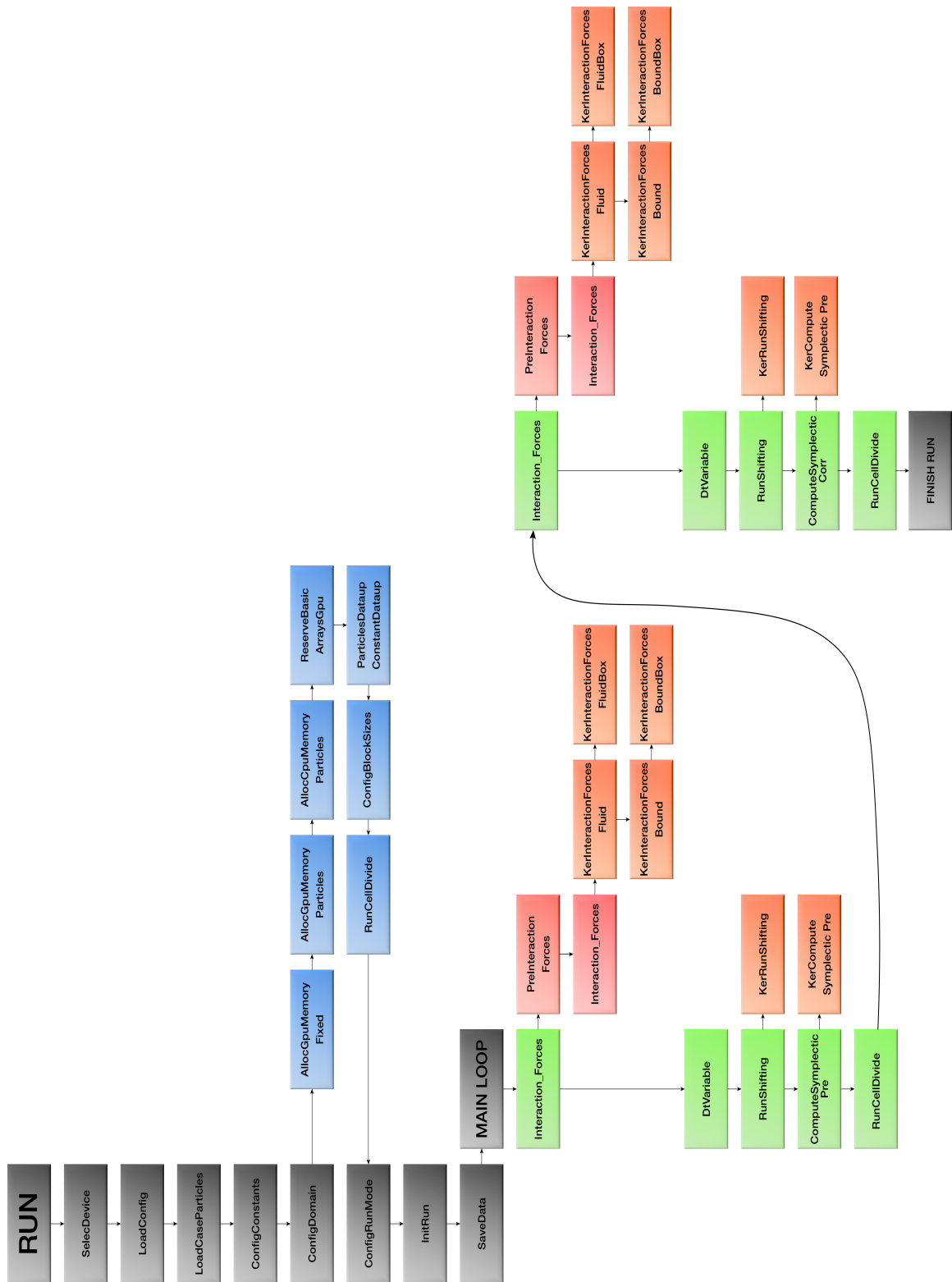
Figure 5.6 Call function for the DualSPHysics GPU code using a symplectic integrator

Table 5.3 Main Loop Functions and their Description

Function	Description
Predictor step.	
Interaction Forces	Call for particle interaction (PI).
PreInteraction Forces	Prepares variables and assigns memory for PI.
Interaction	Forces Computes particle interaction.
DtVariable	Computes the value of the new variable time step.
ComputeSymplecticPre	Computes System Update using
PosInteraction	Forces Memory release of arrays in GPU.
RunCellDivide	Generates neighbour list.
CORRECTOR Corrector step.	
Interaction Forces	Call for particle interaction.
PreInteraction Forces	Prepares variables and assigns memory for PI.
Interaction Forces	Computes particle interaction.
DtVariable	Computes the value of the new variable time step.
ComputeSymplecticCorr	Computes system update using symplectic=corrector.
PosInteraction	Forces Memory release of arrays in GPU.
RunCellDivide	Generates Neighbour List.
FinishRun	Shows and stores final overview of execution.

of different research groups, the DualSPHysics package is constantly updated with new functionalities.

To keep the range of applicability of DualSPHysics intact and possibly to extend it, the variable resolution algorithm was implemented, favoring the preservation of

the base structure of the code, avoiding major changes that could lead to long-term maintenance issues.

There are two observations that can be made by looking at the algorithm proposed in Section 5.1 for variable resolution and to the DualSPHysics code structure outlined previously:

- Each computational sub-problem is dependent on the other ones only when the physical properties of the buffer particles are interpolated

- To each computational sub-problem corresponds a JSphSingle class instance.

Considering these two aspects, the implementation of the new algorithm has been structured by operating at the highest level of abstraction. A new class, named JSphGpuWrapper, has been implemented: in this new object, an array of JSphGpuSingle objects is allocated, and at each object corresponds a numerical sub-domain. In this way, each computational sub-problem can be managed independently and synchronized to the other when needed.

- The number of sub-domains is read from the configuration file

- The JSphGpuSingle array is allocated

- Each JSphGpuSingle is initialized and configurated

- The main loop for advancing the simulation is executed.

- Subroutine for completing the simulation.

The new main loop is structured in the same way as in the standard DualSPHysics implementation. Still, at the end of the time-step, the routines for updating the buffer regions are executed, following the pseudocode outlined in Algorithm 1:

1. For each subdomain, the solution is advanced in time by calling the same subroutines as in the original DualSPHysics code.

Table 5.4 Main loop Functions and their Description

Function	Description
Interaction_BufferExtrapFlux	Call for computing the flux at the accumulation point.
ComputeStep	Procedure for transformation between fluid and buffer particles.
BufferListCreate	Definition of the point in which buffer particles must be created.
BufferCreateNewPart	Creation of buffer particles.
RunCellDivide	Generates neighbour list.
Interaction_BufferExtrapFlux	Call for interpolating the buffer particles.

2. Each sub-domain computes the coupling part of the new multi-resolution algorithm.

A visualization of the structure of the main loop for the multi-resolution implementation is shown in Figure 5.7, while in Table 5.4 are described the functions of the coupling section of the multi-resolution algorithm is divided into these main steps, which can be divided in three main steps:

1. Computation of the flux at the accumulation point.

2. Evaluation of the mass segment and particle creation and deletion procedure.

3. Particle reordering and interpolation for obtaining the physical properties of the buffer particles.

The main advantage of the present implementation strategy is that the main structure of the DualSPHysics code is left unchanged as the changes introduced for the variable
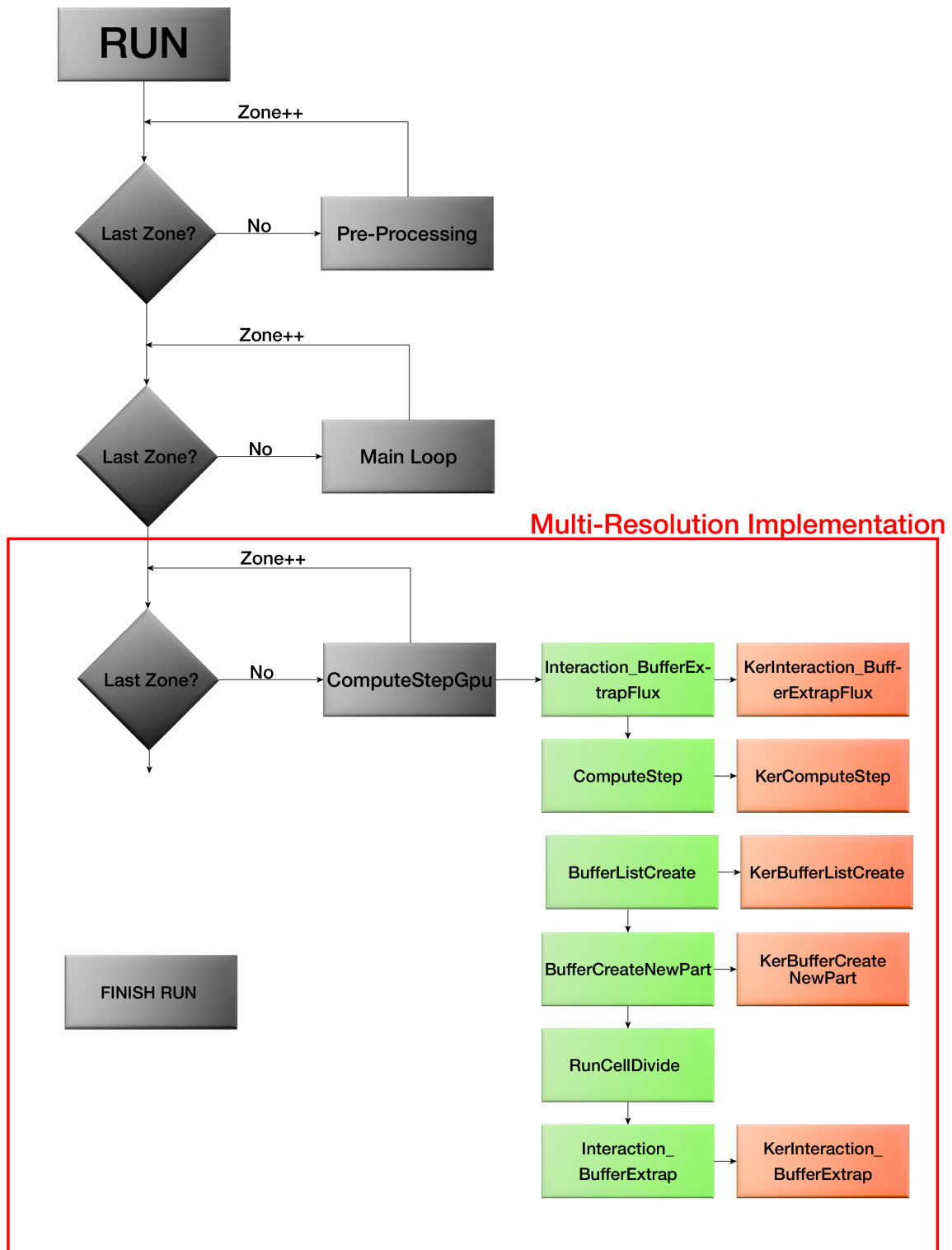
Figure 5.7 Call function for the main loop in the new multi-resolution algorithm.

Table 5.5 New Files Added to the Source Code

Files	Description
JSphGpuWrapper.cpp/.h	Implements the class JSphGpuWrapper.
JSphGpuSingleBuffer.cpp	Define the host function for the coupling algorithm.
JSph_Gpu_Buffer.cu	Define the Cuda kernel function for the coupling algorithm.
JSphBuffer.cpp/.h	Implements the class JSphBuffer.
JSphBufferZone.cpp/.h	Implements the class JSphBufferZone.
Interaction_BufferExtrapFlux	Call for interpolating the buffer particles.

resolution algorithm are additive. In Table 5.5 are listed the new files introduced in the source code. Two new classes are introduced into the code:

JSphBufferZone In this class, the geometrical definition of the buffer region is defined.

JSphBuffer Define an array of JSphBufferZone objects, one for each buffer region of the sub-domain. It also implements the routine needed to retrieve the list of particles in the buffer region and label them as buffer particles.

5.3 Results and Discussion

5.3.1 Hydrostatic tank

Despite being a simple test case, the hydrostatic tank is often very difficult for the SPH method, because of the inconsistency due to the presence of a free-surface and the tank wall that introduce numerical error in the solution. Moreover, is an ideal test case to verify the accuracy of the coupling between sub-domain and any inaccuracies introduced by the interpolation of buffer regions.
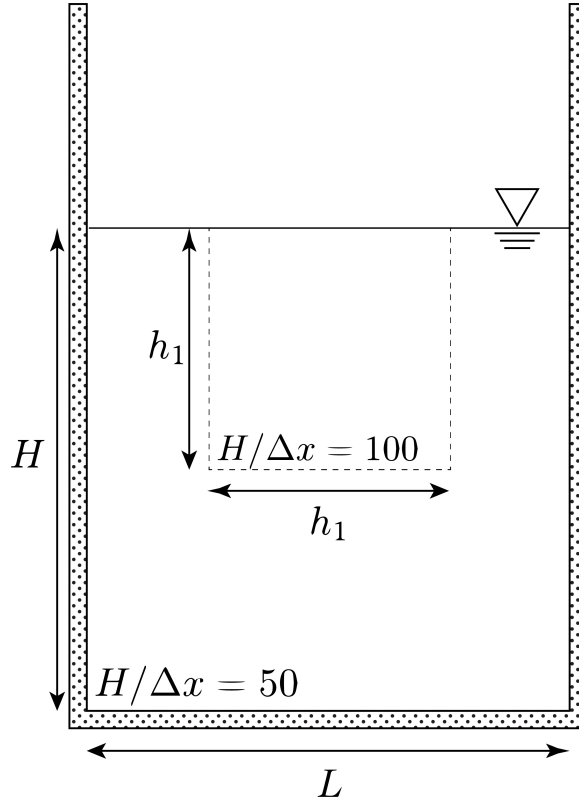
Figure 5.8 Computational domain for the hydrostatic tank case

For these reasons, an hydrostatic tank is chosen as a study case to validate the proposed variable-resolution algorithm. The computational domain consists of a 2-D rectangular tank, with width $L = 1m$, filled with water up to a height $H = 1m$. The water density is set equal to $\rho_0 = \rho_\infty = 1000$ kg/m^3 and the gravity $g = 9.81$m/s^2. Regarding the numerical parameters, an artificial viscosity model is used with $\alpha = 0.01$, while the speed of sound is equal to $c_0 = 10v_{max}$, where $v_{max} = \sqrt{gH}$. The Fourtakas DDT in Equation 3.66 is used to order to preserve the hydrostatic solution.

Two refinement zone are employed, the coarse one with a resolution equal to $H/\Delta x = 50$, and the finest one with $H/\Delta x = 100$. The refinement region is a square box with length $h_1 = 0.5m$, centered at the midline of the rectangular tank. In Figure 5.8 the geometrical definition of the computational domain and of the refinement regions is shown.
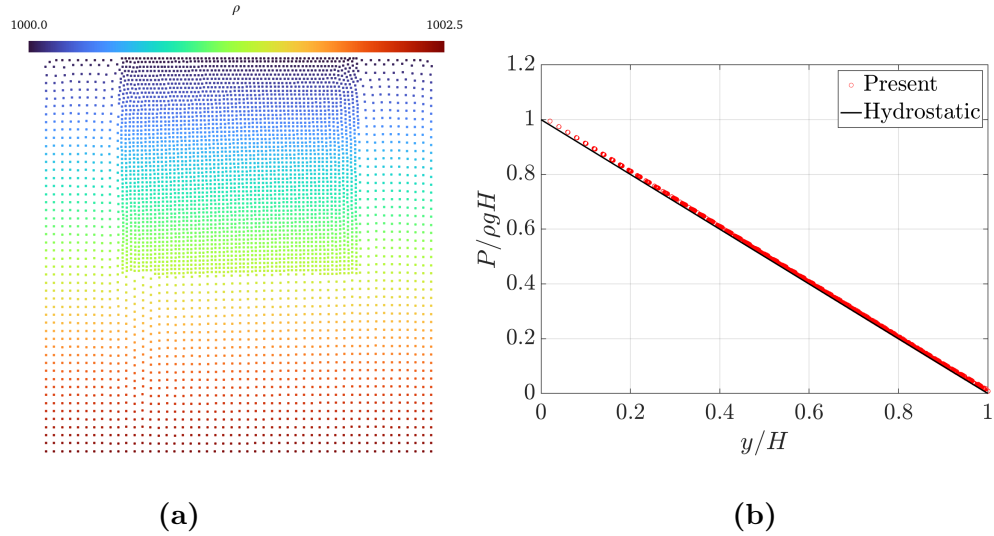
Figure 5.9 Hydrostatic tank case: (a) density contours and (b) pressure distribution against the hydrostatic solution at $t = 20s$

Figure 5.9(b) reports the pressure distribution against the vertical coordinate at $t = 20s$: as can be seen, the present multi-resolution approach is able to preserve the hydrostatic solution, and no discontinuities are visible at $y/H = 0.5$, where the horizontal interface between the coarse and the fine resolution is placed. Moreover, despite a low value of the artificial viscosity coefficient α, in Figure 5.9(a) the density contours at $t = 20s$ reveal a regular distribution of the particles, that doesn't show any spurious motion, especially at the interface between the sub-domains.

5.3.2 Flow past a fixed, circular cylinder

Flow past a circular cylinder is simulated for several Reynolds numbers (Re) as a first study case to benchmark the new multi-resolution algorithm against consolidated literature results. This problem has been investigated extensively both numerically and experimentally, thus it is suitable for demonstrating the advantages of the present multi-resolution approach with respect to using a uniform SPH particle resolution. Since the Reynolds number based on the smoothing length, $Re_h = U_\infty h \nu^{-1}$, must be in the order of 1 to resolve the flow near the cylinder properly, this test case is
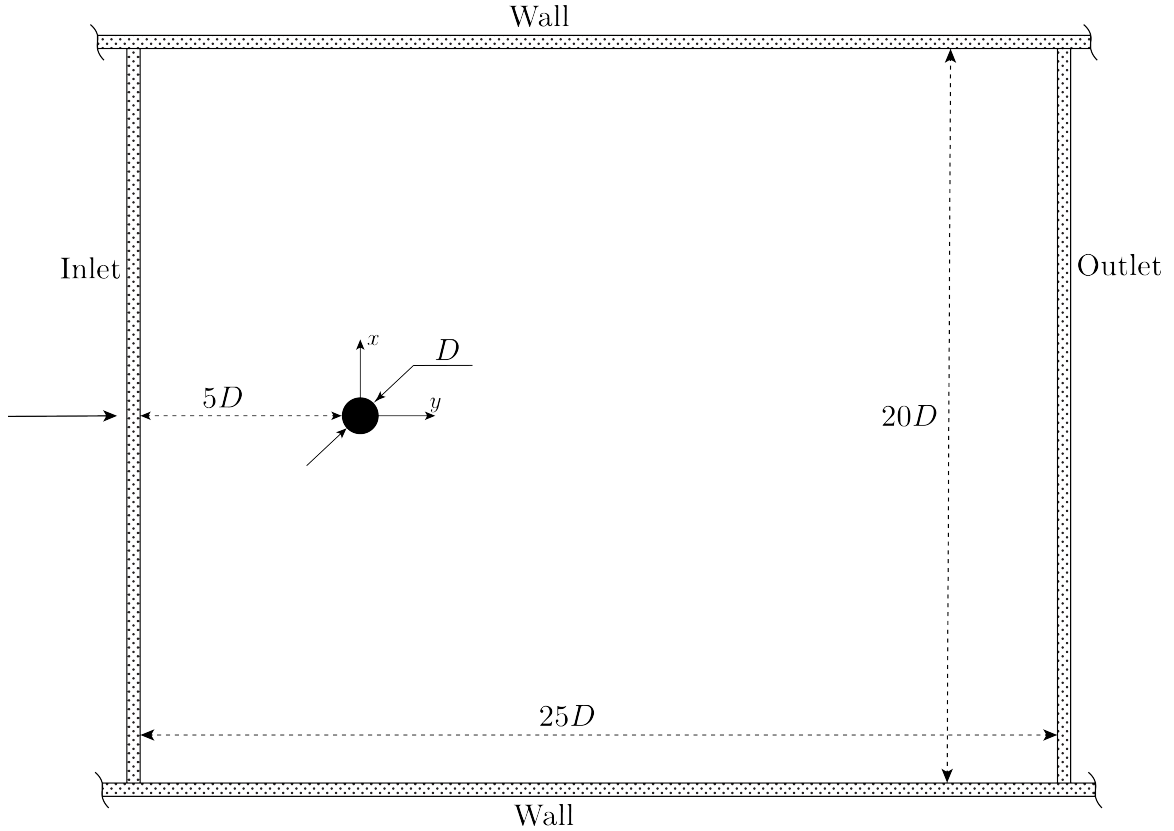
Figure 5.10 Computational domain for 2-D flow past a circular cylinder

quite challenging to resolve with a uniform particle resolution, even at low to moderate Reynolds numbers, due to the prohibitive number of particles required for the domain discretization. Moreover, the level of resolution needed in the far-field is substantially lower than around the cylinder and thus the proposed multi-resolution algorithm is adopted to reduce the average particle resolution in the far-field without affecting the global accuracy of the simulation.

The computational domain shown in Figure 5.10 is chosen following the work in [238], where a cylinder with diameter $D = 0.1$ m is centered at $(x, y) = (0, 0)$ and the overall domain dimensions are set to $25D \times 20D$ to minimize the change of any blockage effect. A no-slip solid boundary condition is applied to the cylinder, while free-slip conditions are defined at the bottom and upper walls. Inflow-outflow conditions are imposed using the formulation in [238]: at the inlet, the velocity and
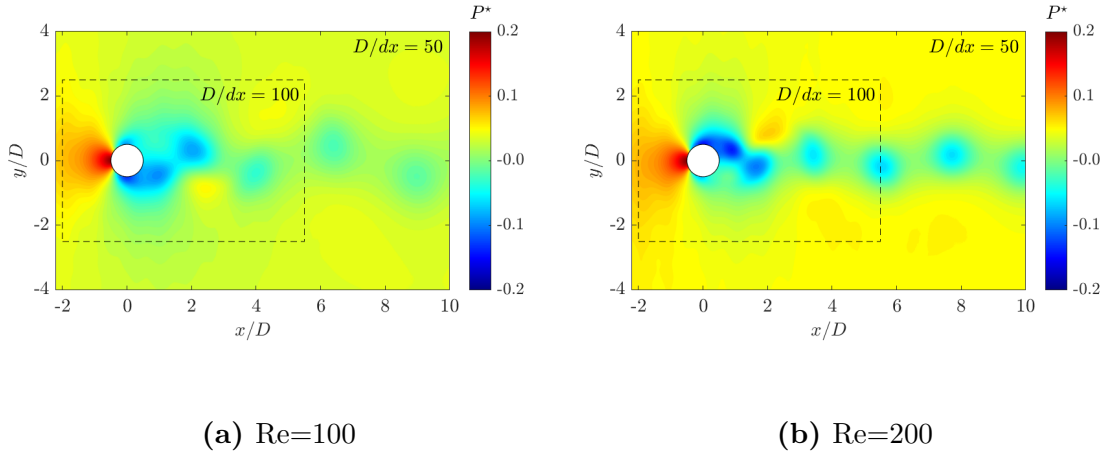
(a) Re=100 **(b)** Re=200

Figure 5.11 Dimensionless pressure for flow past a cylinder with (a) Re = 100 and (b) Re = 200

the density are prescribed, whereas at the outlet, the velocity is extrapolated from the fluid to the buffer region, while the density is prescribed to the reference value. The fluid is initialized with $U_\infty(x, y) = (1, 0)$ m/s while the density has an initial value equal to $\rho_0 = \rho_\infty = 1000$ kg/m^3. The Reynolds number Re$=U_\infty D \nu^{-1}$ is varied by changing the value of the kinematic viscosity ν. The smoothing length is set to $h = 2\Delta x$, constant across the different sub-domains, and the DDT in Equation (3.66) is activated in order to diffuse the oscillations affecting the density field due to the centered collocated SPH scheme. Finally, PST is applied to avoid the creation of empty regions due to the vortical structures that develop in the wake.

For the setup of the different resolution sub-domains, a minimum resolution corresponding to $D/\Delta x = 25$ is chosen for the far field. Then, new sub-domains are nested inside the far-field, each with a resolution that doubles as they get closer to the cylinder. The number of subdomains created depends on the flow Reynolds number, with higher Re requiring higher overall resolution, therefore more sub-domains. Table 5.6 summarizes the number of sub-domains used and their respective dimensions and particle resolutions as a function of the Reynolds number.

Table 5.6 Number of Sub-Domains Used and their Respective Dimensions and
Particle Resolution as a Function of the Reynolds Number

Case	Re	Number of zones	$D/\Delta x_{max}$
1	100	3	100
2	200	3	100
3	1000	4	200
		5	400
		6	800
4	3000	5	400
		6	800
		7	1600
5	9500	6	800
		7	1600
		8	3200

Re = 100 and 200 For the first two Reynolds numbers Re = 100, 200, only
three sub-domains are utilized as shown previously, and these refinement regions
are centered at the cylinder and extended downstream to better resolve the wake
region. The contours of dimensionless pressure $P^\star = P(x/D, y/D)\rho^{-1}U_\infty^2$ shown
in Figure 5.11 depict the vortices' cores, clearly visible as low-pressure regions
developing in the wake. These vortical structures have higher intensity with increasing
Reynolds number. No discontinuities are visible through the interface between
the fine and the medium refinement regions, demonstrating the robustness of the
coupling procedure between sub-domains. Furthermore, the dimensionless vorticity
$\zeta^\star = \zeta(x/D, y/D)DU^{-1}$ can be observed in Figure 5.12, colored such that clockwise
and counter-clockwise fluid rotations tend towards blue and red, respectively. The
typical von Karman street associated with the periodic vortex shedding is captured
correctly and the vortical structures cross the interface of the different resolution
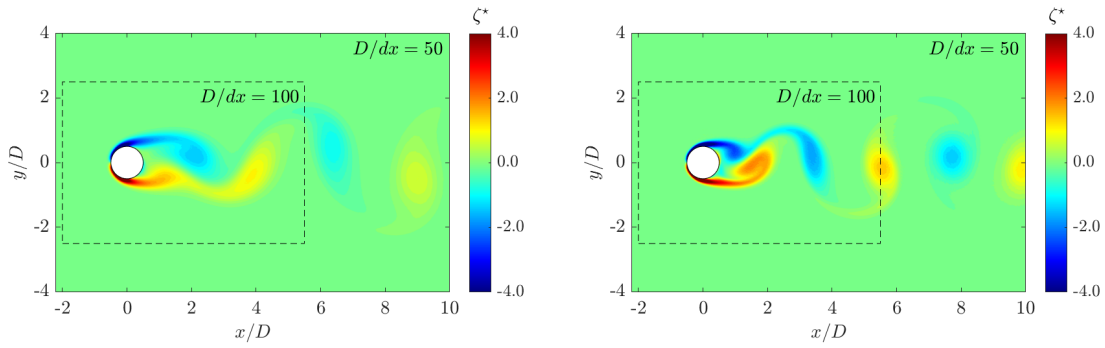
(a) Re=100   **(b)** Re=200

Figure 5.12 Dimensionless vorticity for flow past a cylinder with (a) Re = 100 and (b) Re = 200
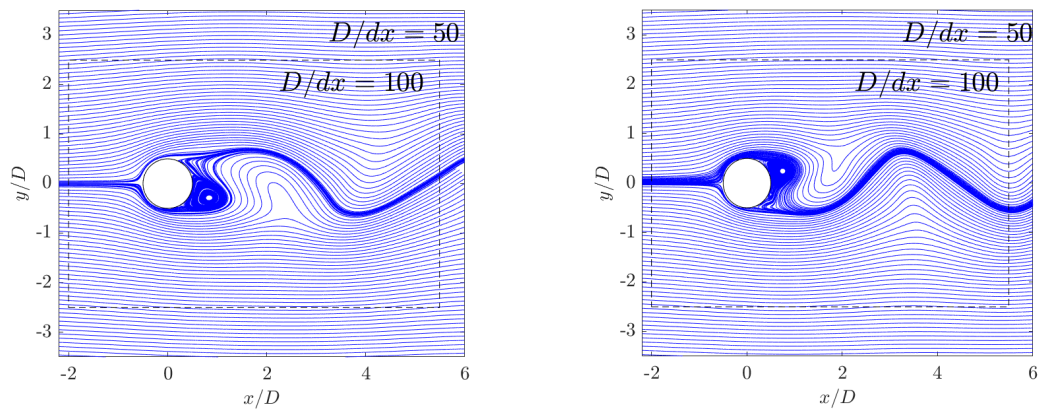
(a) Re=100   **(b)** Re=200

Figure 5.13 Streamlines for flow past a cylinder with (a) Re = 100 and (b) Re=200

sub-domains without any numerical noise or associated errors. The oscillating nature of the flow, with the presence of counter-rotating vortices in the wake of the cylinder, is also visible in Figure 5.13, where the streamlines are presented for both Reynolds numbers.

Table 5.7 Mean Values of Drag Coefficient C_D, Lift Coefficient C_L, and Strouhal Number St for the Re $= 100$ and Re $= 200$ cases

Re		Present	Tafuni et al. [238]	Liu et al. [137]	Marrone et al. [150]
	C_D	1.375		1.35	1.36
100	C_L	0.34	0.322	0.339	0.24
	St	0.175	0.177	0.165	0.168
	C_D	1.316	1.46	1.31	1.38
200	C_L	0.7	0.693	0.690	0.68
	St	0.205	0.206	0.192	0.200

For a quantitative assessment, the drag and lift coefficients, C_D and C_L respectively, and the Strouhal number, St, have been computed as follows:

$$C_D = 2F_D\rho_\infty^{-1}U_\infty^{-2}D^{-1},$$
$$C_L = 2F_L\rho_\infty^{-1}U_\infty^{-2}D^{-1}, \tag{5.10}$$
$$St = fDU_\infty^{-1}$$

where F_D and F_L are the drag and lift forces over the cylinder, respectively, and f is the vortex shedding frequency computed through spectral analysis. The mean values of drag and lift coefficients and the Strouhal number are reported in Table 5.3.2 and compared to other relevant SPH studies, with a close agreement observed throughout. Moreover, Figure 5.14 includes the time history of C_L and C_D, highlighting the relation between the aerodynamic forces and the Reynolds number. As the latter increases, there is a corresponding rise in the maximum lift coefficient and Strouhal number, while a decrease in the drag coefficient is observed.

To ensure that the proposed variable resolution algorithm preserves the accuracy of the solution, the same test cases above have been solved using a uniform resolution equal to $D/\Delta x = 100$, i.e., the highest resolution used with variable resolution in the sub-domain closest to the cylinder. Figure 5.15 shows the time history of the
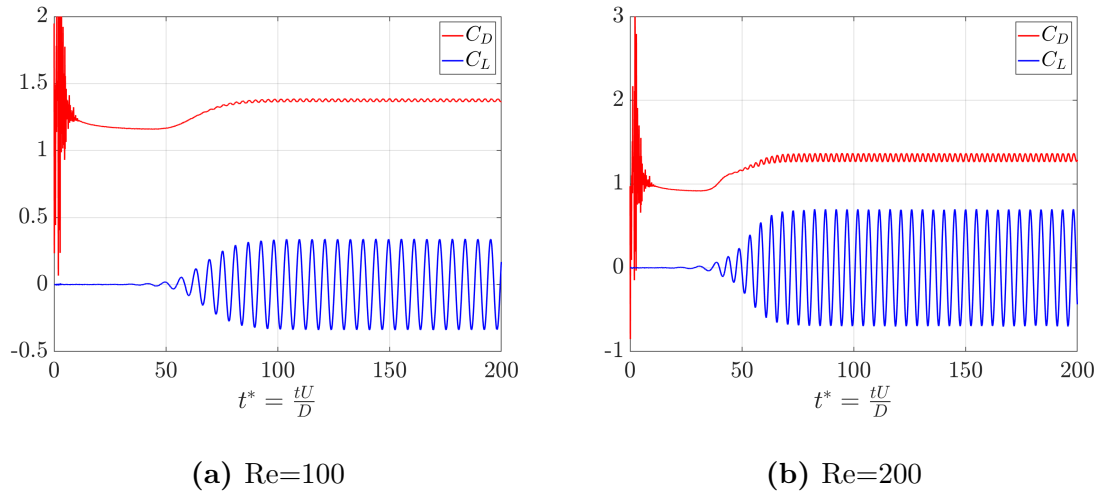
(a) Re=100

(b) Re=200

Figure 5.14 Time history of the drag and lift coefficient for a flow past cylinder with Re = 100 and Re = 200
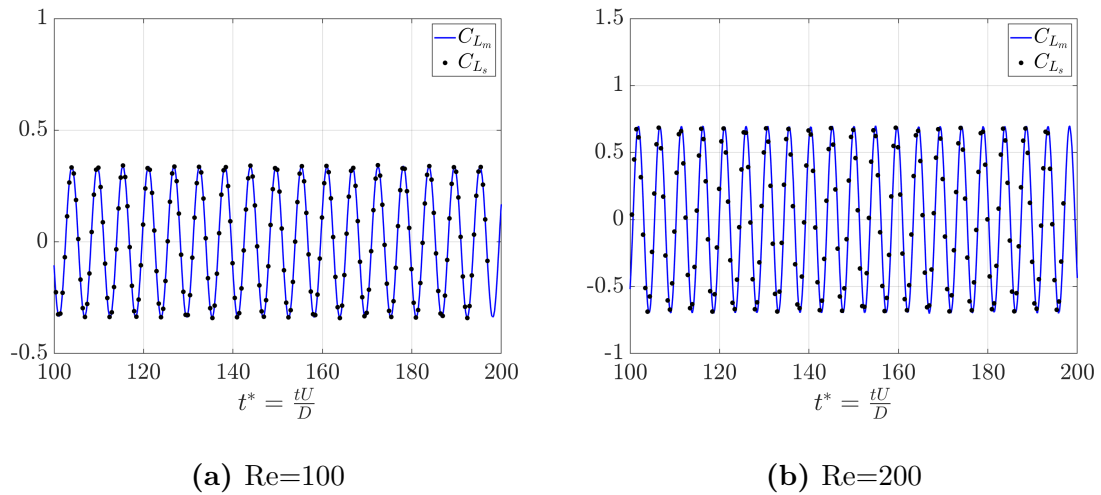
(a) Re=100

(b) Re=200

Figure 5.15 Time history of the lift coefficient for flow past a cylinder with (a) Re = 100 and (b) Re = 200. C_{Ls} indicates the lift coefficient obtained from a single resolution simulation while C_{Lm} belongs to the multi-resolution simulation.

lift coefficient obtained using a single resolution, C_{Ls}, and the one calculated for the multi-resolution simulation, C_{Lm}. The two signals are in very good agreement with each other, showing how the multi-resolution is preserving the solution accuracy while requesting a total number of particles less than one order of magnitude with respect to the uniform resolution simulation.

Re = 1000, Re = 3000 and Re = 9500   As the Reynolds number increases to values 1000, 3000, and 9500, the vortex dynamics in the wake of the cylinder becomes three-dimensional [267], although the flow can still be considered mostly two-dimensional in the early stages [27]. The simulation setup chosen for these high Reynolds numbers is similar to the Re = 100, 200 cases, albeit with some adjustments. First of all, the initialization of the velocity and density fields is done with potential flow solutions, in order to expedite the simulation runtime. Moreover, to ensure convergence in these higher Reynolds number cases, different levels of refinement are considered for each Reynolds number and the results are validated against reference solutions. For example, for Re = 1000, three simulations have been run respectively with 4, 5, and 6 SPH sub-domains, each with its own particle resolution. Each time a new sub-domain is added in a simulation, it is nested in the previous, finest resolution sub-domain, following a Russian doll-like approach. The resolution in a newly created sub-domain is always double that of the sub-domain in which it is nested. Considering again Re = 1000 as an example, this means that the highest resolution achieved in the three cases with 4, 5 and 6 sub-domains is $D/\Delta x = 200, 400, 800$, respectively. The illustration in Figure 5.16 shows how this domain partitioning strategy leads to having a remarkable number of 9 SPH sub-domains for the highest Reynolds number case, i.e. Re = 9500, with a maximum resolution of $D/\Delta x = 3200$ achieved near the cylinder.

Figure 5.17 shows the time histories of drag coefficient for the three Reynolds numbers herein, each with three SPH multi-resolution simulations validated against the reference solutions in [118]. Specifically, Figure 5.17(a) focuses on Re = 1000, where it is noticeable how the drag force starts to increase from $t^* = 0.5$ due to the appearance of primary vortical structures. These are clearly visible in the vorticity contours depicted in Figure 5.18(a) and in the streamlines of Figure 5.19(a). At around $t^* = 3$ [Figure 5.18(c) and 5.19(c)], a secondary pair of vortical structures
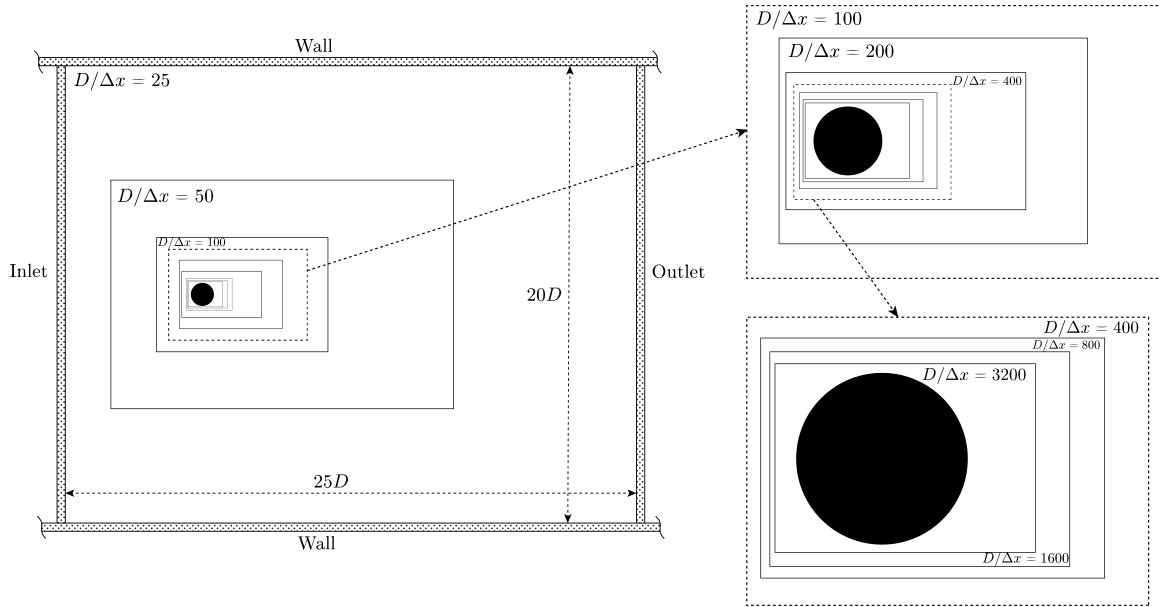
Figure 5.16 Sketch of the different SPH sub-domains created to resolve the flow past a cylinder at various Reynolds numbers

develops, which hampers the growth of the drag coefficient. However, these vortices are not able to reach further in the wake and therefore, they remain confined by the primary vortices.

When Re = 3000 is considered, the number of sub-domains adopted increases to 5, 6 and 7, corresponding to maximum resolutions of $D/\Delta x = 400, 800, 1600$ achieved in the vicinity of the cylinder. Looking at the drag coefficient in Figure 5.17(b), a convergence of the solution is achieved also for this case, with a very good agreement between the SPH solution with $D/\Delta x = 1600$ and the reference solution in [118]. As for Re = 1000, the drag force over the cylinder starts to increase due to the formation of vortices in the wake region[Figure 5.20(a) and 5.21(a)] until $t^* = 2$, when a secondary vortex pair appears [Figure 5.20(b) and 5.21(b)], which causes a flattening of the drag curve at around $t^* = 2.5$ as noted in Figure 5.17(b). However, in constrast to the Re = 1000 case, a tertiary vortex pair is generated here, establishing a feeding mechanism for the primary vortex and therefore causing an increase in drag

(a) Re = 1000
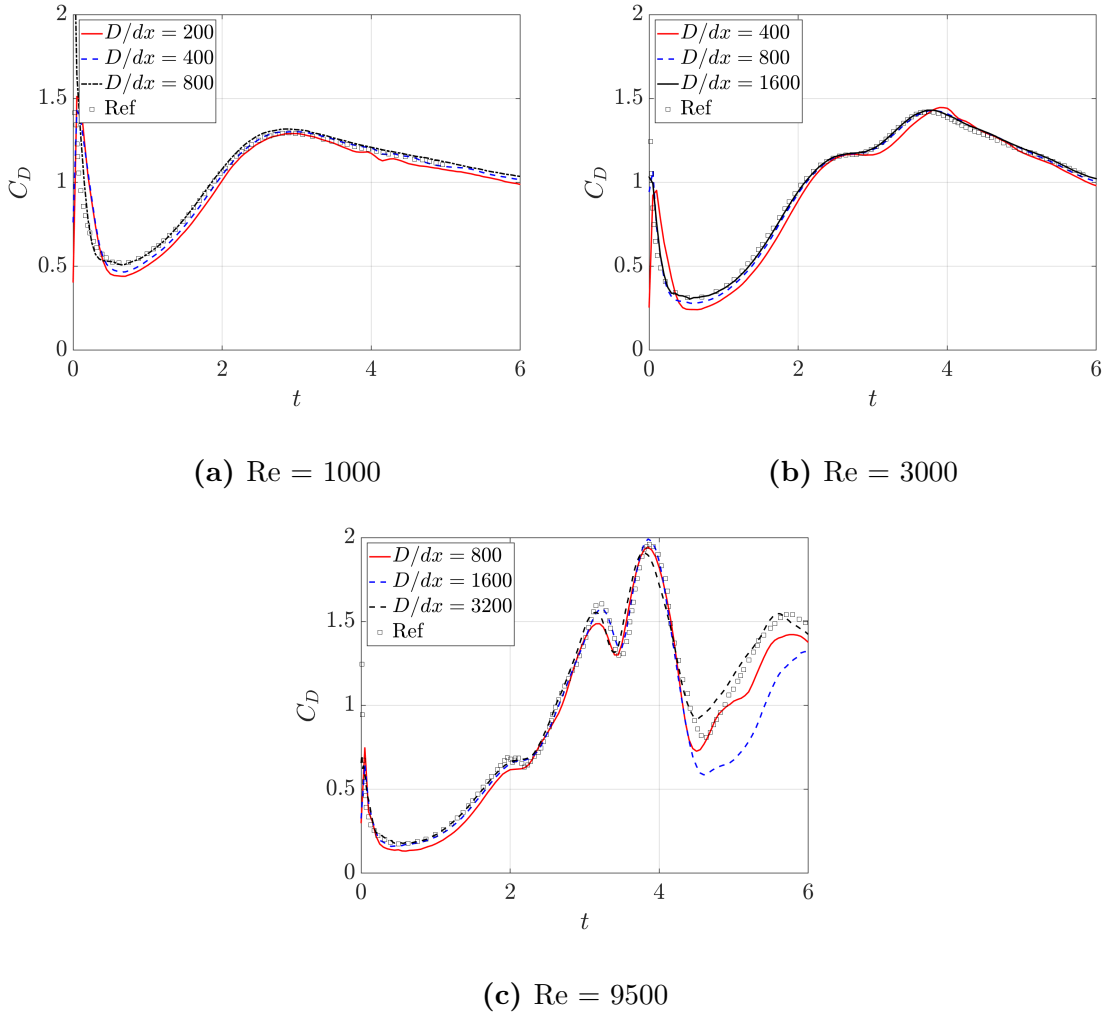
(b) Re = 3000

(c) Re = 9500

Figure 5.17 Drag coefficient for flow past a cylinder with (a) Re = 1000, (b) Re = 3000 and (c) Re = 9500. These SPH solutions are compared against numerical results in [118].

coefficient up to $t^* = 4$. For both Re = 1000 and Re = 3000 cases, the flow around the cylinder remains symmetrical with respect to the streamwise direction.

At Re = 9500, the interaction between the primary and secondary vortex pairs is more complex than for the other Reynolds numbers seen thus far. Figures 5.22 and 5.23 show the vorticity contours and streamlines, respectively. After the initial development of the boundary layer which happens in a similar way as in lower Reynolds numbers cases, a secondary vortex pair appears that displaces the primary vortices downstream, increasing the pressure drag and its relative force contribution.

(a) $t^* = 1$

(b) $t^* = 2$

(c) $t^* = 3$

(d) $t^* = 4$

(e) $t^* = 5$

(f) $t^* = 6$
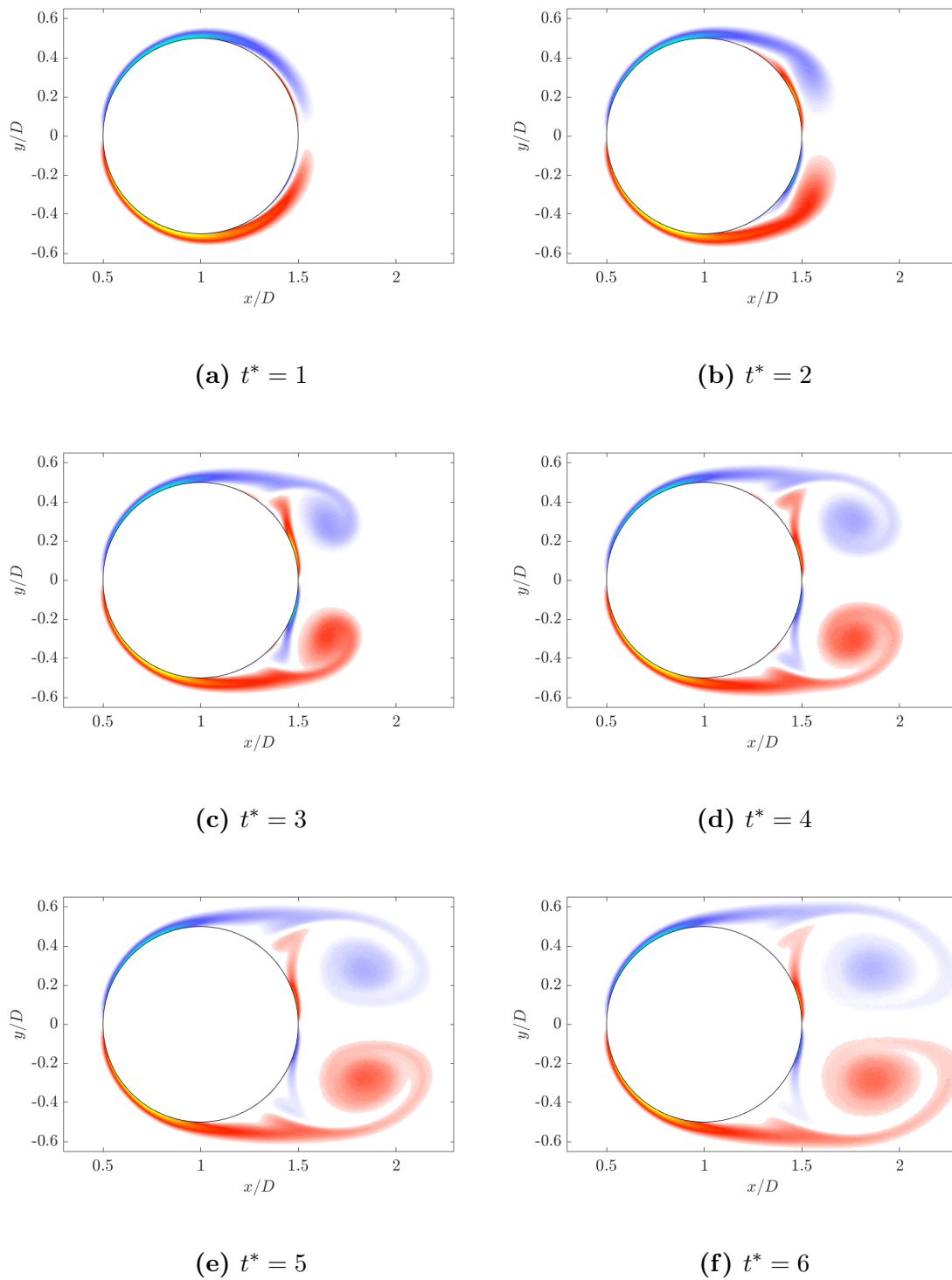
Figure 5.18 Vorticity contours for flow past a cylinder at Re = 1000

(a) $t^* = 1$

(b) $t^* = 2$

(c) $t^* = 3$

(d) $t^* = 4$

(e) $t^* = 5$

(f) $t^* = 6$
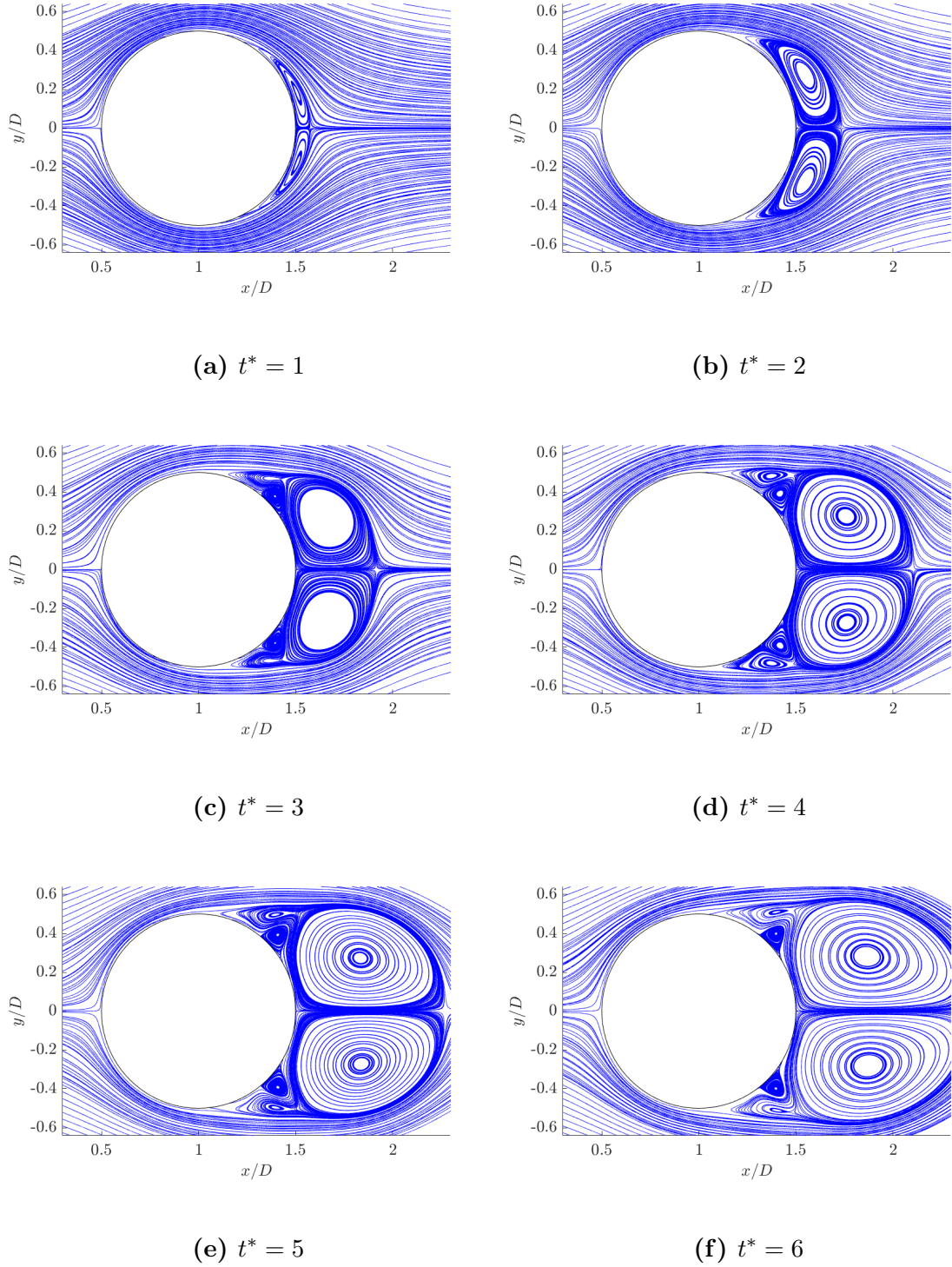
Figure 5.19 Streamlines for flow past a cylinder at Re = 1000

(a) $t^* = 1$

(b) $t^* = 2$

(c) $t^* = 3$

(d) $t^* = 4$

(e) $t^* = 5$

(f) $t^* = 6$
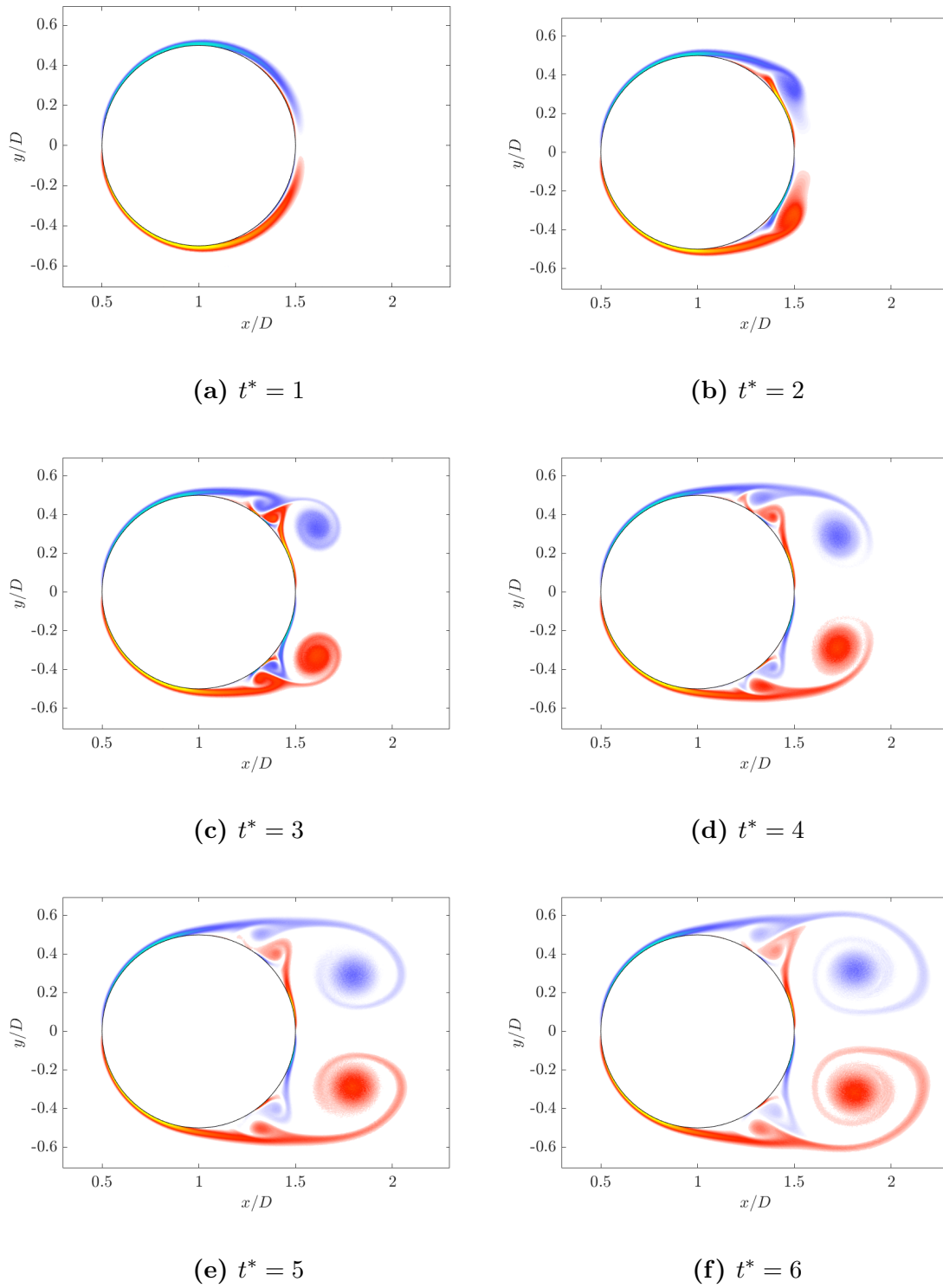
Figure 5.20 Vorticity contours for flow past a cylinder at Re = 3000

(a) $t^* = 1$

(b) $t^* = 2$

(c) $t^* = 3$

(d) $t^* = 4$

(e) $t^* = 5$

(f) $t^* = 6$
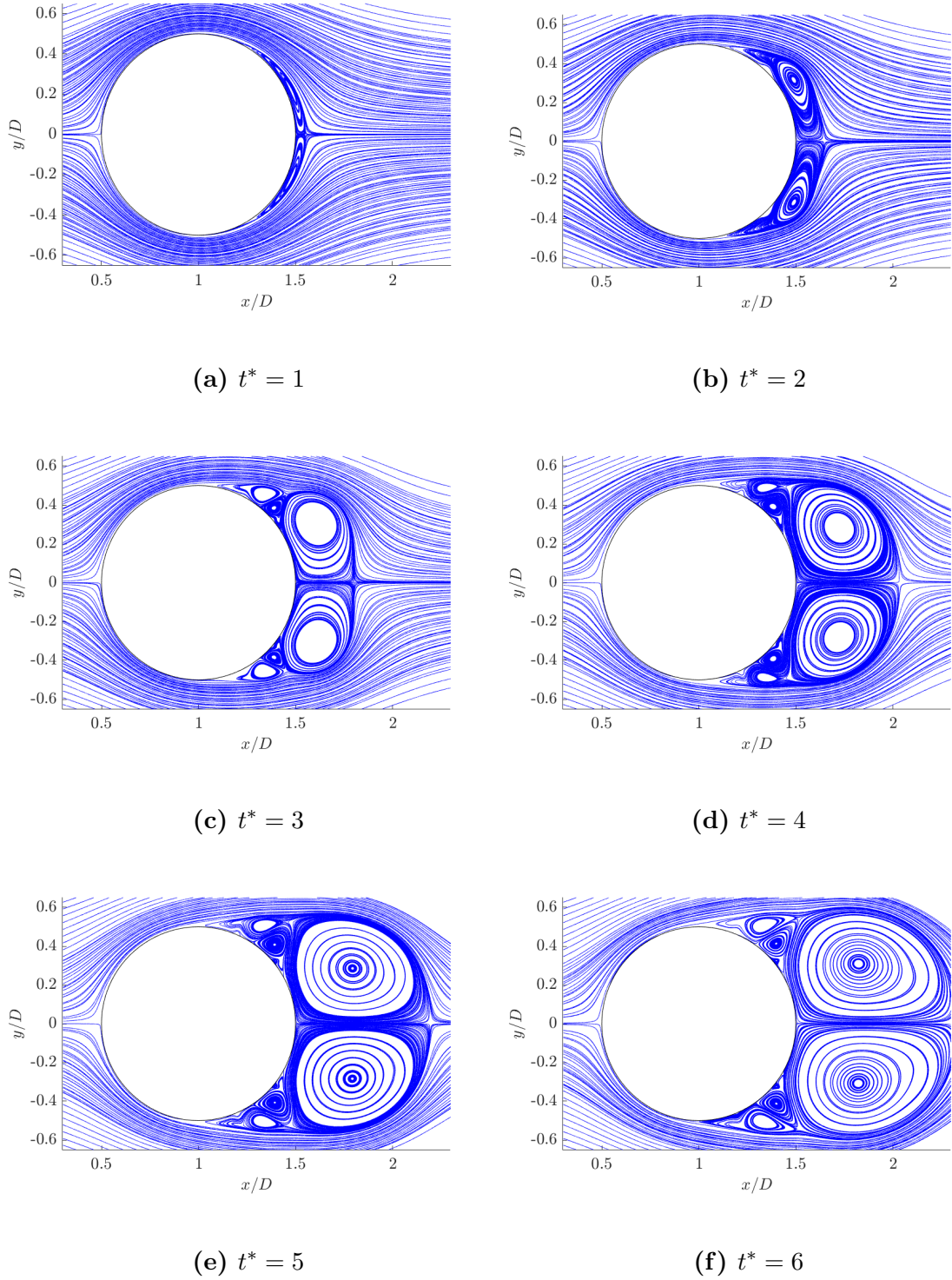
Figure 5.21 Streamlines for flow past a cylinder at Re = 3000

(a) $t^* = 1$ **(b)** $t^* = 2$

(c) $t^* = 3$ **(d)** $t^* = 4$

(e) $t^* = 5$ **(f)** $t^* = 6$
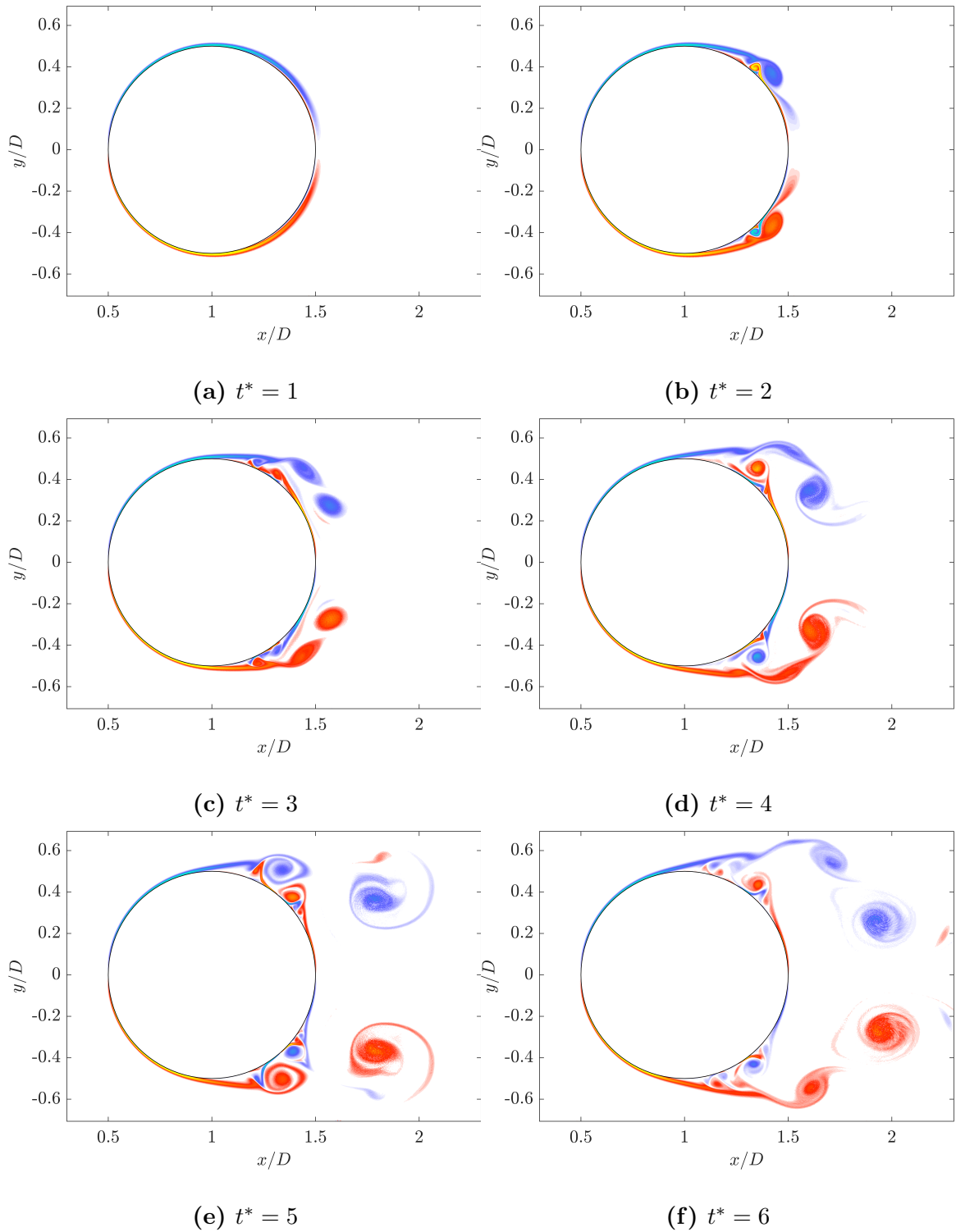
Figure 5.22 Vorticity contours for flow past a cylinder at Re = 9500

Around $t^* \approx 2$ [Figures 5.22(b) and 5.23(b)], the primary vortex pair detaches from the cylinder, as can be seen also by looking at the time history of the drag coefficient

(a) $t^* = 1$

(b) $t^* = 2$

(c) $t^* = 3$

(d) $t^* = 4$

(e) $t^* = 5$

(f) $t^* = 6$
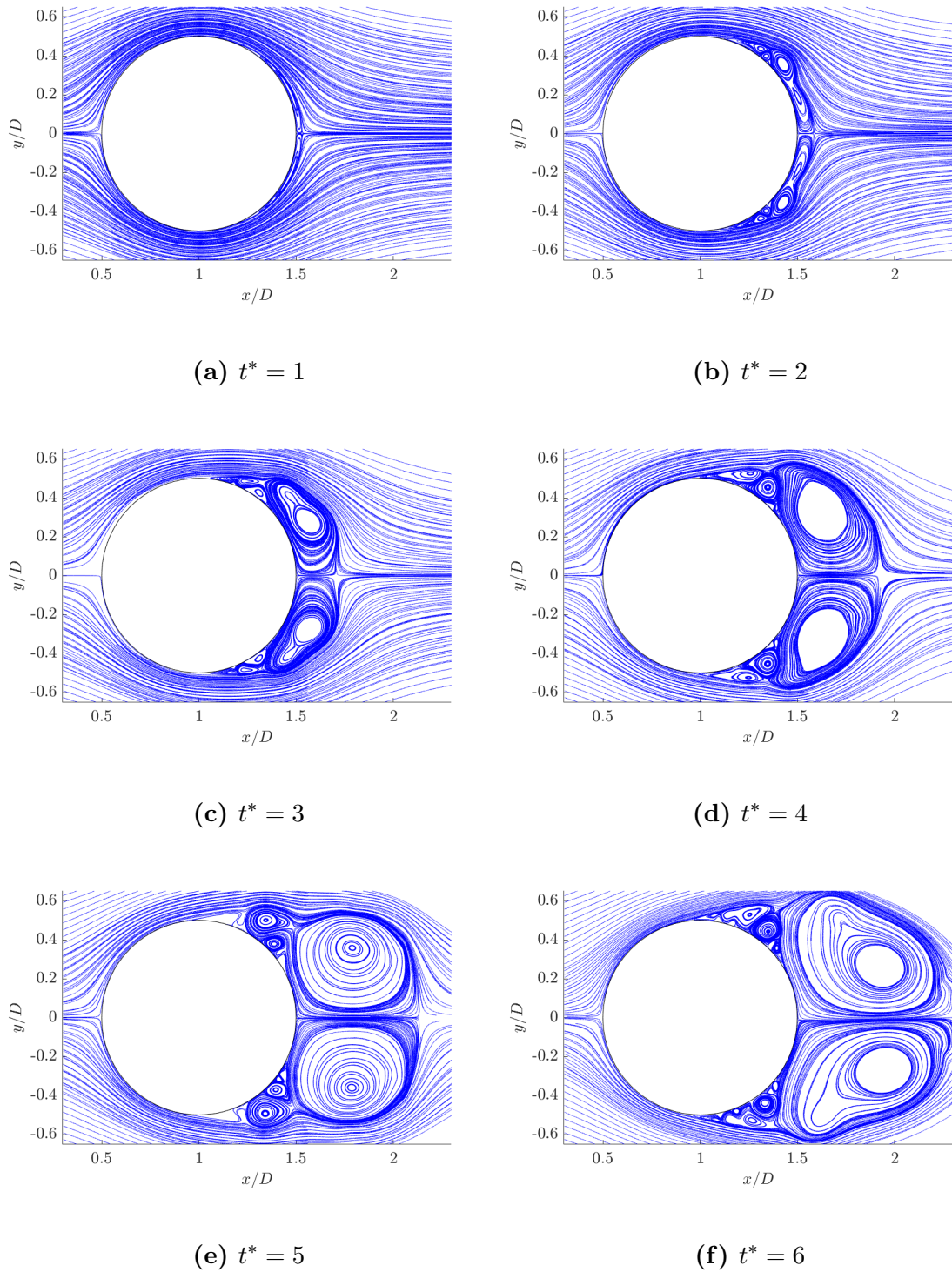
Figure 5.23 Streamlines for flow past a cylinder at Re = 9500

in Figure 5.17(c). Meanwhile, a new vortex pair is formed at a higher angle, and the same interplay between primary and secondary vorticity is observed, increasing the pressure drag up to $t^* = 3$. Interestingly, a $t^* = 4$, the second vortex pair merges with the previous, primary vortices after being separated from the body. The evolution at later times is dominated again by the complex interaction among vortices in the boundary layer, resulting in a highly unsteady flow. The convergence study performed for this last Reynolds number has resulted in using 6, 7, and 8 different resolution zones, reaching a maximum resolution near the cylinder equal to $D/\Delta x = 800, 1600, 3200$, respectively. The quantitative effect of these three different resolutions can be assessed in Figure 5.17(c), where the time history of the drag coefficient is shown. While all three resolutions capture the drag coefficient well until $t^* = 4$, only the simulation with $D/\Delta x = 3200$ is a good match with the reference solution for $t^* > 4$, when the flow is characterized by a high degree of unsteadiness. Moreover, with the highest resolution adopted, the flow remains almost perfectly symmetrical as is also the case for the reference solution in [118].

Contrary to what has been shown for Re = 100 and 200 in Section 5.3.2, no comparisons between multi-resolution and uniform resolution SPH simulations are shown here for Re = 1000, 3000 and 9500. This is mainly due to the prohibitive cost of running uniform resolution simulations for the three Reynolds numbers selected when the highest resolution has to be used. For example, the multi-resolution simulation for Re = 9,500 with $D/\Delta x = 3200$ requires 8 sub-domains, resulting in a total number of SPH particles deployed of $N \approx 10 \times 10^6$. Similarly, a uniform resolution SPH simulation with this level of particle spacing would require $N \approx 9 \times 10^9$ particles, which can be achieved only with sophisticated memory-distributed parallelization [63].

5.3.3 Flow past an oscillating, circular cylinder

The flow past a circular cylinder oscillating in a transverse direction to the streamwise direction is investigated for Re = 100 for different values of the oscillation amplitude and frequency. This test case generates complicated flows and it has been investigated with different techniques, including experiments computational studies [194] and experimental investigations [32, 33, 268, 5]. Herein, flow past an oscillating cylinder has been chosen to assess the capability of the proposed multi-resolution scheme to simulate flows with moving boundaries. The computational setup is the same as the one employed for studying the flow past a fixed cylinder case (see Section 5.3.2) and the domain has been discretized with three different resolution zones, with particle size equal to $D/\Delta x = 25, 50, 100$ (see Figure 5.10).

A sinusoidal motion $y(t)$ is applied to the cylinder in the cross-flow direction:

$$y(t) = ADsin(2\pi F f_s t) \tag{5.11}$$

where $A = y_{max}/D$, with y_{max} equal to the maximum displacement and $F = f_0/f_s$, where f_s is the frequency of the vortex shedding when the cylinder is fixed. The refinement regions also move according to Equation (5.11), so that the relative position of the cylinder with respect to the refinement areas does not change in time. Four different configurations of amplitude and frequency have been considered which can be found in Table 5.8.

In Figure 5.24(a), the time history of the lift coefficient C_L is shown for $[A, F] = [0.25, 0.9]$. This is defined as a "locked configuration" because the vortex shedding presents a dominant frequency equal to f_0, also corroborated by the Power Spectral Density (PSD) of the lift coefficient time signal shown in Figure 5.25(a), where only one peak is visible.

For an unlocked case, instead, the lift signal contains two or more frequencies, and this is achieved by changing the frequency ratio to $F = 0.5$ and $F = 1.5$. In the

Table 5.8 Amplitude and Frequency Values Chosen for the Simulation of Flow Past an Oscillating Cylinder

Case	A	F
1	0.25	0.9
2	0.25	0.5
3	0.25	1.5
4	1.25	1.5
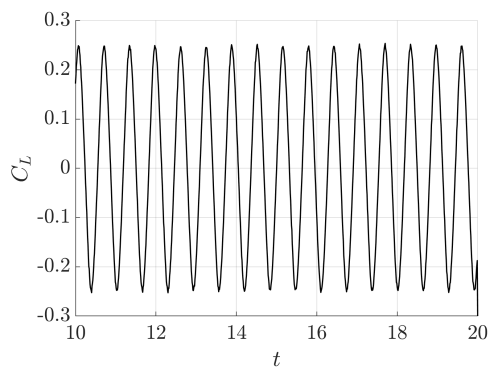
(a) $(A, F) = (0.25, 0.9)$
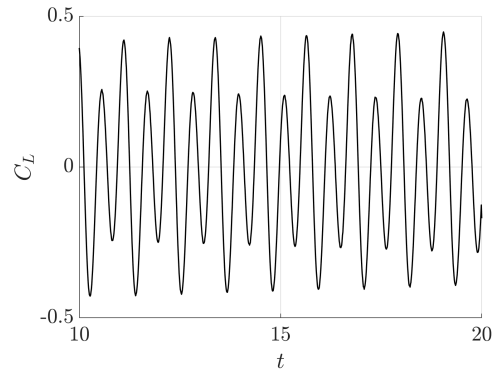
(b) $(A, F) = (0.25, 0.5)$
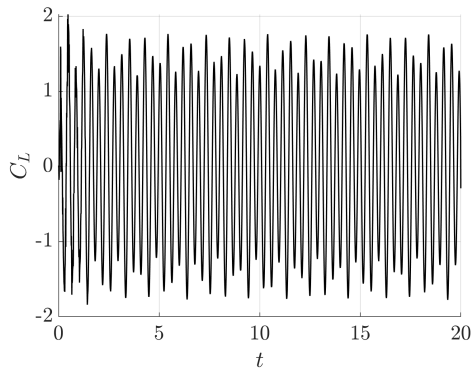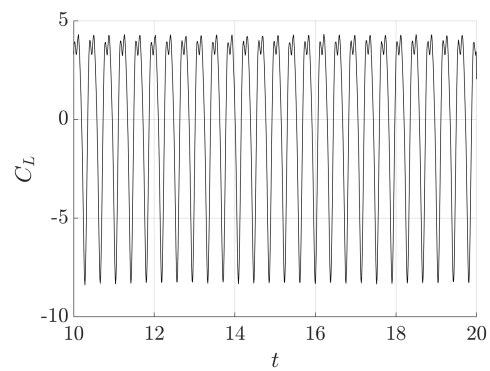
(c) $(A, F) = (0.25, 1.5)$

(d) $(A, F) = (1.25, 1.5)$

Figure 5.24 Time history of the lift coefficient for flow past an oscillating cylinder at Re = 100 for different amplitude A and frequency F ratios: (a) $(A, F) = (0.25, 0.9)$, (b) $(A, F) = (0.25, 0.5)$, (a) $(A, F) = (0.25, 1.5)$, (a) $(A, F) = (1.25, 1.5)$

first case, the periodic signal is characterized by two modes with different magnitudes and period $t_b = 2\,t_0$, where t_0 is the period of the imposed sinusoidal motion. This is

(a) $(A, F) = (0.25, 0.9)$

(b) $(A, F) = (0.25, 0.5)$

(c) $(A, F) = (0.25, 1.5)$

(d) $(A, F) = (1.25, 1.5)$
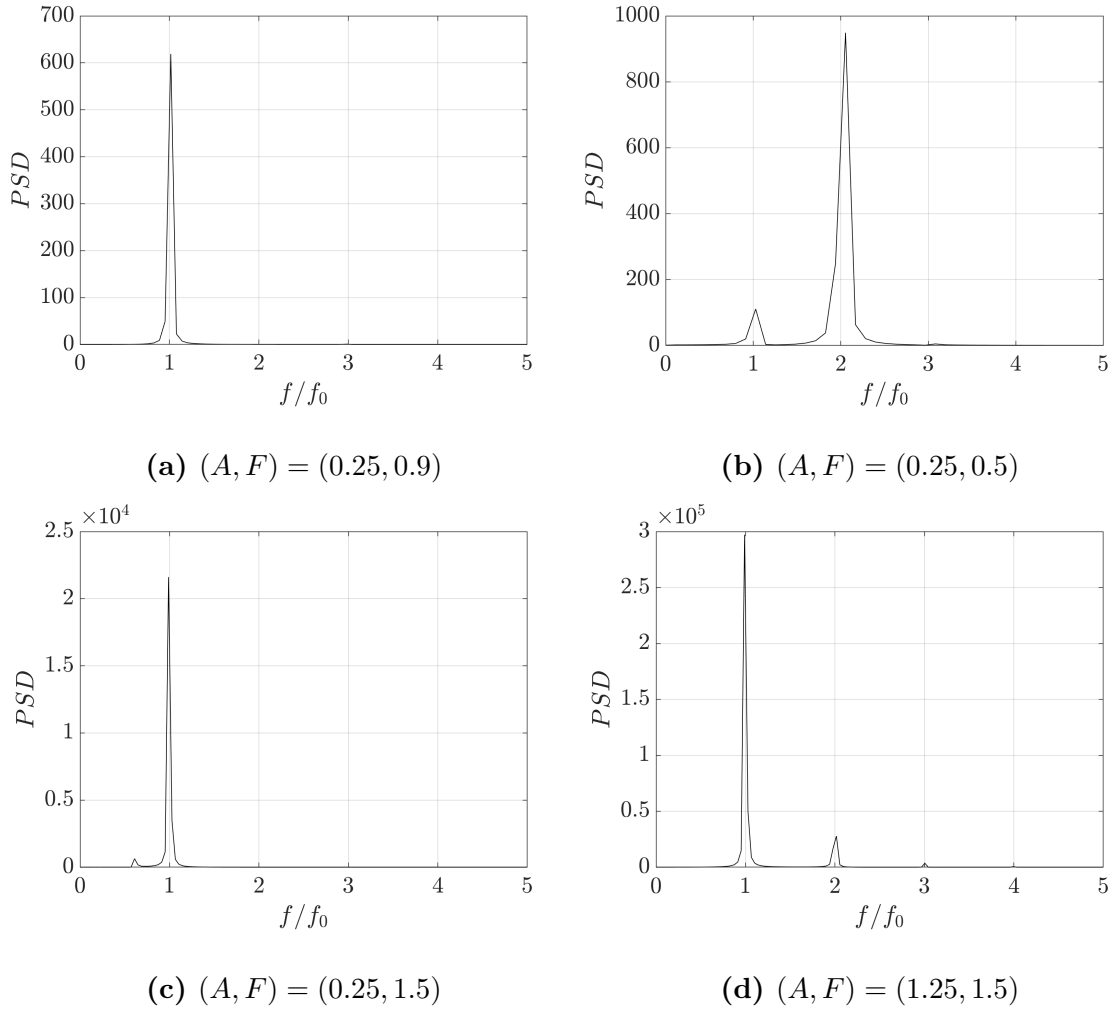
Figure 5.25 Power Spectral Density (PSD) for the flow past an oscillating cylinder at Re=100 for different amplitude A and frequency F ratio

confirmed by looking at the PSD in Figure 5.25(b), where two peaks associated with $f = f_0$ and $f = 2f_0$ can be observed in agreement with findings in [194]. The same beating phenomena [194] is also present for the $F = 1.5$ case, although in this case the lift coefficient has a period $t_b = 8t_0$.

The last case simulates a more challenging configuration obtained by using $(A, F) = (1.25, 1.5)$. Figures 5.24(d) and 5.25(d) highlight a dominant frequency $f = f_0$ coupled with a second $f = 2f_0$ and third $f = 3f_0$ frequency, in agreement with the results reported by [194]. These small secondary frequencies are not associated with beating phenomena, rather they influence the vortex shedding patterns, resulting

(a) $(A, F) = (0.25, 0.9)$ **(b)** $(A, F) = (0.25, 0.5)$

(c) $(A, F) = (0.25, 1.5)$ **(d)** $(A, F) = (1.25, 1.5)$
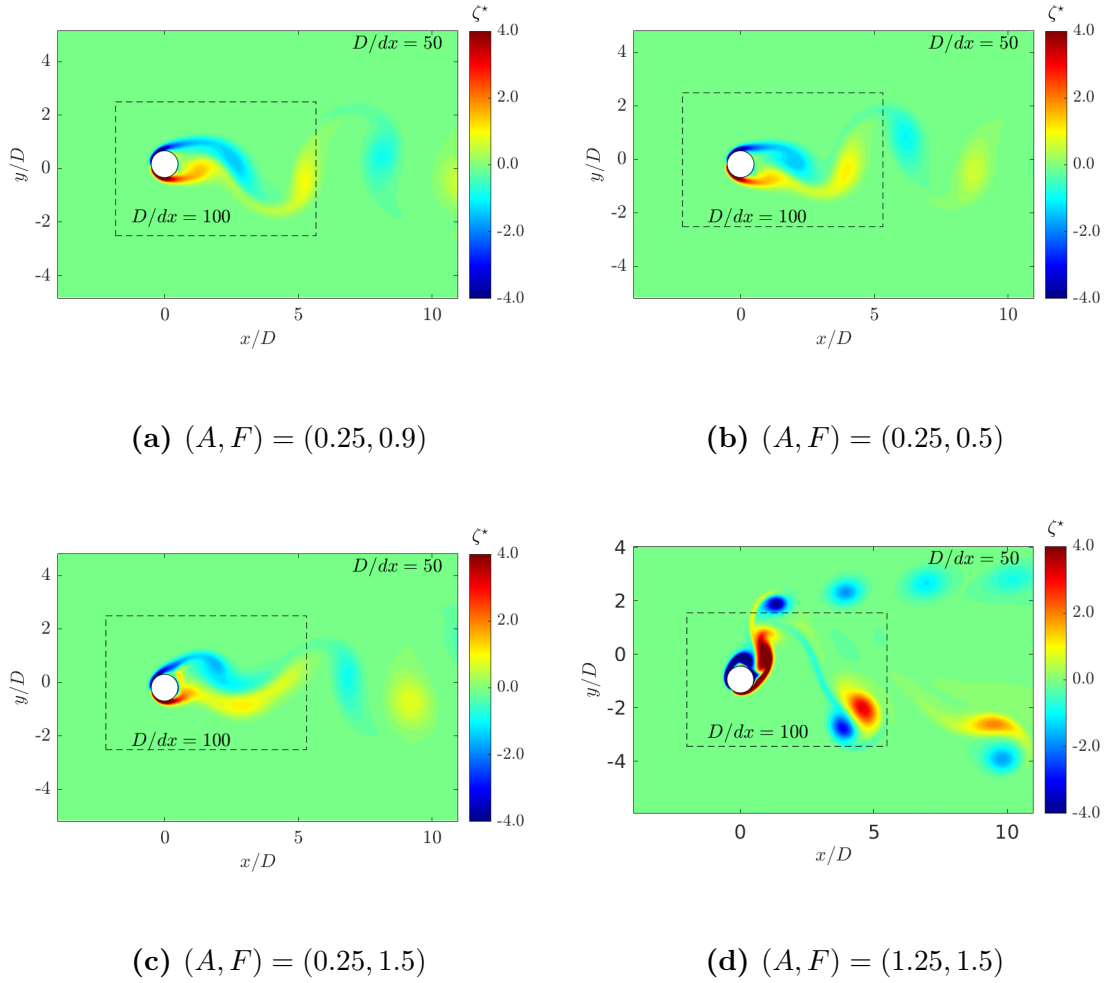
Figure 5.26 Contours of dimensionless vorticity for flow past an oscillating cylinder at $\mathrm{Re} = 100$ with different amplitude A and frequency F ratios

in a vortex pair plus a single vortex configuration, as can be seen in Figure 5.26, where the dimensionless vorticity contours are shown for all cases presented. In Figure 5.27, the SPH aerodynamic forces obtained keeping $A = 0.25$ fixed and varying the frequency ratio F are compared against the reference solutions in [194], showing a very good agreement especially in terms of the drag coefficient.

5.3.4 Propagation of regular waves

To demonstrate the ability of the proposed multi-resolution algorithm to deal with free-surface flow, the propagation of regular waves is investigated. The computational

(a) Drag Coefficient

(b) Lift Coefficient
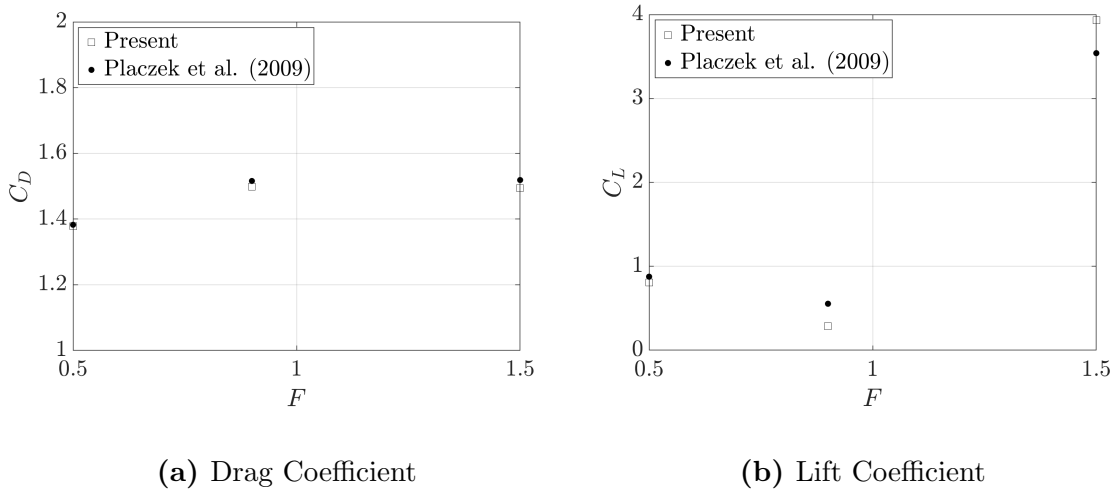
Figure 5.27 Comparison of SPH aerodynamic forces against results in [194] for flow past an oscillating cylinder with $A = 0.25$
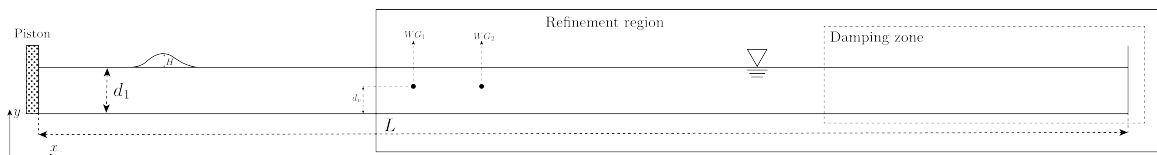
Figure 5.28 Computational domain for the propagation of regular waves case

domain is depicted in Figure 5.28 and consists of a rectangular tank with length $L = 16$ m filled with water up to a level $d_1 = 0.66$ m. Following Stokes' second-order wave theory, a piston-type wavemaker generates a train of regular waves with height $H = 0.2$ m and period $T = 2.0$ s for a total simulated physical time of $t = 80$ s, which gives approximately 40 waves throughout the simulation. The domain has been divided into two zones with different resolutions, a lower resolution zone on the left and a higher resolution zone on the right. Within the higher resolution region, a damping zone is placed at the right end to suppress any wave reflections (Figure 5.28).

A particle spacing $\Delta x = 0.01$ m is adopted in the left part of the domain (0 m $\leq x \leq 5$ m), while a resolution $\Delta x = 0.005m$ is adopted instead in the second region (5 m $\leq x \leq L$). To ensure accuracy and stability for the buffer interpolation procedure, especially when boundary particles are at the interface between the different resolution
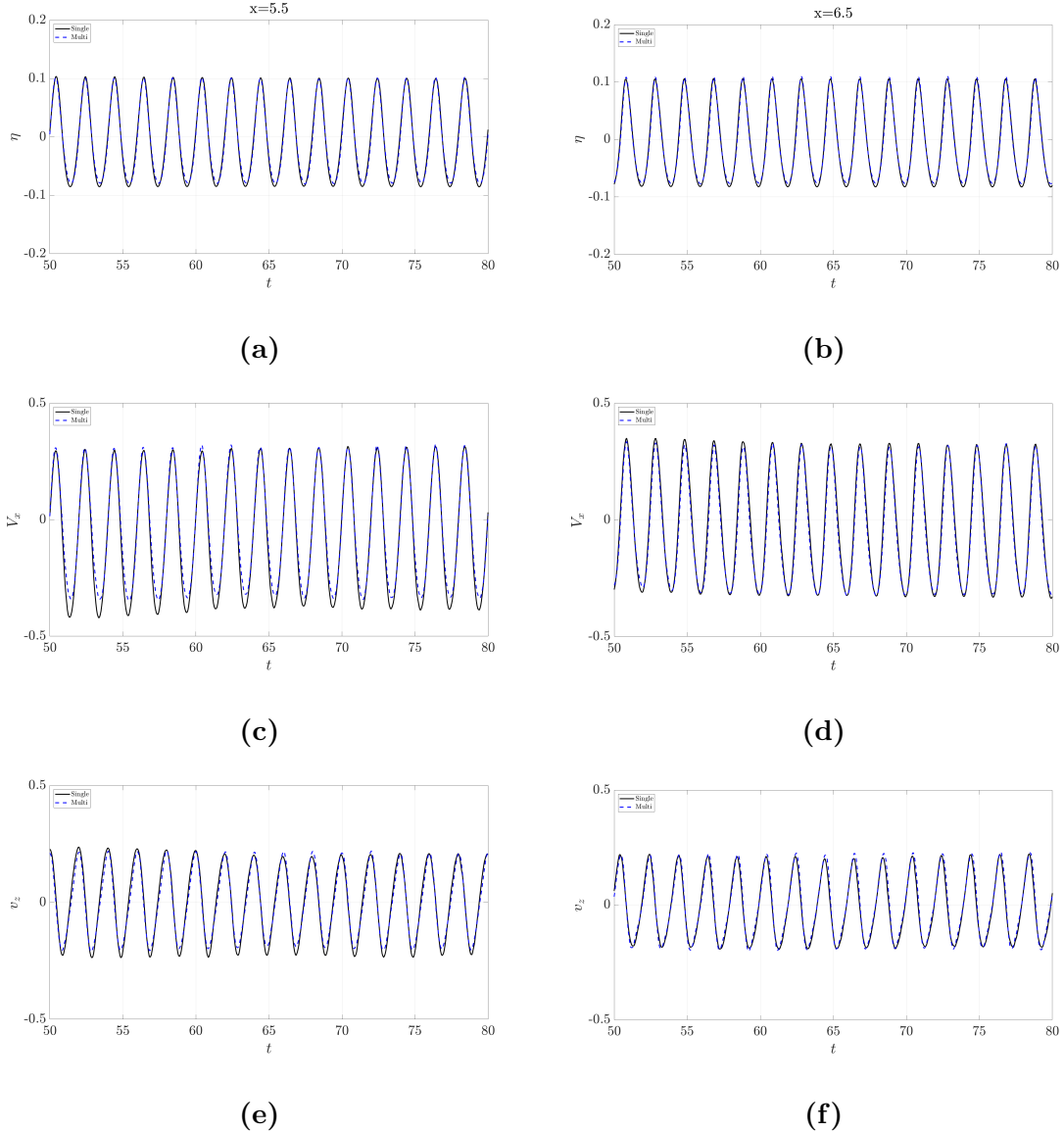
Figure 5.29 Comparison of free-surface elevation (a, b) and orbital velocities (c–f) between the multi-resolution and uniform resolution SPH simulations regular waves propagation

zones, the two regions are slightly overlapped, co-existing over a horizontal portion of the domain with length $2h_1$, where h_1 is the smoothing length of the coarser zone. The multi-resolution simulation is compared against another SPH solution obtained with uniform particle spacing $\Delta x = 0.005$ m everywhere. For the discretization of the viscous term in the governing equations, the artificial viscosity formulation is preferred with $\alpha = 0.02$ and the smoothing length to particle spacing ratio is set to
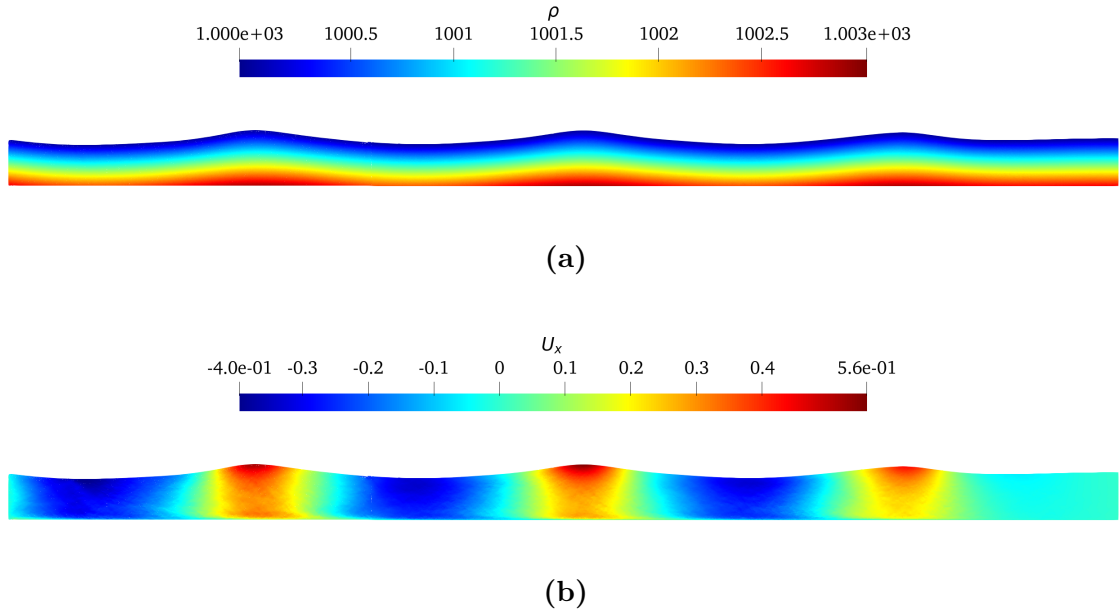
Figure 5.30 (a) Density and (b) velocity contours for the multi-resolution simulation for the wave propagation test case

$h/\Delta x = 2$. To measure the free-surface elevation and the orbital velocity, two wave gauges (WG1 and WG2) are placed at a height $d_v = 0.4$ m and a normal distance from the zonal interface of $x = 5.5$ m and $x = 6.5$ m, respectively.

In Figure 5.29, a comparison between multi- and uniform resolution simulations is shown. Starting from the top, Figures 5.29(a) and 5.29(b) show the good agreement obtained between both multi- and single-resolution simulations for the free-surface elevation, η. In Figures 5.29(c) and 5.29(e), the horizontal (v_x) and vertical (v_z) orbital velocities are compared at WG1 for both multi- and single-resolution, highlighting a slight underestimation of the velocity by the proposed variable resolution approach. This is however expected since the first wave gauge is close to the interface and, in the multi-resolution setup, the wave is first propagated across the coarse region with $\Delta x = 0.01$ m, while for single resolution the wave is propagated at $\Delta x = 0.005$ m throughout the domain. Therefore, a level of discrepancy is expected between the two solutions, mainly due to the different magnitude of the artificial viscosity. Nevertheless, this disagreement is resolved further downstream as seen in
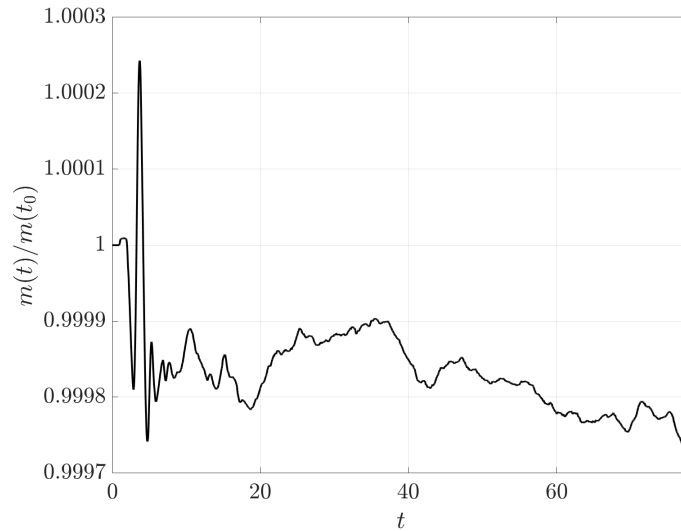
Figure 5.31 Time history of the mass variation in the multi-resolution simulation

Figures 5.29(d) and 5.29(f), where the two curves start overlapping again.

Figure 5.30 shows contours of density (top) and horizontal velocity (bottom). No clear discontinuities at the interface between the two sub-domains are noted, showing once again the ability of the present algorithm to propagate waves between SPH sub-domains with different resolutions with a good level of accuracy.

Finally, thanks to the absence of open boundary conditions, this test case allows some considerations on the mass conservation properties of the proposed approach. In Figure 5.31 is shown the time history of the mass for the multi-resolution simulation: despite the present approach doesn't enforce strict mass conservation, it can be seen that the mass variation in the total simulation is kept below 0.03%.

CHAPTER 6

3-D VALIDATION

This section extends the multi-resolution proposed in the previous chapter to the simulation of three-dimensional flow. Two different test cases are herein simulated in order to validate the present method: a flow past a sphere for $Re = 300$ and $Re = 500$ and a dam-breaking flow. Both the test cases are validated against experimental and numerical results available in the literature.

6.1 Flow Past a Sphere

The flow past a sphere, as the flow past a cylinder, has been extensively investigated as a simplified case of flow around bluff bodies with a general shape. Different transitions characterize this flow, and it evolves from a steady axisymmetric to an unsteady turbulent flow increasing the value of the Reynolds number. The first transition point has been individuated in [240] at $Re \approx 24$, where the flows detach from the sphere's wall, and a vortex ring develops in the wake. The flow remains steady and axisymmetric up to $Re \approx 210$ [147, 269], where the flow assumes a steady planar symmetric configuration [147, 179, 215]. At $Re \approx 277$, the flow becomes unsteady while maintaining its planar symmetry [102, 147, 215] up to $Re \approx 420$ when the flow transition to a chaotic system with multiple characteristic frequencies. After that threshold, the flow becomes increasingly complex until the complete transition to a turbulent flow for $Re > 10^3$.

6.1.1 Computational setup

The computational domain shown in Figure 6.1 is chosen to investigate the flow past a sphere for Re=300 and Re=500: a sphere with diameter $D = 0.1m$ is centered at $(x, y) = (0.0)$. The inlet is placed at a distance equal to $10D$ from
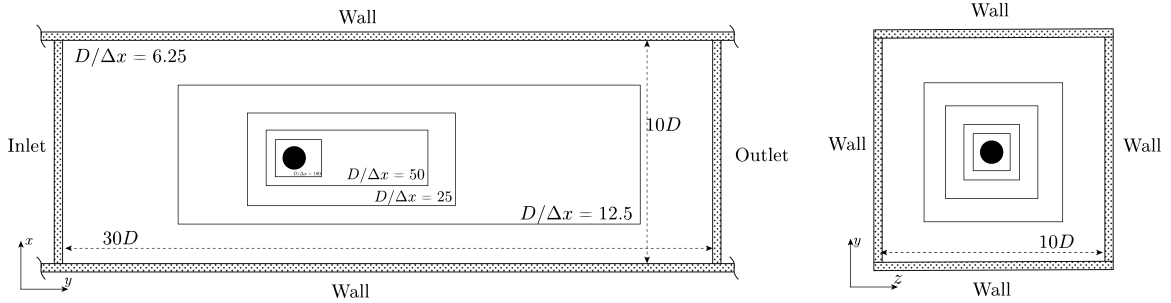
Figure 6.1 Longitudinal- and cross- sections of the computational domain for the flow past a sphere.

the sphere. At the same time, in the downstream direction, the computational domain is extended by $20D$ in order to resolve at least 3 vertical structures. A square cross-section with size $10D$ is used, which results in a blockage ratio approximately equal to 0.7%. The definition of the boundary conditions follows the setup followed in subsection 5.3.2: a no-slip boundary condition is applied to the sphere, while free-slip conditions are defined at the cross-section walls. Inlet-outlet boundary conditions and the initial conditions are imposed again in the same manner as in section 5.3.2. However, different from the two-dimensional study, the value of the smoothing length is $h = 1.5\Delta x$ in order to reduce the computational cost. The DDT in Equation 3.66 and the PST are applied to the entire domain.

For the setup of the refinement regions, a minimum resolution equal to $D/\Delta x = 6.25$ is chosen. As for the two-dimensional study on the flow past a cylinder, new sub-domains are nested inside the far field, each with a resolution that doubles as they get closer to the cylinder, with a maximum resolution equal to $D/\Delta x = 100$, which corresponds to a ratio between the boundary layer δ_{bl} and the particles size equal $\delta_{bl}/\Delta x \approx 6 - 5$ for a range $Re = 300 - 500$. It is noted that the total number of particles in these simulations is $Np \approx 11 \times 10^6$, while with a uniform resolution, the number of particles would have been equal to $N_p = 3 \times 10^9$.

Table 6.1 Numerical Results of the Drag Coefficient C_D, Lift Coefficient C_L and Strouhal Number St Values for the Flow Past a Sphere at Re=300

Case	C_D	ΔC_D	C_L	ΔC_L	St
Present	0.667	0.0032	0.066	0.017	0.134
Costantinescu and Squires [46]	0.655	0.0032	0.065	–	0.136
Johnson and Patel [102]	0.656	0.0035	0.069	0.016	0.138
Tomboulides and Orszag [242]	0.671	0.0028	–	–	0.136
Ploumhans et al. [195]	0.683	0.0025	0.061	0.014	0.13

6.1.2 Re=300

Herein, the first case considered is for a Reynold Number $Re = 300$. The flow is simulated for an overall duration of $t^* = 250$ time unit, where $t^* = tU/D$, and only the last 120 time units are considered for collecting the flow statistics.

In Figure 6.2(a) the time history of the aerodynamical coefficients is shown: the average value of the drag $C_D = F_x/(0.5\rho U_\infty^2 \pi D^2/4)$ and lift $C_L = F_y/(0.5\rho U_\infty^2 \pi D^2/4)$ are respectively 0.667 and 0.066 with an oscillation amplitude ΔC_D and ΔC_L equal to 0.0032 and 0.17. These values agree with other numerical investigations, as seen in Table 6.1, where the present results are summarized and compared against the literature. From Figure 6.2(a) is also evident that the side coefficient $C_S = F_y/(0.5\rho U_\infty^2 \pi D^2/4)$ is equal to 0, indicating that the plane (x, y) is a plane of symmetry for the present flow, as expected from previous experimental and numerical investigations with $Re = 300$ [242, 102].

From the frequency analysis in Figure 6.2(b), where the Power Spectral Densities of C_D and C_L are reported, it can be found the value of the non-dimensional vortex shedding frequency $St = 0.134$, which is again in agreement with other numerical investigation, for example with the results in [242] where is predicted at a value $St = 0.137$. Interestingly, as in [102], the drag coefficient presents a peak in the spectrum at a value equal to $2St$, which is not present in the lift coefficient spectrum.
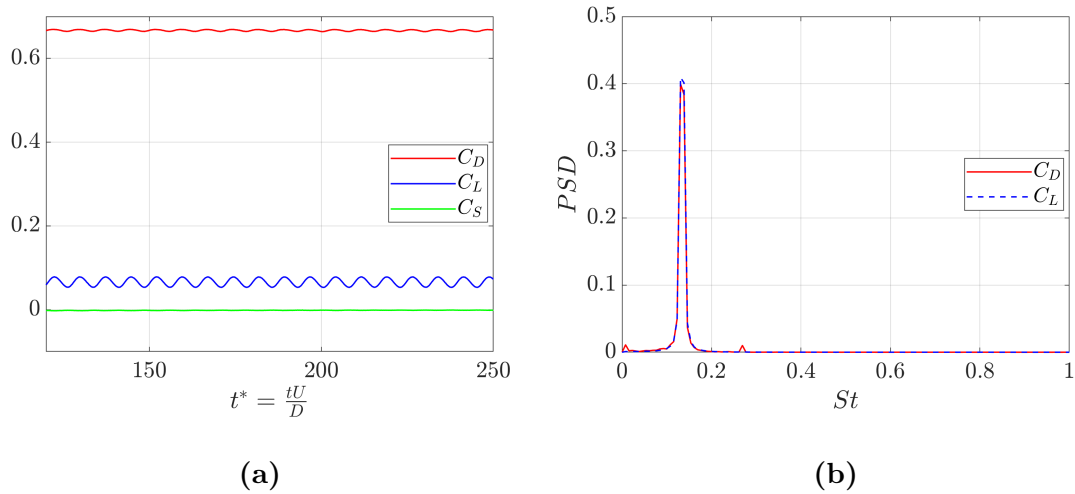
Figure 6.2 (a) Time histories and (b) normalized power spectral densities of the aerodynamic coefficients for the flow past a sphere at $Re = 300$.

To further investigate this aspect, Figure 6.3 displays the time history of the stream-wise velocity and its power spectral density at a point distant $5.75D$ from the sphere in the downstream direction. The only peaks present are at a value equal to $St = 0.134$, along with its three super-harmonics at $2St$, $3St$, and $4St$, as in [242].

Figure 6.4 presents the average streamwise velocity U_{avg} along the wake centerline, with a comparative analysis against the numerical outcomes from [242]. A good correlation is observed up to a point $x/D = 7$, beyond which the displayed results indicate lower values for U_{avg}. The root-mean-square value of the streamwise velocity on the same centerline is also highlighted in the figure, with the current simulation predicting a diminished peak value at $x/D = 1.7$. Further downstream there is a reasonable agreement between the two sets of results.

The flow visualization displayed in Figures 6.5-6.6, where the Q criterion, a vortex identification method, is shown at every quarter of the vortex shedding period, helps understand the development of the vortical structures in the wake. In Figures 6.6(a)-6.5(a), a vortex is about to separate from the vortical structures surrounding the sphere. This coherent structure is convected downstream, as can be seen in Figures 6.6(b)-6.5(b)), where are now clearly visible the legs of the hairpin vortex.

Figure 6.3 (a) Time history and (b) normalized power spectral density of the value of the streamwise coefficient at a $x/D = 5.75$ on the wake centerline for the flow past a sphere at $Re = 300$.
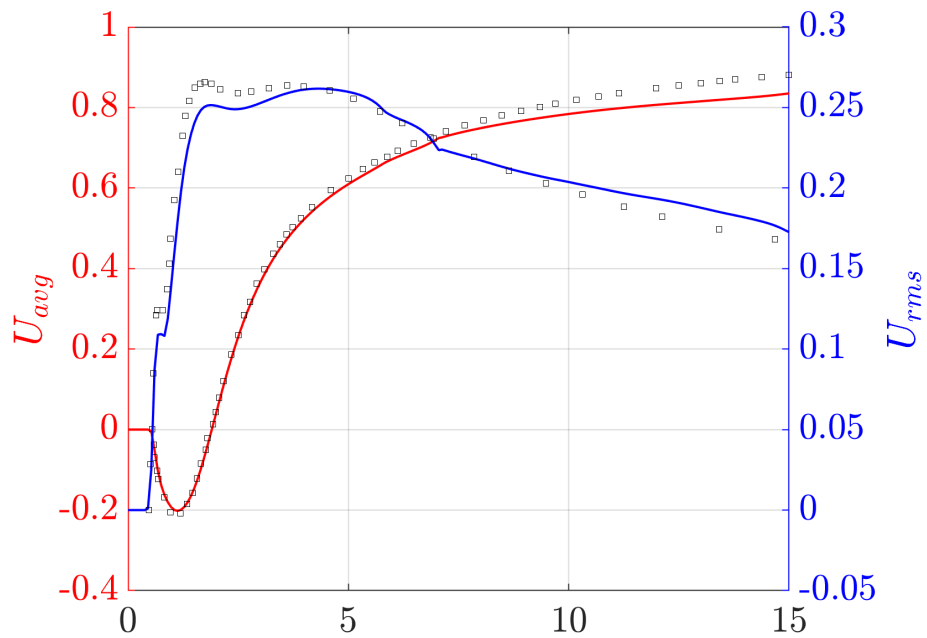
Figure 6.4 Comparison of the average and root-mean-square values of the streamwise velocity along the wake centerline with the numerical results in [242]

While the shed-wake structure moves further away from the sphere [Figures 6.6(c)-6.5(c)], a new structure, resulting from the interaction between the wake and the outer flow, is formed around the legs of the hairpin vortex (6.6(d)-6.5(d)). The last figure also shows the development of a new coherent structure in the near-wake region. To summarize, the vortex-shedding mechanism is characterized by two hairpin structures oriented in opposite directions; one results from the wake-shed, the other from the interaction between the wake and the outer flow.

6.1.3 Re=500

To further validate the present multi-resolution algorithm, the Reynolds number is raised up to 500, where the flow past a sphere is characterized by the loss of the planar symmetry and a more complex vortex shedding. The numerical simulation is computed for a total of $t^* = 300$ time unit, and the last $t^* = 180$ are used to collect the statistics.

In Figure 6.7(a), the time history of the force coefficient is reported. The average value of C_D of the present simulation is equal to 0.566, which is in perfect agreement with the results in [160]. With respect to the case with $Re = 300$, the loss of planar symmetry can be discerned from the evolution of the side coefficient.

The spectral analysis of the aerodynamical coefficients is reported in Figure 6.7(b), reveals the more complex nature with respect to the case with $Re = 300$, where only one dominant peak, corresponding with the vortex shedding frequency, was present in the spectrum of C_D. Instead, in this case, the power spectral density of the drag coefficient is characterized by different peaks, with the dominant one at $St_2 = 0.44$, which is close to the value found in [126, 51]. As for the previous case, to further analyze the flow's spectral characteristic, in Figure 6.8, the normalized power spectral densities for the stream-wise velocity are shown, and the pressure at three different locations in the near wake region, chosen to match the same measurement

(a)

(b)

(c)

(d)
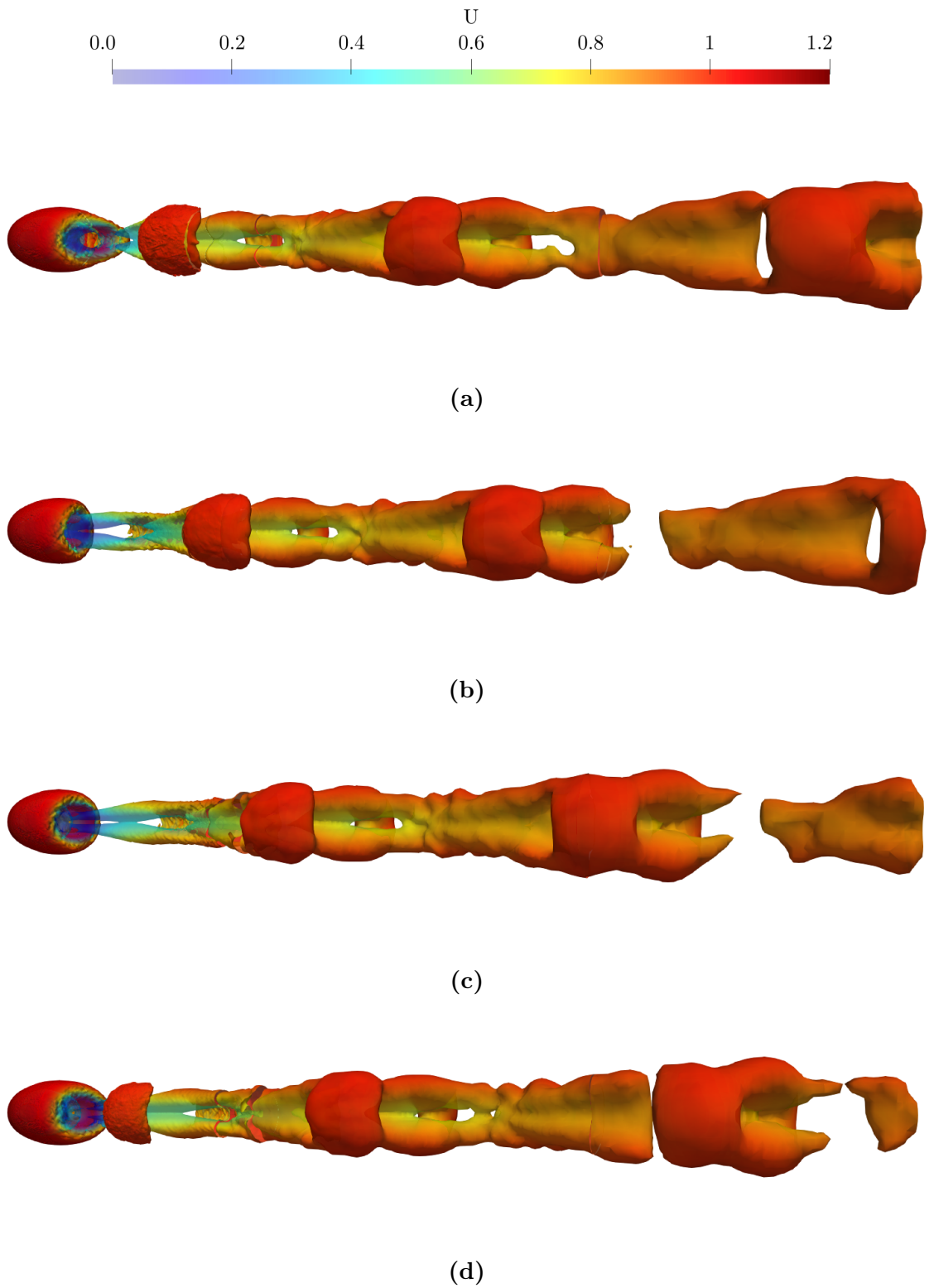
Figure 6.5 Flow visualization by the Q criterion, colored by the velocity magnitude U, at every quarter of period from a view normal to the (x, z) plane for the flow past a sphere at $Re = 300$.

(a)

(b)

(c)

(d)
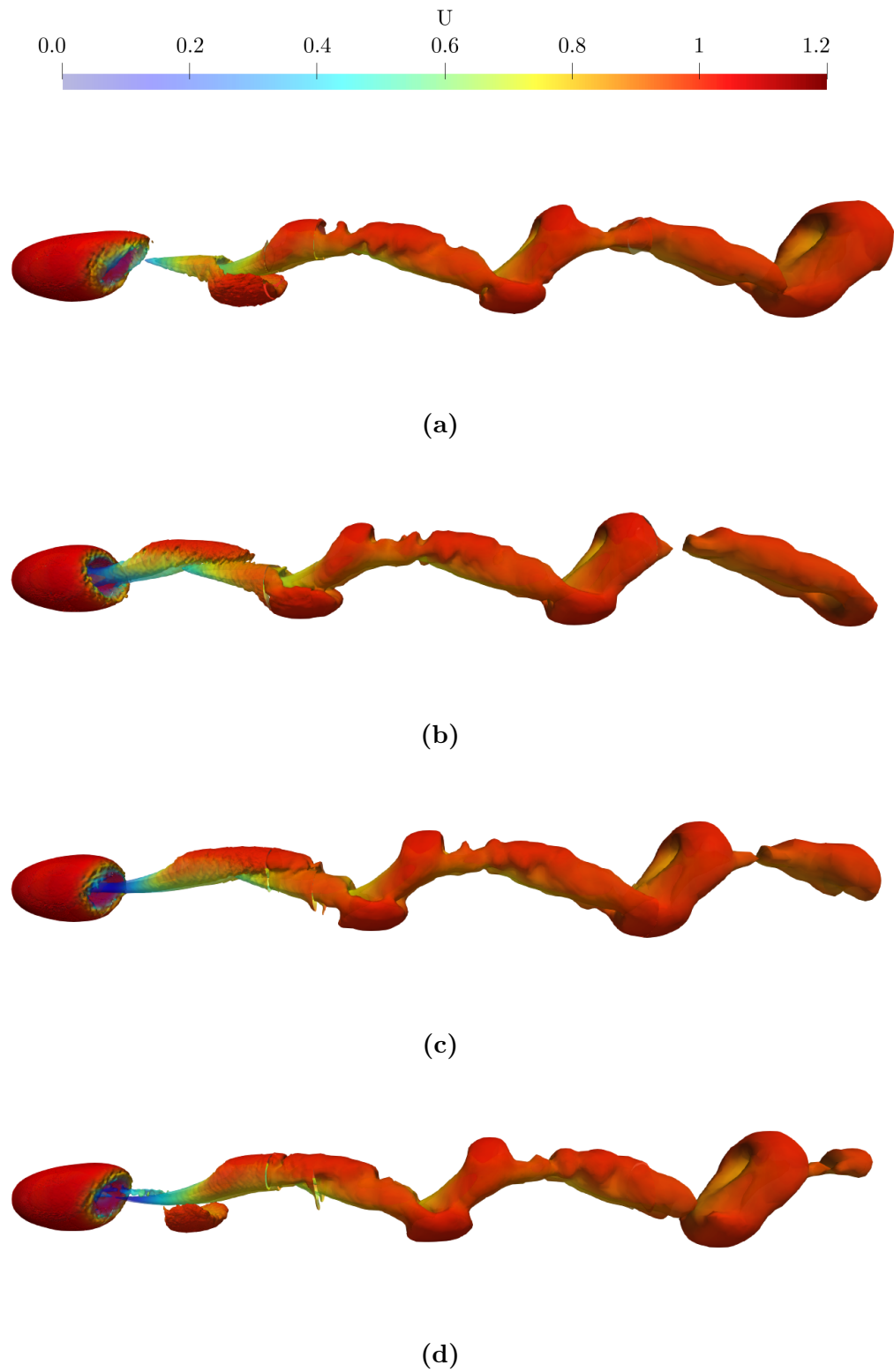
Figure 6.6 Flow visualization by the Q criterion, colored by the velocity magnitude U, at every quarter of period from a view normal to the (x, y) plane for the flow past a sphere at $Re = 300$.
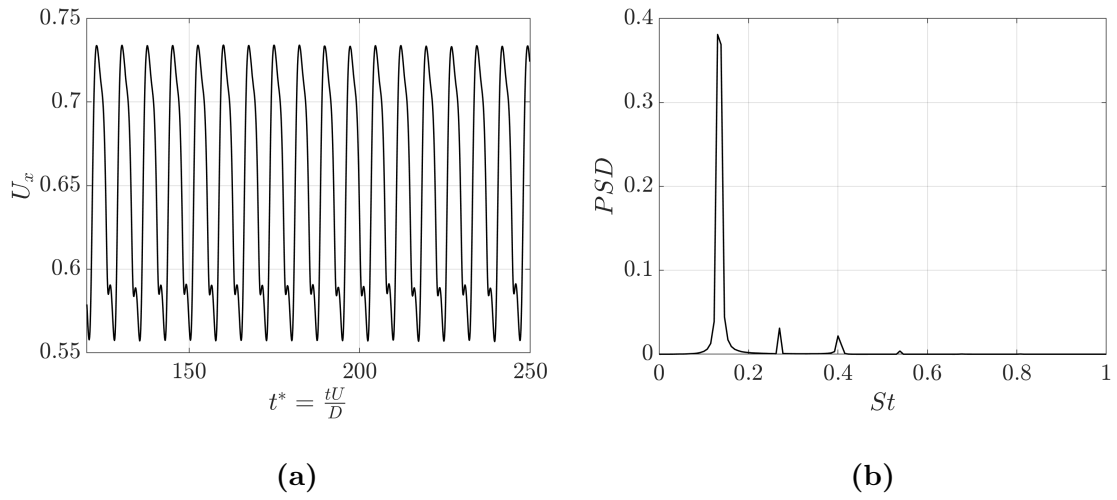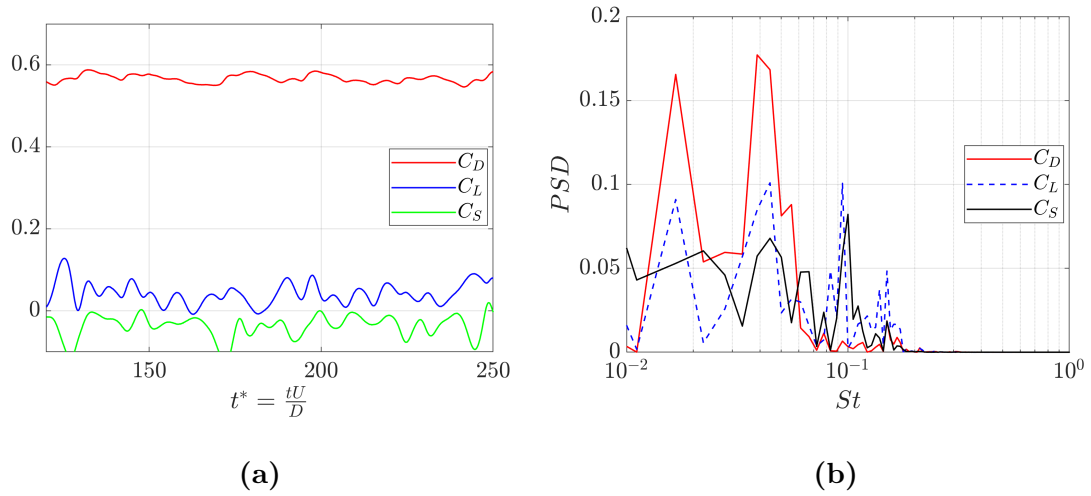
Figure 6.7 (a) Time histories and (b) normalized power spectral densities of the aerodynamic coefficients for the flow past a sphere at $Re = 500$.

Table 6.2 Numerical Results of the Drag Coefficient C_D, Strouhal Number St_1 and St_2 Values for the Flow Past a Sphere at Re=500

Case	C_D	St_1	St_2
Present	0.566	0.0167	0.044
Mittal and Najjar [160]	0.56	0.150	0.05
Lee [126]	0.54	0.164	0.045
Tomboulides and Orszag [242]	-	0.167	0.045
Crivellini et al. [51]	0.558	0.157	0.044

points in [242, 51]. The first point on the wake centerline at $(x, y, z) = (2.5D, 0, 0)$ shows the presence of two different frequencies, one at $St_2 = 0.44$, the second at $St_1 = 0.166$, while at locations 2 and 3, the dominant frequency is the $St_1 = 0.166$. The values of the low and high frequencies found are in good agreement with the results in [242], as can be seen from Table 6.2, where the value of the drag coefficient and the Strouhal numbers found in this study are compared against other experimental and numerical investigations.
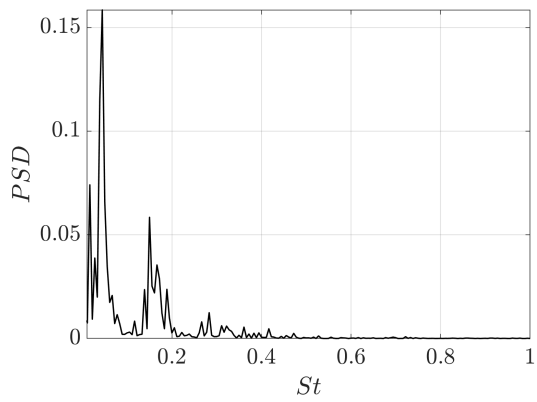
(a) Streamwise velocity
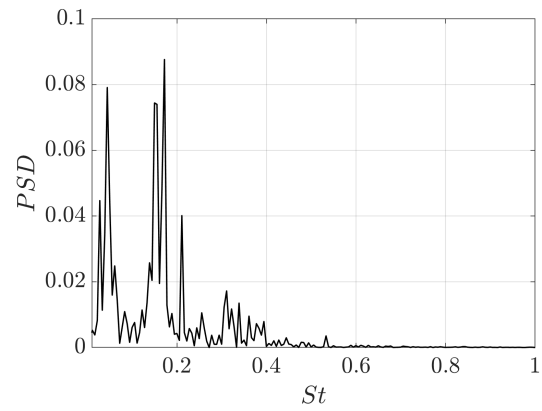
(b) Pressure
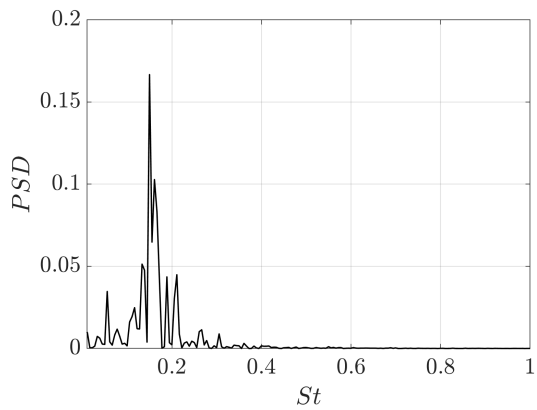
(c) Streamwise velocity
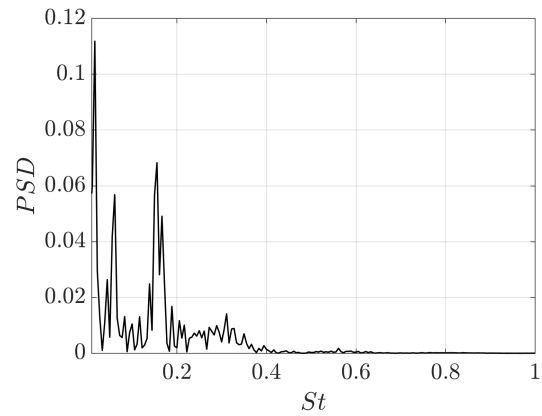
(d) Pressure
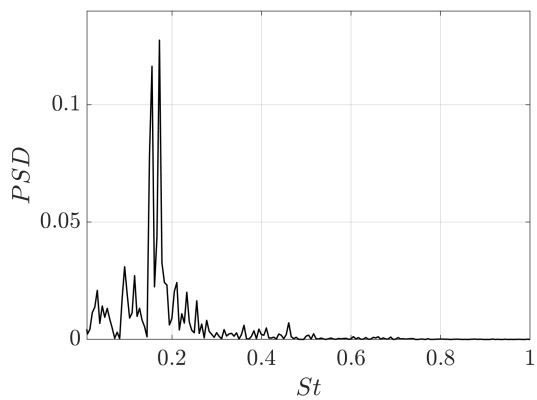
(e) Streamwise velocity
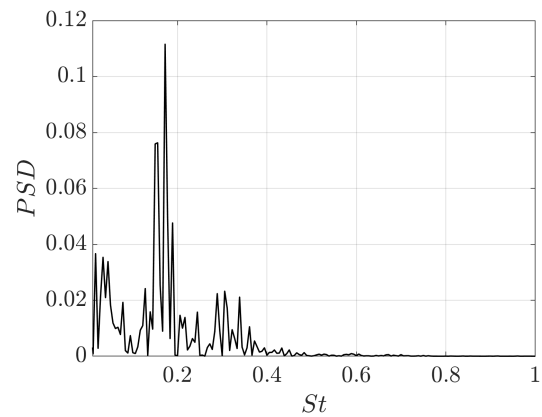
(f) Pressure

Figure 6.8 Normalized power spectral density for the streamwise velocity and pressure at (a)-(b) $(x, y, z) = (2.5D, 0, 0)$, (c)-(d) $(x, y, z) = (2D, 0.3, 0)$, (c)-(d) $(x, y, z) = (2D, 0.0, 0.3)$, for the flow past a sphere at $Re = 500$.

In Figure 6.9 the iso-surfaces for the Q criterion at every period $T_1 = 1/St_1$ are displayed: it is clear that the St_1 is the frequency of the vortex shedding mechanism, which resembles the same shedding process seen at $Re = 300$, although in this case, the vortex structure sequence is more irregular. Moreover, it can be seen that the vortex orientation changes from cycle to cycle.

6.2   3-D Dam-Breaking Flow

Herein, the ability of the proposed multi-resolution algorithm to deal with three-dimensional free-surface flows is validated by simulating a dam-breaking flow that impacts an obstacle. This test case is very popular in the SPH community and has been chosen as SPHERIC benchmark case #2. The configuration of the numerical experiment [113] is reported in Figure 6.10.

A baseline spatial resolution $\Delta x_{max} = 0.005$ is chosen, and a refinement region has been defined around the obstacle, wherein a finer resolution of $\Delta x_{min} = 0.0025$ is applied, as shown in Figure 6.11. A uniform value across the different sub-domain for the smoothing length to particle distance is set equal to $h/\Delta x = 1.5$.

The reference density has a value equal to $\rho_0 = 1000$ kg/m^3, while the gravitational accelleration $\mathbf{g} = -9.81$ m/s^2. The sound speed is chosen equal to $c_0 = 10\sqrt{\mathbf{g}H}$, where $H = 0.55m$ is the height of the water column. To ensure the numerical stability, an artificial viscosity model with $\alpha = 0.01$ is used, which corresponds to a physical kinematic viscosity $\nu = 8.6 \times 1-^{-5}$, along with the DDT term in Equation 3.66. No-slip wall boundary conditions are enforced on the walls.

Figure 6.12 shows the comparison between the numerical simulation and the experimental results of [113] at the pressure probes placed on the front side of the obstacles. A good agreement is found at gauges P1 and P2, where the numerical solution is able to predict quite well the evolution of the pressure at the first impact. Some discrepancies are instead found at P3 and P4, where the SPH simulation under-

ω_x

-23.2   20.2

(a) T_1

(b) $2T_1$

(c) $3T_1$

(d) $4T_1$
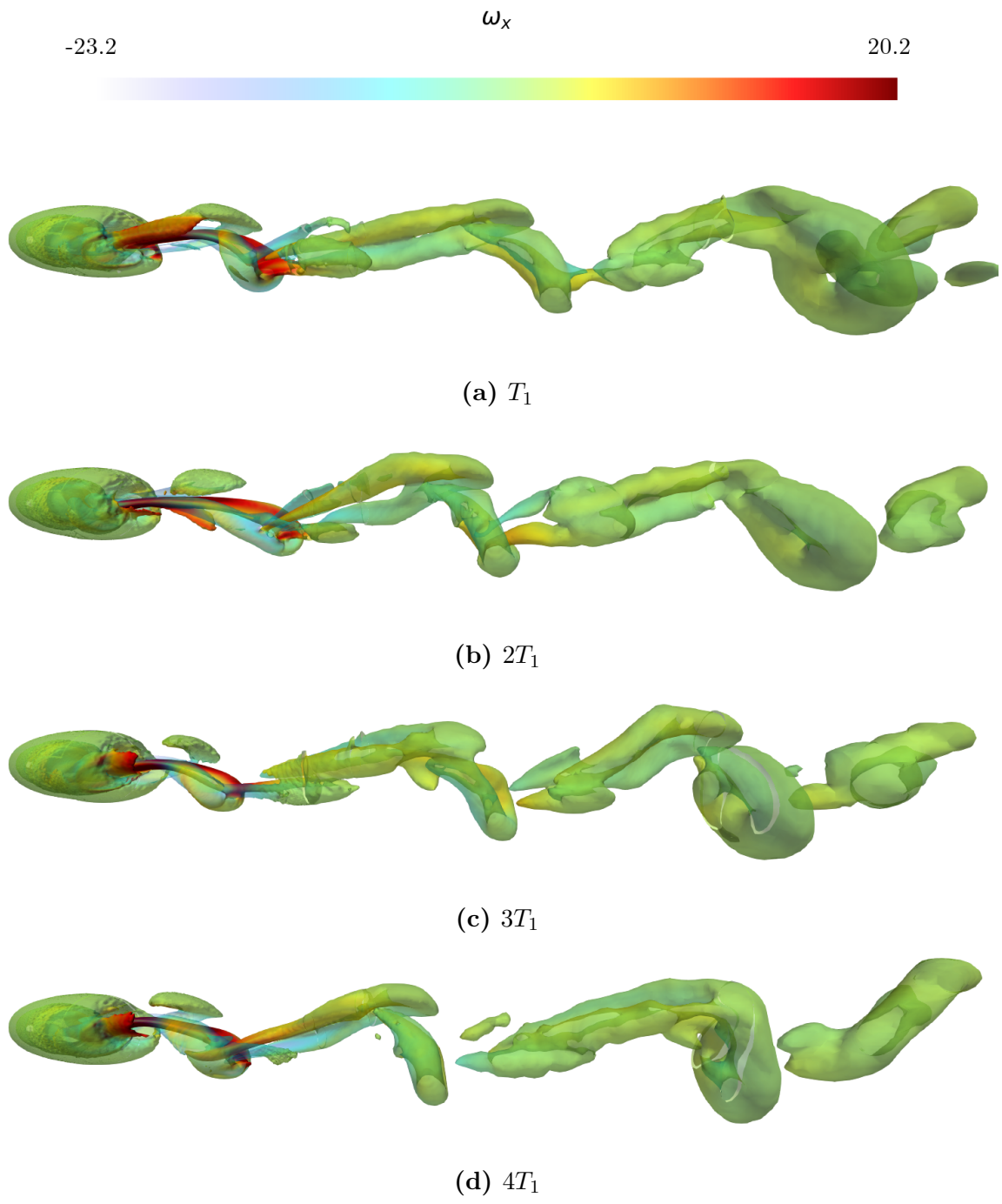
Figure 6.9 Flow visualization by the Q criterion, colored by the vorticity ω_x, at every period $T_1 = 1/St_1$ from a view normal to the (x, y) plane for the flow past a sphere at $Re = 500$.
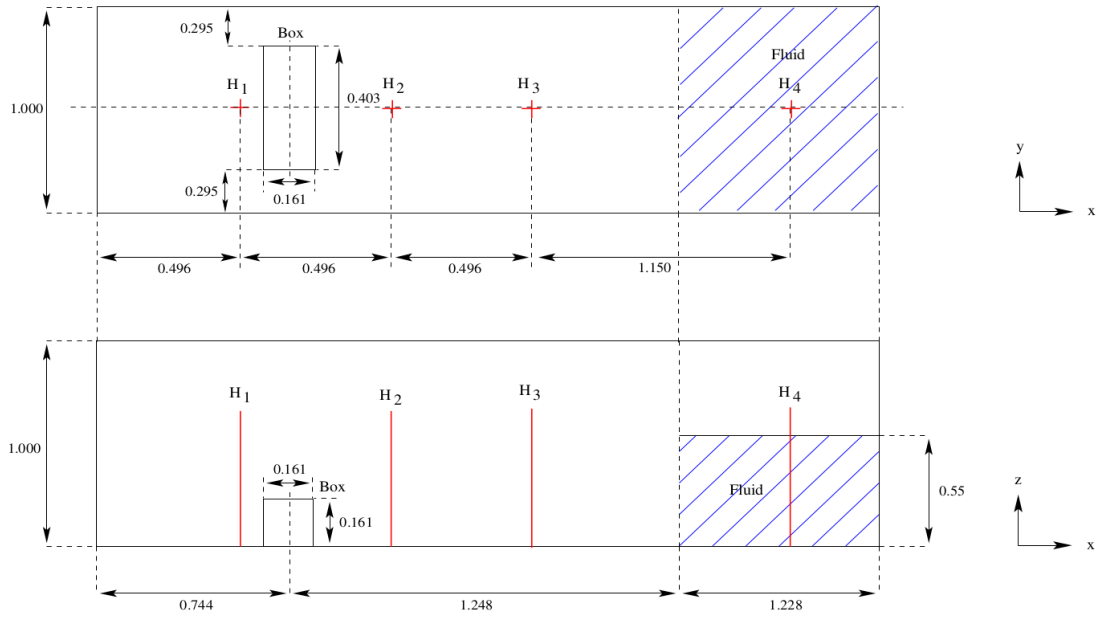
(a) Top and side view of the experimental configuration.
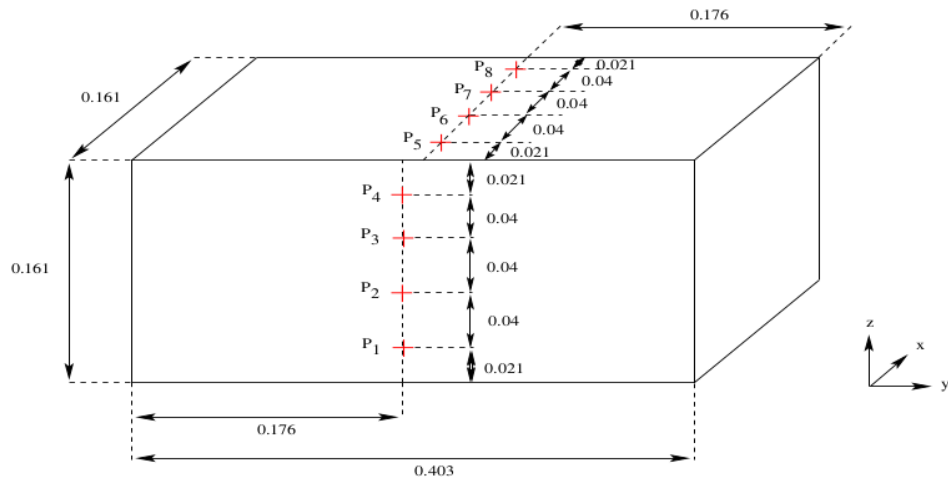
(b) Description of the obstacle.

Figure 6.10 Configuration of the experimental setup for the three-dimensional dam-breaking test case [113].
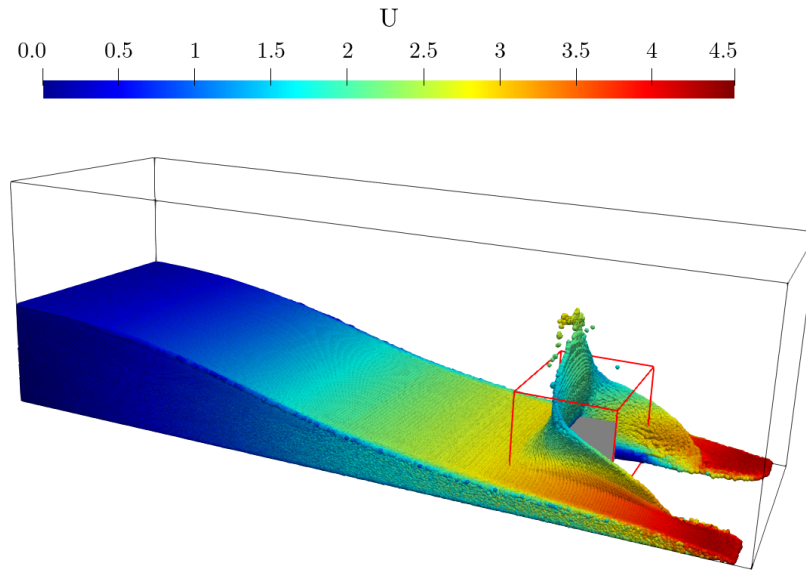
Figure 6.11 Velocity magnitude contours for the three-dimensional dam break using the multi-resolution algorithm. The refinement region is highlighted in red.

predicts the pressure peak. In previous studies [48, 155], the poor agreement at these locations was attributed to the neglection of the air phase. It must be noted, however, that at the pressure probes P4, the results obtained with the present algorithm are improved with respect to previous investigation with the SPH method [75].

The time history of the pressure at the probes placed on the top side of the obstacle is reported in Figure 6.13. At all locations, the SPH simulation is able to predict quite well the rise of the pressure due to the wave impact on the top surface of the obstacle. The high viscosity value herein used is probably responsible for the phase lag at the second impact of the incident wave around $t \approx 5s$ that is present at all gauges locations.

In Figure 6.14 is displayed the wave elevation at the different gauges. The numerical simulation agrees well with the experimental results, in particular at the $H2$ and $H4$ points. At $H1$ and $H3$, despite some differences, the present solution is able to describe the shape of the wave elevation. However, there are some differences, probably due to the more complex shape of the free-surface interface at these locations. It is noticeable, as from the pressure measurement, a phase error
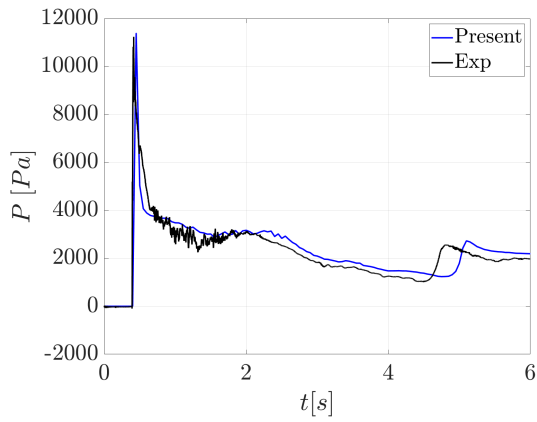
(a) P1
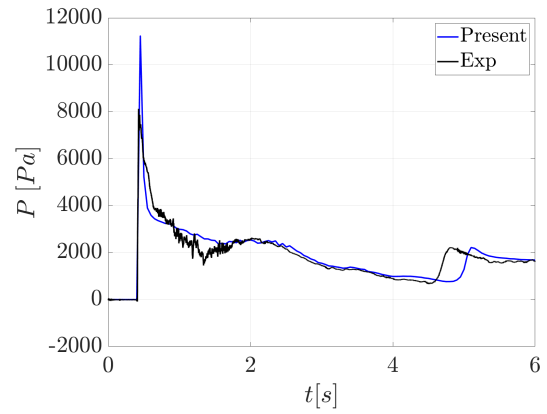
(b) P2
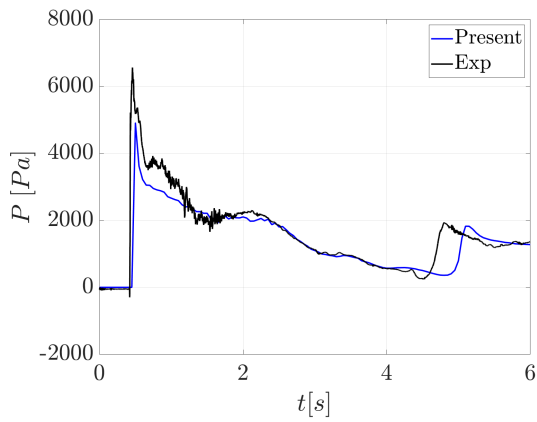
(c) P3
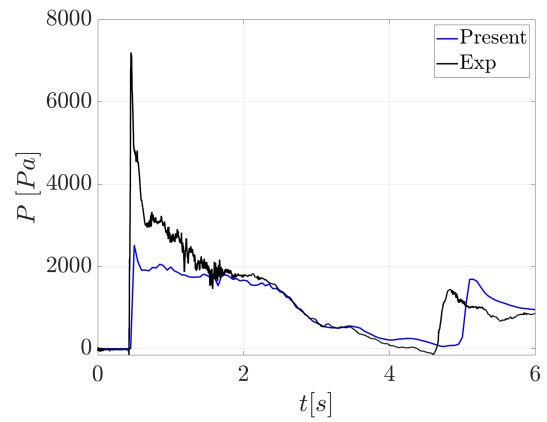
(d) P4

Figure 6.12 Comparison of the time history of the pressure at the front side measurements gauges between the present simulation and the experimental data [113].
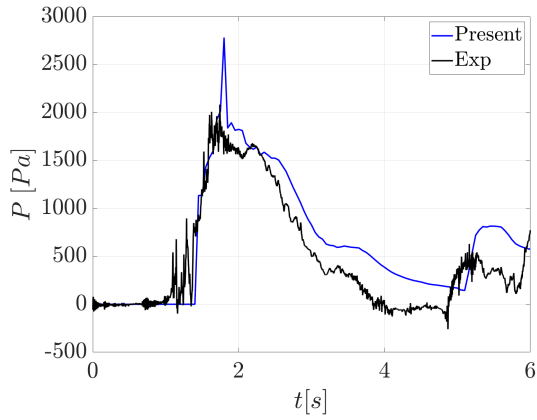
(a) P5
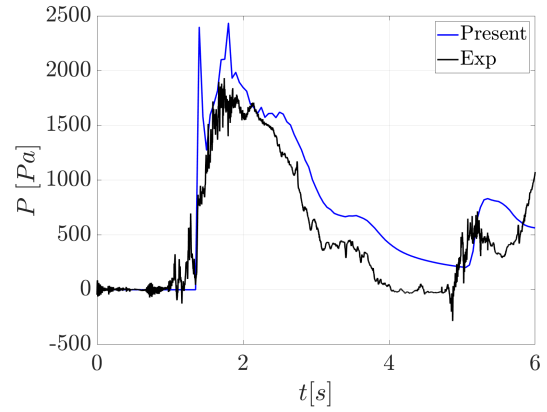
(b) P6
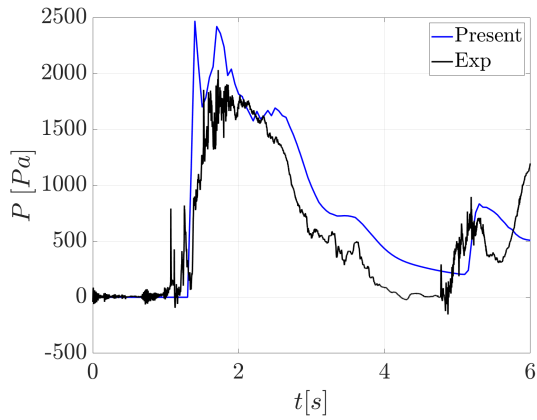
(c) P7
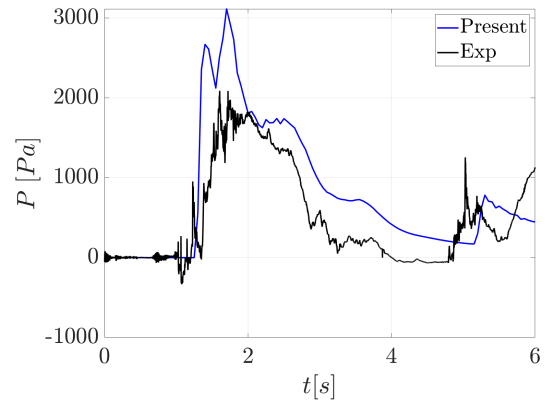
(d) P8

Figure 6.13 Comparison of the time history of the pressure at the top side measurements gauges between the present simulation and the experimental data [113].

(a) $H1$ **(b)** $H2$

(c) $H3$ **(d)** $H4$
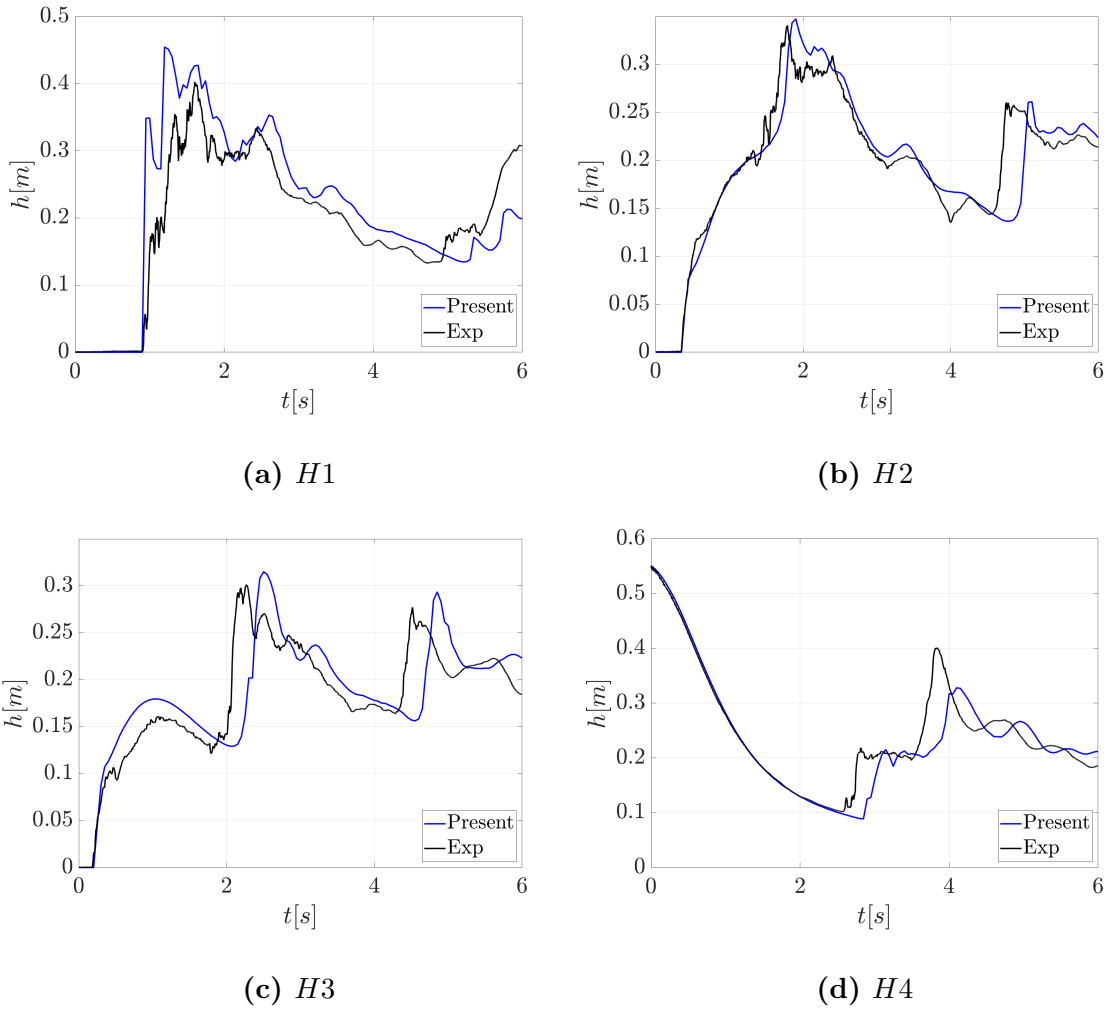
Figure 6.14 Comparison of the time history of the wave elevation at the measurements gauges between the present simulation and the experimental data [113].

occurs when the incident wave is reflected back into the domain due to the high viscosity value herein used. To furtherly illustrate how the multi-resolution algorithm is able to treat the crossing over of the complex free-surface interface across the two sub-domains, in Figure 6.15 the density contours across the center-line section in the longitudinal direction are displayed. As can be seen, following the first impact of the dambreaking flow against the central obstacle [Figure 6.15(a)], a jumping jet develops over the cuboid obstacle [Figure 6.15(b)]. This jet then interact with the flow reflected by the vertical wall of the rectangular tank [Figure 6.15(c)], and complex interfaces

characterized by various fluid jet develops. The present approach is able to model accurately the evolution of this violent flow, and no discontinuity are visible.
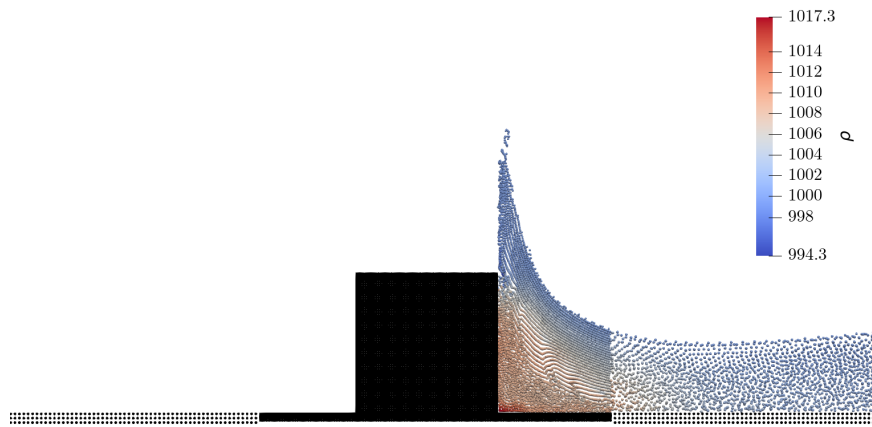
(a) $t = 0.5s$
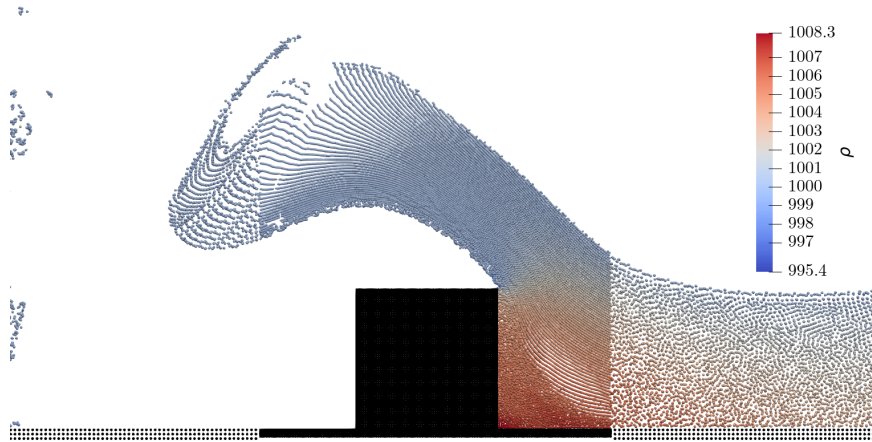
(b) $t = 1s$
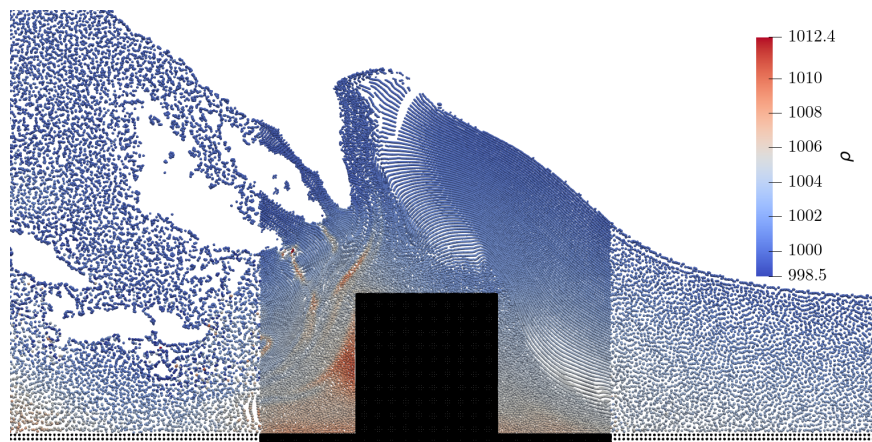
(c) $t = 1.5s$

Figure 6.15 Snapshots of the density [kg/m³] contours across the center-line section in the longitudinal direction during the first impact of dam-breaking flows against the obstacle.

CHAPTER 7

CONCLUSION AND FUTURE WORK

7.1 Conclusion

In this work, significant developments have been proposed for extending the applicability of the SPH method to real engineering problems, with a particular focus on the simulation of turbulent flows.

The first part of this dissertation has focused on investigating isotropic turbulent flows using a direct numerical simulation approach. A decaying isotropic turbulent flow in a triple periodic box has been simulated using different kinematic descriptions of the governing equations. The Eulerian scheme has shown an accurate reproduction of the reference solution, both in terms of energy dissipation rate and energy distribution across the different turbulent scales. On the opposite, the Lagrangian SPH, despite achieving a certain degree of convergence toward the reference solution, suffers from the error introduced by the particle disorder that results in an over-dissipative solution and a spurious flattening at high-frequencies in the turbulent energy spectrum. The inclusion of the density diffusion term proposed in [84] does not prevent the over-diffusion observed in the early part of the flow but seems beneficial when smaller turbulent structures develop. Particularly, this term restores an accurate estimation of the energy dissipation rate and improves the energy distribution across the different turbulent scales. The investigation is then moved to a linearly forced isotropic turbulent case, the density diffusion term by [84] must be introduced in the continuity equation for both Eulerian and Lagrangian SPH to preserve stability. When this term is employed, both schemes are able to achieve a stationary solution, with the value of the ratio between the mean energy dissipation rate and the mean square velocity reaching the prescribed one, indicating

that the density diffusion term does not affect the momentum dissipation. Besides some discrepancies at the high wavenumbers, the energy spectra of the Lagrangian and Eulerian formulations are consistent. This suggests that both schemes are able to produce DNS of fully developed turbulent flows, provided that a correct resolution is adopted and that a density diffusion term is incorporated. Finally, the influence of particle shifting has been evaluated when the magnitude of the forcing term is increased, leading to more critical simulation conditions. The PST has shown a strong regularization of the particle distribution, with an important role of the ALE corrective terms on the correct description of the turbulent scales in the inertial range.

The numerical computation of turbulent flows with Eulerian SPH schemes based on high-order kernels has been investigated for the first time, demonstrating the ability of such scheme to accurately compute, even at moderate resolution, the three-dimensional Taylor-Green vortex case. More precisely, the 4th- and 6th-order schemes, due to their low intrinsic numerical diffusion, are capable of dramatically improving the prediction of the vorticity dynamics with respect to the standard 2nd-order SPH schemes.

In the second part of the dissertation, the scope of this work has been tackled from a different perspective, with the development of a novel multi-resolution SPH approach. The proposed algorithm is based on partitioning the computational domain, defining a different resolution for each sub-domain. Therefore, the computational sub-problems are then closed, extending each sub-domain with buffer regions that act as Dirichlet boundary condition. The enforcement of the boundary conditions at each time step is obtained by assigning the flow variables of buffer particles through a second-order accurate interpolation over the fluid particles of adjacent sub-domains. To model the mass exchange between sub-domains, a procedure based on evaluating the Eulerian mass flux at the interfaces is employed. A special formulation based on a free-surface detection method is adopted for cases where the free surface crosses

the interface between two domains. To avoid pressure discontinuities and to ensure a robust coupling, a regularization procedure based on the Particle Shifting Technique is introduced for the buffer particles.

The proposed algorithm has been implemented in the open-source SPH code DualSPHysics, and has been validated through various two-dimensional test cases: a hydrostatic tank case, the flow past a cylinder from a Reynolds number $Re = 100$ up to $Re = 9500$, a flow past an oscillating cylinder, and the propagation of regular waves in a rectangular domain case. The numerical results have been compared against single-resolution simulation when possible to demonstrate the consistency of the variable-resolution approach, or experimental and numerical results available in literature.

The validation study has demonstrated the ability of the proposed algorithm to maintain the accuracy of the solution while lowering the computational cost with respect to the uniform resolution formulation, up to almost three orders of magnitude in some cases. Moreover, the multi-resolution herein proposed can be used to increase the resolution near moving objects, and can also be applied to free-surface flow.

Then, the validation process has been extended to three-dimensional flows: the flow past a sphere for $Re = 300$ and $Re = 500$ has been simulated using the present variable-resolution approach. The numerical results have been compared against relevant reference data in the literature for the aerodynamical coefficients and the vortex shedding frequencies. Moreover, the SPHERIC benchmark case #2, a dambreaking flow that impacts against a cubic obstacle, is then simulated and validated against the experimental results.

7.2   Future Work

Given the developments presented in this dissertation, there are several areas in which the current research work can progress:

145

- Extension of the numerical study presented in Chapter 4 to turbulent channel flows, poorly addressed in the SPH research community. This study is also encouraged by the development of the proposed variable-resolution algorithm that can be employed to ensure an adequate resolution at the solid boundary.

- The multi-resolution algorithm herein presented, can be also viewed as a general SPH-SPH coupling framework. From that perspective, a future improvement could be the coupling of the Eulerian SPH scheme, applied in the interior region of the flow to exploit its higher order of accuracy, with the Lagrangian SPH formulation that can be employed in areas in which complex moving interface are expected.

- The implementation of the multi-resolution algorithm in the DualSPHysics code presented in this work is susceptible to major improvements in terms of efficiency. One bottleneck is represented from the non-asynchronous computation of the particle interaction between the sub-domains, that can decrease the performance of the code, especially when the size of the particle of one or more sub-domain is not high enough to fully occupy the streaming multiprocessor. A strategy to address this issue could be based on taking advantage of the CUDA stream module.

- Application of the variable-resolution approach to fluid-structure interaction with moving and deformable objects, both with a monolithic or partitioned approach. Another major development is the extension of the approach to multiphase flow.

APPENDIX

In the following appendix, is reported the numerical method that has been employed in order to compute the turbulent energy spectra for the Lagrangian SPH results.

MLS Extrapolation

To extract the turbulent energy spectra, a second order Moving Least-Squares (MLS) interpolation over a uniform grid has been performed following the indications in Shi et al. (2013) [223] and with a resolution equal to the initial particle spacing. Taking the value of a field at a random point as:

$$f_b = f(\mathbf{r}_b), \tag{A.1}$$

where $\mathbf{r}_b$ is the position of particle b in a Cartesian system, and expanding it in Taylor series about particle j, one obtains

$$f_b = f_a + \sum_{n=1}^{+\infty} \frac{\partial^n f_a}{n!}(\mathbf{r}_b - \mathbf{r}_b)^n. \tag{A.2}$$

The value of f_b is approximated via a MLS interpolation using a polynomial of order β, thus leading to:

$$f_b^+ = f_a + \sum_{n=1}^{\beta} \frac{\partial^n f_a}{n!}(\mathbf{r}_b - \mathbf{r}_a)^n. \tag{A.3}$$

The error at the position i is then expressed as:

$$E_a = \sum_{b=1}^{N} L_{ab}[f_b^+ - f_a]^2, \tag{A.4}$$

where L_{ab} weighs the contribution of different particles, and can be employed as an SPH interpolator defined as:

$$L_{ab} = \Phi_a \mathbf{W}_{ab}. \tag{A.5}$$

Within a least-squares procedure, when minimizing the error with respect to f_a and its derivatives, one obtains a $p \times p$ set of equations, where p depends on the dimensionality of the problem and on the order β of the approximation chosen. For a second order 3D MLS interpolator, one obtains the following system:

$$R_{IJ} F_J = T_I \quad \text{for } I, J = 1, 2, \ldots, p, \tag{A.6}$$

where

$$R_{IJ} = \sum_{b=1}^{N} \Phi_b W_{ab} \cdot \Lambda(I)\Theta(J),$$

$$\Theta = [1.0, x_{ab}, y_{ab}, z_{ab}, x_{ab}^2, x_{ab}y_{ab}, y_{ab}^2, z_{ab}z_{ab}, z_{ab}^2, y_{ab}z_{ab}],$$

$$\Lambda = [1.0, x_{ab}, y_{ab}, z_{ab}, x_{ab}^2, x_{ab}y_{ab}, y_{ab}^2, z_{ab}z_{ab}, z_{ab}^2, y_{ab}z_{ab}],$$

$$F_J = [f_a, \partial^x f_a, \partial^y f_a, \partial^z f_a, \partial_2^x f_a, \partial^x \partial^y f_a, \partial_2^y f_a, \partial^x \partial^z f_a, \partial_2^z f_a, \partial^z f_a, \partial^y f_a],$$

$$T_I = \sum_{n=1}^{N} \Phi_b W_{ab} \cdot \Lambda(I).$$

REFERENCES

[1] S. Adami, X. Y. Hu, and N. A. Adams. A generalized wall boundary condition for smoothed particle hydrodynamics. *Journal of Computational Physics*, 231(21):7057–7075, 2012.

[2] C. Altomare, A. J. Crespo, J. M. Domínguez, M. Gómez-Gesteira, T. Suzuki, and T. Verwaest. Applicability of smoothed particle hydrodynamics for estimation of sea wave impact on coastal structures. *Coastal Engineering*, 96:1–12, 2015.

[3] C. Altomare, A. J. Crespo, B. Rogers, J. Dominguez, X. Gironella, and M. Gómez-Gesteira. Numerical modelling of armour block sea breakwater with smoothed particle hydrodynamics. *Computers and Structures*, 130:34–45, 2014.

[4] C. Altomare, A. Tafuni, J. M. Domínguez, A. J. Crespo, X. Gironella, and J. Sospedra. Sph simulations of real sea waves impacting a large-scale structure. *Journal of Marine Science and Engineering*, 8(10):826, 2020.

[5] P. Anagnostopoulos and P. Bearman. Response characteristics of a vortex-excited cylinder at low reynolds numbers. *Journal of Fluids and Structures*, 6(1):39–50, 1992.

[6] C. Antoci, M. Gallati, and S. Sibilla. Numerical simulation of fluid–structure interaction by sph. *Computers and Structures*, 85(11-14):879–890, 2007.

[7] R. Antona, R. Vacondio, D. Avesani, M. Righetti, and M. Renzi. Towards a high order convergent ale-sph scheme with efficient weno spatial reconstruction. *Water*, 13(17):2432, 2021.

[8] M. Antuono, A. Colagrossi, S. Marrone, and D. Molteni. Free-surface flows solved by means of SPH schemes with numerical diffusive terms. *Computer Physics Communications*, 181(3):532–549, 2010.

[9] M. Antuono, S. Marrone, A. Di Mascio, and A. Colagrossi. Smoothed particle hydrodynamics method from a large eddy simulation perspective. generalization to a quasi-lagrangian model. *Physics of Fluids*, 33(1):015102, 2021.

[10] M. Antuono, P. Sun, S. Marrone, and A. Colagrossi. The δ-ale-sph model: An arbitrary lagrangian-eulerian framework for the δ-sph model with particle shifting technique. *Computers and Fluids*, 216:104806, 2021.

[11] P. Artymowicz and S. H. Lubow. Dynamics of binary-disk interaction. 1: Resonances and disk gap sizes. *The Astrophysical Journal*, 421:651–667, 1994.

[12] S. N. Atluri and T. Zhu. A new meshless local petrov-galerkin (mlpg) approach in computational mechanics. *Computational Mechanics*, 22(2):117–127, 1998.

[13] D. Avesani, M. Dumbser, and A. Bellin. A new class of moving-least-squares weno–sph schemes. *Journal of Computational Physics*, 270:278–299, 2014.

[14] D. Avesani, M. Dumbser, R. Vacondio, and M. Righetti. An alternative sph formulation: Ader-weno-sph. *Computer Methods in Applied Mechanics and Engineering*, 382:113871, 2021.

[15] D. A. Barcarolo, D. Le Touzé, G. Oger, and F. De Vuyst. Adaptive particle refinement and derefinement applied to the smoothed particle hydrodynamics method. *Journal of Computational Physics*, 273:640–657, 2014.

[16] R. Batra and G. Zhang. Analysis of adiabatic shear bands in elasto-thermo-viscoplastic materials by modified smoothed-particle hydrodynamics (msph) method. *Journal of Computational Physics*, 201(1):172–190, 2004.

[17] R. Batra and G. Zhang. Search algorithm, and simulation of elastodynamic crack propagation by modified smoothed particle hydrodynamics (msph) method. *Computational Mechanics*, 40:531–546, 2007.

[18] T. Belytschko, Y. Guo, W. Kam Liu, and S. Ping Xiao. A unified stability analysis of meshless particle methods. *International Journal for Numerical Methods in Engineering*, 48(9):1359–1400, 2000.

[19] T. Belytschko, Y. Y. Lu, and L. Gu. Element-free galerkin methods. *International Journal for Numerical Methods in Fluids*, 37(2):229–256, 1994.

[20] X. Bian, Z. Li, and G. E. Karniadakis. Multi-resolution flow simulations by smoothed particle hydrodynamics via domain decomposition. *Journal of Computational Physics*, 297:132–155, 2015.

[21] G. Bilotta, A. Hérault, A. Cappello, G. Ganci, and C. Del Negro. Gpusph: a smoothed particle hydrodynamics model for the thermal and rheological evolution of lava flows. *Geological Society, London, Special Publications*, 426(1):387–408, 2016.

[22] G. Boffetta and R. E. Ecke. Two-dimensional turbulence. *Annual Review of Fluid Mechanics*, 44:427–451, 2012.

[23] J. Bonet and T.-S. Lok. Variational and momentum preservation aspects of smooth particle hydrodynamic formulations. *Computer Methods in Applied Mechanics and Engineering*, 180(1-2):97–115, 1999.

[24] J. Bonet and M. X. Rodríguez-Paz. Hamiltonian formulation of the variable-h sph equations. *Journal of Computational Physics*, 209(2):541–558, 2005.

[25] I. Borazjani, L. Ge, and F. Sotiropoulos. Curvilinear immersed boundary method for simulating fluid structure interaction with complex 3d rigid bodies. *Journal of Computational Physics*, 227(16):7587–7620, 2008.

[26] S. Børve, M. Omang, and J. Trulsen. Regularized smoothed particle hydrodynamics with improved multi-resolution handling. *Journal of Computational Physics*, 208(1):345–367, 2005.

[27] R. Bouard and M. Coutanceau. The early stage of development of the wake behind an impulsively started cylinder for 40¡ re¡ 104. *Journal of Fluid Mechanics*, 101(3):583–607, 1980.

[28] M. E. Brachet, D. I. Meiron, S. A. Orszag, B. Nickel, R. H. Morf, and U. Frisch. Small-scale structure of the taylor–green vortex. *Journal of Fluid Mechanics*, 130:411–452, 1983.

[29] M. Brito, R. Canelas, O. García-Feal, J. Domínguez, A. Crespo, R. Ferreira, M. Neves, and L. Teixeira. A numerical tool for modelling oscillating wave surge converter with nonlinear mechanical constraints. *Renewable Energy*, 146:2024–2043, 2020.

[30] R. B. Canelas, A. J. Crespo, J. M. Domínguez, R. M. Ferreira, and M. Gómez-Gesteira. Sph–dcdem model for arbitrary geometries in free surface solid–fluid flows. *Computer Physics Communications*, 202:131–140, 2016.

[31] X. Cao, F. Ming, and A. Zhang. Sloshing in a rectangular tank based on sph simulation. *Applied Ocean Research*, 47:241–254, 2014.

[32] J. Carberry, J. Sheridan, and D. Rockwell. Forces and wake modes of an oscillating cylinder. *Journal of Fluids and Structures*, 15(3-4):523–532, 2001.

[33] J. Carberry, J. Sheridan, and D. Rockwell. Controlled oscillations of a cylinder: forces and wake modes. *Journal of Fluid Mechanics*, 538:31–69, 2005.

[34] J. L. Cercos-Pita. Aquagpusph, a new free 3d sph solver accelerated with opencl. *Computer Physics Communications*, 192:295–312, 2015.

[35] J. Chanéac, P. Duquesne, S. Aubert, and J.-C. Marongiu. Improvements of the refinement pattern of Adaptive Particle Refinement. In *15th International SPHERIC Workshop*, SPHERIC 2021 International Workshop Proceedings, Newark, United States, June 2021.

[36] J. Chen and J. Beraun. A generalized smoothed particle hydrodynamics method for nonlinear dynamic problems. *Computer Methods in Applied Mechanics and Engineering*, 190(1-2):225–239, 2000.

[37] L. Chiron, G. Oger, M. De Leffe, and D. Le Touzé. Analysis and improvements of adaptive particle refinement (apr) through cpu time, accuracy and robustness considerations. *Journal of Computational Physics*, 354:552–575, 2018.

[38] H. Choi and P. Moin. Grid-point requirements for large eddy simulation: Chapman's estimates revisited. *Physics of Fluids*, 24(1):011702, 2012.

[39] Y. Chuzel-Marmot, R. Ortiz, and A. Combescure. Three dimensional sph–fem gluing for simulation of fast impacts on concrete slabs. *Computers and Structures*, 89(23-24):2484–2494, 2011.

[40] P. W. Cleary. Modelling confined multi-material heat and mass flows using sph. *Applied Mathematical Modelling*, 22(12):981–993, 1998.

[41] P. W. Cleary and J. J. Monaghan. Conduction modelling using smoothed particle hydrodynamics. *Journal of Computational Physics*, 148(1):227–264, 1999.

[42] A. Colagrossi, M. Antuono, and D. Le Touzé. Theoretical considerations on the free-surface role in the smoothed-particle-hydrodynamics model. *Physical Review E*, 79(5):056701, 2009.

[43] A. Colagrossi, M. Antuono, A. Souto-Iglesias, and D. Le Touzé. Theoretical analysis and numerical verification of the consistency of viscous smoothed-particle-hydrodynamics formulations in simulating free-surface flows. *Physical Review E*, 84(2):026705, 2011.

[44] A. Colagrossi, B. Bouscasse, M. Antuono, and S. Marrone. Particle packing algorithm for SPH schemes. *Computer Physics Communications*, 183(8):1641–1653, 2012.

[45] A. Colagrossi and M. Landrini. Numerical simulation of interfacial flows by smoothed particle hydrodynamics. *Journal of Computational Physics*, 191(2):448–475, 2003.

[46] G. Constantinescu and K. Squires. Les and des investigations of turbulent flow over a sphere. In *38th Aerospace Sciences Meeting and Exhibit*, page 540, 2000.

[47] A. Crespo, C. Altomare, J. Domínguez, J. González-Cao, and M. Gómez-Gesteira. Towards simulating floating offshore oscillating water column converters with smoothed particle hydrodynamics. *Coastal Engineering*, 126:11–26, 2017.

[48] A. C. Crespo, J. M. Dominguez, A. Barreiro, M. Gómez-Gesteira, and B. D. Rogers. Gpus, a new tool of acceleration in cfd: efficiency and reliability on smoothed particle hydrodynamics methods. *PloS one*, 6(6):e20685, 2011.

[49] A. J. Crespo, J. M. Domínguez, B. D. Rogers, M. Gómez-Gesteira, S. Longshaw, R. Canelas, R. Vacondio, A. Barreiro, and O. García-Feal. Dualsphysics: Open-source parallel cfd solver based on smoothed particle hydrodynamics (sph). *Computer Physics Communications*, 187:204–216, 2015.

[50] A. J. Crespo, M. Gómez-Gesteira, and R. A. Dalrymple. Boundary conditions generated by dynamic particles in sph methods. *Computers, Materials and Continua*, 5(3):173–184, 2007.

[51] A. Crivellini, V. D'Alessandro, and F. Bassi. Assessment of a high-order discontinuous galerkin method for incompressible three-dimensional navier–stokes equations: Benchmark results for the flow past a sphere up to re= 500. *Computers and Fluids*, 86:442–458, 2013.

[52] S. J. Cummins and M. Rudman. An sph projection method. *Journal of Computational Physics*, 152(2):584–607, 1999.

[53] R. Dalrymple and O. Knio. Sph modelling of water waves. In *Coastal Dynamics 2001*, Coastal Dynamics 2001, pages 779–787, United States, 2001. American Society of Civil Engineers (ASCE).

[54] R. A. Dalrymple and B. D. Rogers. Numerical modeling of water waves with the SPH method. *Coastal Engineering*, 2006.

[55] W. Dehnen and H. Aly. Improving convergence in smoothed particle hydrodynamics simulations without pairing instability. *Monthly Notices of the Royal Astronomical Society*, 425(2):1068–1082, 2012.

[56] L. Delorme, A. Colagrossi, A. Souto-Iglesias, R. Zamora-Rodriguez, and E. Botia-Vera. A set of canonical problems in sloshing, part i: Pressure field in forced roll—comparison between experimental results and sph. *Ocean Engineering*, 36(2):168–178, 2009.

[57] A. Di Mascio, M. Antuono, A. Colagrossi, and S. Marrone. Smoothed particle hydrodynamics method from a large eddy simulation perspective. *Physics of Fluids*, 29(3):035102, mar 2017.

[58] G. A. Dilts. Moving-least-squares-particle hydrodynamics—i. consistency and stability. *International Journal for Numerical Methods in Engineering*, 44(8):1115–1155, 1999.

[59] J. Domínguez, A. Crespo, M. Gómez-Gesteira, and J. Marongiu. Neighbour lists in smoothed particle hydrodynamics. *International Journal for Numerical Methods in Fluids*, 67(12):2026–2042, 2011.

[60] J. Domínguez, G. Fourtakas, J. Cercos-Pita, R. Vacondio, B. Rogers, and A. Crespo. Evaluation of reliability and efficiency of different boundary conditions in a sph code. 2015. 10th International SPHERIC Workshop ; Conference date: 09-06-2015.

[61] J. M. Domínguez, A. J. Crespo, and M. Gómez-Gesteira. Optimization strategies for cpu and gpu implementations of a smoothed particle hydrodynamics method. *Computer Physics Communications*, 184(3):617–627, 2013.

[62] J. M. Domínguez, G. Fourtakas, C. Altomare, R. B. Canelas, A. Tafuni, O. García-Feal, I. Martínez-Estévez, A. Mokos, R. Vacondio, A. J. Crespo, et al. Dualsphysics: from fluid dynamics to multiphysics problems. *Computational Particle Mechanics*, pages 1–29, 2021.

[63] J. Domínguez, A. Crespo, D. Valdez-Balderas, B. Rogers, and M. Gómez-Gesteira. New multi-gpu implementation for smoothed particle hydrodynamics on heterogeneous clusters. *Computer Physics Communications*, 184(8):1848–1860, 2013.

[64] J. Donea, A. Huerta, J.-P. Ponthot, and A. Rodríguez-Ferran. Arbitrary lagrangian–eulerian methods. *Encyclopedia of Computational Mechanics*, 2004.

[65] D. Drikakis, C. Fureby, F. F. Grinstein, and D. Youngs. Simulation of transition and turbulence decay in the taylor–green vortex. *Journal of Turbulence*, (8):N20, 2007.

[66] A. English, J. Domínguez, R. Vacondio, A. Crespo, P. Stansby, S. Lind, L. Chiapponi, and M. Gómez-Gesteira. Modified dynamic boundary conditions (mdbc) for general-purpose smoothed particle hydrodynamics (sph): Application to tank sloshing, dam break and fish pass problems. *Computational Particle Mechanics*, 9(5):1–15, 2022.

[67] P. Espanol and M. Revenga. Smoothed dissipative particle dynamics. *Physical Review E*, 67(2):026705, 2003.

[68] R. Fatehi and M. Manzari. A remedy for numerical oscillations in weakly compressible smoothed particle hydrodynamics. *International Journal for Numerical Methods in Fluids*, 67(9):1100–1114, 2011.

[69] I. Federico, S. Marrone, A. Colagrossi, F. Aristodemo, and M. Antuono. Simulating 2d open-channel flows through an sph model. *European Journal of Mechanics-B/Fluids*, 34:35–46, 2012.

[70] J. Feldman and J. Bonet. Dynamic refinement and boundary contact forces in sph with applications in fluid flow problems. *International Journal for Numerical Methods in Engineering*, 72(3):295–324, 2007.

[71] M. Ferrand, D. Laurence, B. D. Rogers, D. Violeau, and C. Kassiotis. Unified semi-analytical wall boundary conditions for inviscid, laminar or turbulent flows in the meshless sph method. *International Journal for Numerical Methods in Fluids*, 71(4):446–472, 2013.

[72] A. Ferrari, M. Dumbser, E. F. Toro, and A. Armanini. A new 3d parallel sph scheme for free surface flows. *Computers and Fluids*, 38(6):1203–1217, 2009.

[73] J. H. Ferziger, M. Perić, and R. L. Street. *Computational Methods for Fluid Dynamics*, volume 3. Springer, 2002.

[74] G. Fourey, C. Hermange, D. Le Touzé, and G. Oger. An efficient fsi coupling strategy between smoothed particle hydrodynamics and finite element methods. *Computer Physics Communications*, 217:66–81, 2017.

[75] G. Fourtakas, J. M. Dominguez, R. Vacondio, and B. D. Rogers. Local uniform stencil (lust) boundary condition for arbitrary 3-d boundaries in parallel smoothed particle hydrodynamics (sph) models. *Computers and Fluids*, 190:346–361, 2019.

[76] G. Fourtakas, R. Vacondio, and B. D. Rogers. On the approximate zeroth and first-order consistency in the presence of 2-d irregular boundaries in sph obtained by the virtual boundary particle methods. *International Journal for Numerical Methods in Fluids*, 78(8):475–501, 2015.

[77] G. C. Ganzenmüller. An hourglass control algorithm for lagrangian smooth particle hydrodynamics. *Computer Methods in Applied Mechanics and Engineering*, 286:87–106, 2015.

[78] T. Gao, H. Qiu, and L. Fu. A block-based adaptive particle refinement sph method for fluid–structure interaction problems. *Computer Methods in Applied Mechanics and Engineering*, 399:115356, 2022.

[79] M. Germano, U. Piomelli, P. Moin, and W. H. Cabot. A dynamic subgrid-scale eddy viscosity model. *Physics of Fluids A: Fluid Dynamics*, 3(7):1760–1765, 1991.

[80] R. A. Gingold and J. J. Monaghan. Smoothed particle hydrodynamics: theory and application to non-spherical stars. *Monthly Notices of the Royal Astronomical Society*, 181(3):375–389, 1977.

[81] M. Gomez-Gesteira, B. D. Rogers, A. J. Crespo, R. A. Dalrymple, M. Narayanaswamy, and J. M. Dominguez. Sphysics–development of a free-surface fluid solver–part 1: Theory and formulations. *Computers and Geosciences*, 48:289–299, 2012.

[82] J. González-Cao, C. Altomare, A. J. Crespo, J. Domínguez, M. Gómez-Gesteira, and D. Kisacik. On the accuracy of dualsphysics to assess violent collisions with coastal structures. *Computers and Fluids*, 179:604–612, 2019.

[83] M. D. Green and J. Peiró. Long duration sph simulations of sloshing in tanks with a low fill ratio and high stretching. *Computers and Fluids*, 174:179–199, 2018.

[84] M. D. Green, R. Vacondio, and J. Peiró. A smoothed particle hydrodynamics numerical scheme with a consistent diffusion term for the continuity equation. *Computers and Fluids*, 2019.

[85] M. D. Green, R. Vacondio, and J. Peiró. A smoothed particle hydrodynamics numerical scheme with a consistent diffusion term for the continuity equation. *Computers and Fluids*, 179:632–644, 2019.

[86] M. D. Green, Y. Zhou, J. M. Dominguez, M. G. Gesteira, and J. Peiró. Smooth particle hydrodynamics simulations of long-duration violent three-dimensional sloshing in tanks. *Ocean Engineering*, 229:108925, 2021.

[87] B. E. Griffith and N. A. Patankar. Immersed methods for fluid–structure interaction. *Annual Review of Fluid Mechanics*, 52:421–448, 2020.

[88] J. Guerrero, E. García-Berro, and J. Isern. Smoothed particle hydrodynamics simulations of merging white dwarfs. *Astronomy and Astrophysics*, 413(1):257–272, 2004.

[89] A. Haftu, A. Muta, and P. Ramachandran. Parallel adaptive weakly-compressible sph for complex moving geometries. *Computer Physics Communications*, 277:108377, 2022.

[90] I. Hammani, S. Marrone, A. Colagrossi, G. Oger, and D. Le Touzé. Detailed study on the extension of the δ-sph model to multi-phase flow. *Computer Methods in Applied Mechanics and Engineering*, 368:113189, 2020.

[91] L. Hernquist and N. Katz. Treesph-a unification of sph with the hierarchical tree method. *Astrophysical Journal Supplement Series (ISSN 0067-0049), vol. 70, June 1989, p. 419-446. Research supported by the San Diego Supercomputer Center, Pittsburgh Supercomputer Center, and New Jersey High Technology Grant.*, 70:419–446, 1989.

[92] C. Hirsch. *Numerical computation of internal and external flows: The fundamentals of computational fluid dynamics.* Elsevier, 2007.

[93] C. W. Hirt, A. A. Amsden, and J. Cook. An arbitrary lagrangian-eulerian computing method for all flow speeds. *Journal of Computational Physics*, 14(3):227–253, 1974.

[94] C. W. Hirt and B. D. Nichols. Volume of fluid (vof) method for the dynamics of free boundaries. *Journal of Computational Physics*, 39(1):201–225, 1981.

[95] D. D. Holm. Fluctuation effects on 3d lagrangian mean and eulerian mean fluid motion. *Physica D: Nonlinear Phenomena*, 133(1-4):215–269, 1999.

[96] M.-C. Hsu, D. Kamensky, Y. Bazilevs, M. S. Sacks, and T. J. Hughes. Fluid–structure interaction analysis of bioprosthetic heart valves: significance of arterial wall deformation. *Computational Mechanics*, 54:1055–1071, 2014.

[97] X. Hu and N. A. Adams. An incompressible multi-phase sph method. *Journal of Computational Physics*, 227(1):264–278, 2007.

[98] S. Inutsuka. Godunov-type sph. *Memorie della Societa Astronomica Italiana*, 65:1027, 1994.

[99] K. Iwasaki and S.-i. Inutsuka. Smoothed particle magnetohydrodynamics with a riemann solver and the method of characteristics. *Monthly Notices of the Royal Astronomical Society*, 418(3):1668–1688, 2011.

[100] J. Jiménez. Near-wall turbulence. *Physics of Fluids*, 25(10):101302, 2013.

[101] G. R. Johnson, R. A. Stryk, and S. R. Beissel. Sph for high velocity impact computations. *Computer Methods in Applied Mechanics and Engineering*, 139(1-4):347–373, 1996.

[102] T. Johnson and V. Patel. Flow past a sphere up to a reynolds number of 300. *Journal of Fluid Mechanics*, 378:19–70, 1999.

[103] W. P. Jones and B. E. Launder. The prediction of laminarization with a two-equation model of turbulence. *International Journal of Heat and Mass Transfer*, 15(2):301–314, 1972.

[104] R. Kamakoti and W. Shyy. Fluid–structure interaction for aeroelastic applications. *Progress in Aerospace Sciences*, 40(8):535–558, 2004.

[105] E. Kazemi, K. Koll, S. Tait, and S. Shao. Sph modelling of turbulent open channel flow over and within natural gravel beds with rough interfacial boundaries. *Advances in Water Resources*, 140:103557, 2020.

[106] A. Khayyer and H. Gotoh. Wave impact pressure calculations by improved sph methods. *International Journal of Offshore and Polar Engineering*, 19(04), 2009.

[107] A. Khayyer, H. Gotoh, and S. Shao. Corrected incompressible sph method for accurate water-surface tracking in breaking waves. *Coastal Engineering*, 55(3):236–250, 2008.

[108] A. Khayyer, H. Gotoh, and S. Shao. Enhanced predictions of wave impact pressure by improved incompressible sph methods. *Applied Ocean Research*, 31(2):111–131, 2009.

[109] A. Khayyer, H. Gotoh, and Y. Shimizu. Comparative study on accuracy and conservation properties of two particle regularization schemes and proposal of an optimized particle shifting scheme in isph context. *Journal of Computational Physics*, 332:236–256, 2017.

[110] A. Khayyer, Y. Shimizu, H. Gotoh, and S. Hattori. Multi-resolution isph-sph for accurate and efficient simulation of hydroelastic fluid-structure interactions in ocean engineering. *Ocean Engineering*, 226:108652, 2021.

[111] A. Khayyer, Y. Shimizu, H. Gotoh, and K. Nagashima. A coupled incompressible sph-hamiltonian sph solver for hydroelastic fsi corresponding to composite structures. *Applied Mathematical Modelling*, 94:242–271, 2021.

[112] A. Kiara, K. Hendrickson, and D. K. Yue. Sph for incompressible free-surface flows. part i: error analysis of the basic assumptions. *Computers and Fluids*, 86:611–624, 2013.

[113] K. Kleefsman, G. Fekken, A. Veldman, B. Iwanowski, and B. Buchner. A volume-of-fluid based simulation method for wave impact problems. *Journal of Computational Physics*, 206(1):363–393, 2005.

[114] A. N. Kolmogorov. A refinement of previous hypotheses concerning the local structure of turbulence in a viscous incompressible fluid at high reynolds number. *Journal of Fluid Mechanics*, 13(1):82–85, 1962.

[115] A. N. Kolmogorov. The local structure of turbulence in incompressible viscous fluid for very large reynolds numbers. *Proceedings of the Royal Society of London. Series A: Mathematical and Physical Sciences*, 434(1890):9–13, 1991.

[116] S. Koshizuka and Y. Oka. Moving-particle semi-implicit method for fragmentation of incompressible fluid. *Nuclear Science and Engineering*, 123(3):421–434, 1996.

[117] P. K. Koukouvinis, J. S. Anagnostopoulos, and D. E. Papantonis. An improved muscl treatment for the sph-ale method: comparison with the standard sph method for the jet impingement case. *International Journal for Numerical Methods in Fluids*, 71(9):1152–1177, 2013.

[118] P. Koumoutsakos and A. Leonard. High-resolution simulations of the flow around an impulsively started cylinder using vortex methods. *Journal of Fluid Mechanics*, 296:1–38, 1995.

[119] R. H. Kraichnan and D. Montgomery. Two-dimensional turbulence. *Reports on Progress in Physics*, 43(5):547, 1980.

[120] A. Krimi, M. Jandaghian, and A. Shakibaeinia. A wcsph particle shifting strategy for simulating violent free surface flows. *Water*, 12(11):3189, 2020.

[121] S. Kulasegaram, J. Bonet, R. Lewis, and M. Profit. A variational formulation based contact algorithm for rigid boundaries in two-dimensional sph applications. *Computational Mechanics*, 33:316–325, 2004.

[122] M. Lastiwka, M. Basa, and N. J. Quinlan. Permeable and non-reflecting boundary conditions in sph. *International Journal for Numerical Methods in Fluids*, 61(7):709–724, 2009.

[123] B. E. Launder and B. I. Sharma. Application of the energy-dissipation model of turbulence to the calculation of flow near a spinning disc. *Letters in Heat and Mass Transfer*, 1(2):131–137, 1974.

[124] P. Le Tallec and J. Mouro. Fluid structure interaction with large structural displacements. *Computer Methods in Applied Mechanics and Engineering*, 190(24-25):3039–3067, 2001.

[125] E.-S. Lee, C. Moulinec, R. Xu, D. Violeau, D. Laurence, and P. Stansby. Comparisons of weakly compressible and truly incompressible algorithms for the sph mesh free particle method. *Journal of Computational Physics*, 227(18):8417–8436, 2008.

[126] S. Lee. A numerical study of the unsteady wake behind a sphere in a uniform flow at moderate reynolds numbers. *Computers and Fluids*, 29(6):639–667, 2000.

[127] B. J. Leimkuhler, S. Reich, and R. D. Skeel. Integration methods for molecular dynamics. In *Mathematical Approaches to Biomolecular Structure and Dynamics*, pages 161–185. Springer, 1996.

[128] A. Leroy, D. Violeau, M. Ferrand, and C. Kassiotis. Unified semi-analytical wall boundary conditions applied to 2-d incompressible sph. *Journal of Computational Physics*, 261:106–129, 2014.

[129] R. J. LeVeque. *Finite volume methods for hyperbolic problems*, volume 31. Cambridge university press, Cambridge, UK, 2002.

[130] Z. Li, J. Leduc, A. Combescure, and F. Leboeuf. Coupling of sph-ale method and finite element method for transient fluid–structure interaction. *Computers and Fluids*, 103:6–17, 2014.

[131] D. K. Lilly. A proposed modification of the germano subgrid-scale closure method. *Physics of Fluids A: Fluid Dynamics*, 4(3):633–635, 1992.

[132] S. Lind, P. Stansby, B. Rogers, and P. Lloyd. Numerical predictions of water–air wave slam using incompressible–compressible smoothed particle hydrodynamics. *Applied Ocean Research*, 49:57–71, 2015.

[133] S. Lind, P. Stansby, and B. D. Rogers. Fixed and moored bodies in steep and breaking waves using sph with the froude–krylov approximation. *Journal of Ocean Engineering and Marine Energy*, 2:331–354, 2016.

[134] S. Lind, R. Xu, P. Stansby, and B. Rogers. Incompressible smoothed particle hydrodynamics for free-surface flows: A generalised diffusion-based algorithm for stability and validations for impulsive flows and propagating waves. *Journal of Computational Physics*, 231(4):1499–1523, 2012.

[135] S. J. Lind and P. Stansby. High-order eulerian incompressible smoothed particle hydrodynamics with transition to lagrangian free-surface motion. *Journal of Computational Physics*, 326:290–311, 2016.

[136] S. J. Lind, R. Xu, P. K. Stansby, and B. D. Rogers. Incompressible smoothed particle hydrodynamics for free-surface flows: A generalised diffusion-based algorithm for stability and validations for impulsive flows and propagating waves. *Journal of Computational Physics*, 231(4):1499–1523, 2012.

[137] C. Liu, X. Zheng, and C. Sung. Preconditioned multigrid methods for unsteady incompressible flows. *Journal of Computational Physics*, 139(1):35–57, 1998.

[138] G.-R. Liu and M. B. Liu. *Smoothed particle hydrodynamics: a meshfree particle method*. World scientific, 2003.

[139] M. Liu and G. Liu. Restoring particle consistency in smoothed particle hydrody-
namics. *Applied Numerical Mathematics*, 56(1):19–36, 2006.

[140] M. Liu and G.-R. Liu. Restoring particle consistency in smoothed particle hydrody-
namics. *Applied Numerical Mathematics*, 56(1):19–36, 2006.

[141] M. Liu and Z. Zhang. Smoothed particle hydrodynamics (sph) for modeling fluid-
structure interactions. *Science China Physics, Mechanics and Astronomy*,
62:1–38, 2019.

[142] E. Lo and S. Shao. Simulation of near-shore solitary wave mechanics by an
incompressible SPH method. *Applied Ocean Research*, 2002.

[143] L. B. Lucy. A numerical approach to the testing of the fission hypothesis. *Astronomical
Journal, vol. 82, Dec. 1977, p. 1013-1024.*, 82:1013–1024, 1977.

[144] M. Luo, A. Khayyer, and P. Lin. Particle methods in ocean and coastal engineering.
Applied Ocean Research, 114:102734, 2021.

[145] H.-G. Lyu and P.-N. Sun. Further enhancement of the particle shifting
technique: Towards better volume conservation and particle distribution in
sph simulations of violent free-surface flows. *Applied Mathematical Modelling*,
101:214–238, 2022.

[146] S. Ma, X. Zhang, and X. Qiu. Comparison study of mpm and sph in modeling
hypervelocity impact problems. *International Journal of Impact Engineering*,
36(2):272–282, 2009.

[147] R. Magarvey and R. L. Bishop. Wakes in liquid-liquid systems. *The Physics of Fluids*,
4(7):800–805, 1961.

[148] J. Marongiu, F. Leboeuf, and E. Parkinson. Numerical simulation of the flow in a
pelton turbine using the meshless method smoothed particle hydrodynamics:
a new simple solid boundary treatment. *Proceedings of the Institution of
Mechanical Engineers, Part A: Journal of Power and Energy*, 221(6):849–856,
2007.

[149] S. Marrone, M. Antuono, A. Colagrossi, G. Colicchio, D. Le Touzé, and G. Graziani.
δ-sph model for simulating violent impact flows. *Computer Methods in Applied
Mechanics and Engineering*, 200(13-16):1526–1542, 2011.

[150] S. Marrone, A. Colagrossi, M. Antuono, G. Colicchio, and G. Graziani. An accurate
sph modeling of viscous flows around bodies at low and moderate reynolds
numbers. *Journal of Computational Physics*, 245:456–475, 2013.

[151] S. Marrone, A. Colagrossi, V. Baudry, and D. Le Touzé. Extreme wave impacts
on a wave energy converter: load prediction through a sph model. *Coastal
Engineering Journal*, 61(1):63–77, 2019.

[152] S. Marrone, A. Colagrossi, D. Le Touzé, and G. Graziani. Fast free-surface detection and level-set function definition in sph solvers. *Journal of Computational Physics*, 229(10):3652–3663, 2010.

[153] S. Marrone, A. Colagrossi, J. Park, and E. Campana. Challenges on the numerical prediction of slamming loads on lng tank insulation panels. *Ocean Engineering*, 141:512–530, 2017.

[154] S. Marrone, A. Di Mascio, and D. Le Touzé. Coupling of smoothed particle hydrodynamics with finite volume method for free-surface flows. *Journal of Computational Physics*, 310:161–180, 2016.

[155] A. Mayrhofer, M. Ferrand, C. Kassiotis, D. Violeau, and F.-X. Morel. Unified semi-analytical wall boundary conditions in sph: analytical extension to 3-d. *Numerical Algorithms*, 68:15–34, 2015.

[156] A. Mayrhofer, D. Laurence, B. D. Rogers, and D. Violeau. Dns and les of 3-d wall-bounded turbulence using smoothed particle hydrodynamics. *Computers and Fluids*, 115:86–97, 2015.

[157] F. Menter. Zonal two equation kw turbulence models for aerodynamic flows. In *23rd Fluid Dynamics, Plasmadynamics, and Lasers Conference*, page 2906, 1993.

[158] D. D. Meringolo, Y. Liu, X.-Y. Wang, and A. Colagrossi. Energy balance during generation, propagation and absorption of gravity waves through the δ-les-sph model. *Coastal Engineering*, 140:355–370, 2018.

[159] R. Mittal and G. Iaccarino. Immersed boundary methods. *Annual Review of Fluid Mechanics*, 37:239–261, 2005.

[160] R. Mittal and F. Najjar. Vortex dynamics in the sphere wake. In *30th Fluid Dynamics Conference*, page 3806, 1999.

[161] P. Moin and J. Kim. Numerical investigation of turbulent channel flow. *Journal of Fluid Mechanics*, 118:341–377, 1982.

[162] D. Molteni and A. Colagrossi. A simple procedure to improve the pressure evaluation in hydrodynamic context using the sph. *Computer Physics Communications*, 180(6):861–872, 2009.

[163] J. Monaghan and A. Kocharyan. Sph simulation of multi-phase flow. *Computer Physics Communications*, 87(1-2):225–235, 1995.

[164] J. J. Monaghan. Smoothed particle hydrodynamics. *Annual Review of Astronomy and Astrophysics*, 30(1):543–574, 1992.

[165] J. J. Monaghan. Simulating free surface flows with sph. *Journal of Computational Physics*, 110(2):399–406, 1994.

[166] J. J. Monaghan. Sph compressible turbulence. *Monthly Notices of the Royal Astronomical Society*, 335(3):843–852, 2002.

[167] J. J. Monaghan. Smoothed particle hydrodynamics. *Reports on Progress in Physics*, 68(8):1703, 2005.

[168] J. J. Monaghan. A turbulence model for smoothed particle hydrodynamics. *European Journal of Mechanics-B/Fluids*, 30(4):360–370, 2011.

[169] J. J. Monaghan. Sph-ε simulation of 2d turbulence driven by a moving cylinder. *European Journal of Mechanics-B/Fluids*, 65:486–493, 2017.

[170] J. J. Monaghan and J. B. Kajtar. Sph particle boundary forces for arbitrary boundaries. *Computer Physics Communications*, 180(10):1811–1820, 2009.

[171] J. J. Monaghan and A. Kos. Solitary waves on a cretan beach. *Journal of Waterway, Port, Coastal, and Ocean Engineering*, 125(3):145–155, 1999.

[172] N. Moreno, P. Vignal, J. Li, and V. M. Calo. Multiscale modeling of blood flow: coupling finite elements with smoothed dissipative particle dynamics. *Procedia Computer Science*, 18:2565–2574, 2013.

[173] J. P. Morris, P. J. Fox, and Y. Zhu. Modeling low reynolds number incompressible flows using sph. *Journal of Computational Physics*, 136(1):214–226, 1997.

[174] G. Murante, S. Borgani, R. Brunino, and S.-H. Cha. Hydrodynamic simulations with the godunov smoothed particle hydrodynamics. *Monthly Notices of the Royal Astronomical Society*, 417(1):136–153, 2011.

[175] A. Muta and P. Ramachandran. Efficient and accurate adaptive resolution for weakly-compressible sph. *Computer Methods in Applied Mechanics and Engineering*, 395:115019, 2022.

[176] A. Nasar, B. D. Rogers, A. Revell, and P. Stansby. Flexible slender body fluid interaction: vector-based discrete element method with eulerian smoothed particle hydrodynamics. *Computers and Fluids*, 179:563–578, 2019.

[177] A. M. Nasar, G. Fourtakas, S. J. Lind, J. King, B. D. Rogers, and P. K. Stansby. High-order consistent sph with the pressure projection method in 2-d and 3-d. *Journal of Computational Physics*, 444:110563, 2021.

[178] A. M. Nasar, G. Fourtakas, S. J. Lind, B. D. Rogers, P. Stansby, and J. King. High-order velocity and pressure wall boundary conditions in eulerian incompressible sph. *Journal of Computational Physics*, 434:109793, 2021.

[179] R. Natarajan and A. Acrivos. The instability of the steady flow past spheres and disks. *Journal of Fluid Mechanics*, 254:323–344, 1993.

[180] B. Nayroles, G. Touzot, and P. Villon. Generalizing the finite element method: diffuse approximation and diffuse elements. *Computational Mechanics*, 10(5):307–318, 1992.

[181] W. F. Noh and P. Woodward. Slic (simple line interface calculation). In *Proceedings of the fifth international conference on numerical methods in fluid dynamics June 28–July 2, 1976 Twente University, Enschede*, pages 330–340. Springer, 2005.

[182] A. M. Oboukhov. Some specific features of atmospheric tubulence. *Journal of Fluid Mechanics*, 13(1):77–81, 1962.

[183] R. Oechslin, S. Rosswog, and F.-K. Thielemann. Conformally flat smoothed particle hydrodynamics application to neutron star mergers. *Physical Review D*, 65(10):103005, 2002.

[184] G. Oger, M. Doring, B. Alessandrini, and P. Ferrant. Two-dimensional sph simulations of wedge water entries. *Journal of Computational Physics*, 213(2):803–822, 2006.

[185] G. Oger, M. Doring, B. Alessandrini, and P. Ferrant. An improved sph method: Towards higher order convergence. *Journal of Computational Physics*, 225(2):1472–1492, 2007.

[186] G. Oger, P.-M. Guilcher, E. Jacquin, L. Brosset, J.-B. Deuff, and D. Le Touzé. Simulations of hydro-elastic impacts using a parallel sph model. In *The Nineteenth International Offshore and Polar Engineering Conference*. OnePetro, 2009.

[187] G. Oger, S. Marrone, D. Le Touzé, and M. de Leffe. SPH accuracy improvement through the combination of a quasi-Lagrangian shifting transport velocity and consistent ALE formalisms. *Journal of Computational Physics*, 313:76–98, 2016.

[188] P. Omidvar, P. K. Stansby, and B. D. Rogers. Wave body interaction in 2d using smoothed particle hydrodynamics (sph) with variable particle mass. *International Journal for Numerical Methods in Fluids*, 68(6):686–705, 2012.

[189] P. Omidvar, P. K. Stansby, and B. D. Rogers. Sph for 3d floating bodies using variable mass particle distribution. *International Journal for Numerical Methods in Fluids*, 72(4):427–452, 2013.

[190] S. Osher and R. P. Fedkiw. Level set methods: an overview and some recent results. *Journal of Computational Physics*, 169(2):463–502, 2001.

[191] J. O'Connor and B. D. Rogers. A fluid–structure interaction model for free-surface flows and flexible structures using smoothed particle hydrodynamics on a gpu. *Journal of Fluids and Structures*, 104:103312, 2021.

[192] A. N. Parshikov and S. A. Medin. Smoothed particle hydrodynamics using inter-particle contact algorithms. *Journal of Computational Physics*, 180(1):358–382, 2002.

[193] C. S. Peskin. Flow patterns around heart valves: a numerical method. *Journal of Computational Physics*, 10(2):252–271, 1972.

[194] A. Placzek, J.-F. Sigrist, and A. Hamdouni. Numerical simulation of an oscillating cylinder in a cross-flow at low reynolds number: Forced and free oscillations. *Computers and Fluids*, 38(1):80–100, 2009.

[195] P. Ploumhans, G. Winckelmans, J. K. Salmon, A. Leonard, and M. Warren. Vortex methods for direct numerical simulation of three-dimensional bluff body flows: application to the sphere at re= 300, 500, and 1000. *Journal of Computational Physics*, 178(2):427–463, 2002.

[196] S. B. Pope. *Turbulent Flows*. Cambridge University Press, 2000.

[197] D. Price and J. J. Monaghan. Smoothed particle magnetohydrodynamics–i. algorithm and tests in one dimension. *Monthly Notices of the Royal Astronomical Society*, 348(1):123–138, 2004.

[198] D. J. Price. Smoothed particle hydrodynamics and magnetohydrodynamics. *Journal of Computational Physics*, 231(3):759–794, 2012.

[199] N. J. Quinlan, M. Basa, and M. Lastiwka. Truncation error in mesh-free particle methods. *International Journal for Numerical Methods in Engineering*, 66(13):2064–2085, 2006.

[200] A. Rafiee, S. Cummins, M. Rudman, and K. Thiagarajan. Comparative study on the accuracy and stability of sph schemes in simulating energetic free-surface flows. *European Journal of Mechanics-B/Fluids*, 36:1–16, 2012.

[201] A. Rafiee and K. P. Thiagarajan. An sph projection method for simulating fluid-hypoelastic structure interaction. *Computer Methods in Applied Mechanics and Engineering*, 198(33-36):2785–2795, 2009.

[202] P. W. Randles and L. D. Libersky. Smoothed particle hydrodynamics: Some recent improvements and applications. *Computer Methods in Applied Mechanics and Engineering*, 1996.

[203] P. Rastelli, R. Vacondio, J. Marongiu, G. Fourtakas, and B. D. Rogers. Implicit iterative particle shifting for meshless numerical schemes using kernel basis functions. *Computer Methods in Applied Mechanics and Engineering*, 393:114716, 2022.

[204] Y. Reyes López, D. Roose, and C. Recarey Morfa. Dynamic particle refinement in sph: application to free surface flow and non-cohesive soil simulations. *Computational Mechanics*, 51(5):731–741, 2013.

164

[205] O. Reynolds. Xxix. an experimental investigation of the circumstances which determine whether the motion of water shall be direct or sinuous, and of the law of resistance in parallel channels. *Philosophical Transactions of the Royal society of London*, (174):935–982, 1883.

[206] L. F. Richardson. *Weather Prediction by Numerical Process*. University Press, 1922.

[207] W. J. Rider and D. B. Kothe. Reconstructing volume tracking. *Journal of Computational Physics*, 141(2):112–152, 1998.

[208] M. Robinson and J. J. Monaghan. Direct numerical simulation of decaying two-dimensional turbulence in a no-slip square box using smoothed particle hydrodynamics. *International Journal for Numerical Methods in Fluids*, 70(1):37–55, 2012.

[209] R. S. Rogallo. *Numerical experiments in homogeneous turbulence*, volume 81315. National Aeronautics and Space Administration, 1981.

[210] B. D. Rogers, R. A. Dalrymple, and P. K. Stansby. Simulation of caisson breakwater movement using 2-d sph. *Journal of Hydraulic Research*, 48(sup1):135–141, 2010.

[211] R. Rook, M. Yildiz, and S. Dost. Modeling transient heat transfer using sph and implicit time integration. *Numerical Heat Transfer, Part B: Fundamentals*, 51(1):1–23, 2007.

[212] C. Rosales and C. Meneveau. Linear forcing in numerical simulations of isotropic turbulence: Physical space implementations and convergence properties. *Physics of fluids*, 17(9):095106, 2005.

[213] S. G. Saddoughi and S. V. Veeravalli. Local isotropy in turbulent boundary layers at high reynolds number. *Journal of Fluid Mechanics*, 268:333–372, 1994.

[214] P. Sagaut. *Large eddy simulation for incompressible flows: an introduction*. Springer Science and Business Media, Berlin, Germany, 2005.

[215] H. Sakamoto and H. Haniu. A Study on Vortex Shedding From Spheres in a Uniform Flow. *Journal of Fluids Engineering*, 112(4):386–392, 12 1990.

[216] M. Schaller et al. SWIFT: SPH With Inter-dependent Fine-grained Tasking. Astrophysics Source Code Library, May 2018.

[217] S. Shahriari, H. Maleki, I. Hassan, and L. Kadem. Evaluation of shear stress accumulation on blood components in normal and dysfunctional bileaflet mechanical heart valves using smoothed particle hydrodynamics. *Journal of Biomechanics*, 45(15):2637–2644, 2012.

[218] J. Shao, H. Li, G. Liu, and M. Liu. An improved sph method for modeling liquid sloshing dynamics. *Computers and Structures*, 100:18–26, 2012.

[219] S. Shao. Incompressible sph simulation of wave breaking and overtopping with turbulence modelling. *International Journal for Numerical Methods in Fluids*, 50(5):597–621, 2006.

[220] S. Shao. Simulation of breaking wave by sph method coupled with k-ε model. *Journal of Hydraulic Research*, 44(3):338–349, 2006.

[221] S. Shao and E. Y. Lo. Incompressible sph method for simulating newtonian and non-newtonian flows with a free surface. *Advances in Water Resources*, 26(7):787–800, 2003.

[222] N. Sharma and T. K. Sengupta. Vorticity dynamics of the three-dimensional taylor-green vortex problem. *Physics of Fluids*, 31(3):035106, 2019.

[223] Y. Shi, X. X. Zhu, M. Ellero, and N. A. Adams. Analysis of interpolation schemes for the accurate estimation of energy spectrum in Lagrangian methods. *Computers and Fluids*, 2013.

[224] K. Shibata, S. Koshizuka, T. Matsunaga, and I. Masaie. The overlapping particle technique for multi-resolution simulation of particle methods. *Computer Methods in Applied Mechanics and Engineering*, 325:434–462, 2017.

[225] Y. Shimizu, A. Khayyer, H. Gotoh, and K. Nagashima. An enhanced multiphase isph-based method for accurate modeling of oil spill. *Coastal Engineering Journal*, 62(4):625–646, 2020.

[226] C.-W. Shu, W.-S. Don, D. Gottlieb, O. Schilling, and L. Jameson. Numerical convergence study of nearly incompressible, inviscid taylor–green vortex flow. *Journal of Scientific Computing*, 24(1):1–27, 2005.

[227] M. Sinnott, P. W. Cleary, and M. Prakash. An investigation of pulsatile blood flow in a bifurcation artery using a grid-free method. In *Proc. Fifth International Conference on CFD in the Process Industries*, pages 1–6, 2006.

[228] A. Skillen, S. Lind, P. K. Stansby, and B. D. Rogers. Incompressible smoothed particle hydrodynamics (sph) with reduced temporal noise and generalised fickian smoothing applied to body–water slam and efficient wave–body interaction. *Computer Methods in Applied Mechanics and Engineering*, 265:163–173, 2013.

[229] A. Souto-Iglesias, L. Delorme, L. Pérez-Rojas, and S. Abril-Pérez. Liquid moment amplitude assessment in sloshing type problems with smooth particle hydrodynamics. *Ocean Engineering*, 33(11-12):1462–1484, 2006.

[230] A. Souto-Iglesias, F. Macià, L. M. González, and J. L. Cercos-Pita. On the consistency of mps. *Computer Physics Communications*, 184(3):732–745, 2013.

[231] A. Souto-Iglesias, F. Macià, L. M. González, and J. L. Cercos-Pita. Addendum to "on the consistency of mps"[comput. phys. comm. 184 (3)(2013) 732–745]. *Computer Physics Communications*, 185(2):595–598, 2014.

[232] P. R. Spalart. Strategies for turbulence modelling and simulations. *International Journal of Heat and Hluid Hlow*, 21(3):252–263, 2000.

[233] V. Springel. The cosmological simulation code gadget-2. *Monthly Notices of the Royal Astronomical Society*, 364(4):1105–1134, 2005.

[234] V. Springel and L. Hernquist. Cosmological smoothed particle hydrodynamics simulations: a hybrid multiphase model for star formation. *Monthly Notices of the Royal Astronomical Society*, 339(2):289–311, 2003.

[235] P. Sun, A. Colagrossi, S. Marrone, M. Antuono, and A. Zhang. Multi-resolution delta-plus-sph with tensile instability control: Towards high reynolds number flows. *Computer Physics Communications*, 224:63–80, 2018.

[236] P. Sun, A.-M. Zhang, S. Marrone, and F. Ming. An accurate and efficient sph modeling of the water entry of circular cylinders. *Applied Ocean Research*, 72:60–75, 2018.

[237] P. N. Sun, A. Colagrossi, S. Marrone, M. Antuono, and A. M. Zhang. A consistent approach to particle shifting in the δ-Plus-SPH model. *Computer Methods in Applied Mechanics and Engineering*, 348:912–934, may 2019.

[238] A. Tafuni, J. Domínguez, R. Vacondio, and A. Crespo. A versatile algorithm for the treatment of open boundary conditions in smoothed particle hydrodynamics gpu models. *Computer Methods in Applied Mechanics and Engineering*, 342:604–624, 2018.

[239] N. Tanaka and T. Takano. Microscopic-scale simulation of blood flow using sph method. *International Journal of Computational Methods*, 2(04):555–568, 2005.

[240] S. Taneda. Experimental investigation of the wake behind a sphere at low reynolds numbers. *Journal of the Physical Society of Japan*, 11(10):1104–1108, 1956.

[241] F.-B. Tian, H. Dai, H. Luo, J. F. Doyle, and B. Rousseau. Fluid–structure interaction involving large deformations: 3d simulations and applications to biological systems. *Journal of Computational Physics*, 258:451–469, 2014.

[242] A. G. Tomboulides and S. A. Orszag. Numerical investigation of transitional and weak turbulent flow past a sphere. *Journal of Fluid Mechanics*, 416:45–73, 2000.

[243] G. Tryggvason, R. Scardovelli, and S. Zaleski. *Direct numerical simulations of gas–liquid multiphase flows*. Cambridge university press, Cambridge, UK, 2011.

[244] S. O. Unverdi and G. Tryggvason. A front-tracking method for viscous, incompressible, multi-fluid flows. *Journal of Computational Physics*, 100(1):25–37, 1992.

[245] R. Vacondio, C. Altomare, M. De Leffe, X. Hu, D. Le Touzé, S. Lind, J.-C. Marongiu, S. Marrone, B. D. Rogers, and A. Souto-Iglesias. Grand challenges for smoothed particle hydrodynamics numerical schemes. *Computational Particle Mechanics*, 8(3):575–588, 2021.

[246] R. Vacondio, B. Rogers, and P. Stansby. Smoothed particle hydrodynamics: Approximate zero-consistent 2-d boundary conditions and still shallow-water tests. *International Journal for Numerical Methods in Fluids*, 69(1):226–253, 2012.

[247] R. Vacondio, B. Rogers, P. Stansby, and P. Mignosa. Sph modeling of shallow flow with open boundaries for practical flood simulation. *Journal of Hydraulic Engineering*, 138(6):530–541, 2012.

[248] R. Vacondio, B. Rogers, and P. K. Stansby. Accurate particle splitting for smoothed particle hydrodynamics in shallow water with shock capturing. *International Journal for Numerical Methods in Fluids*, 69(8):1377–1410, 2012.

[249] R. Vacondio, B. D. Rogers, P. Stansby, P. Mignosa, and J. Feldman. Variable resolution for sph: a dynamic particle coalescing and splitting scheme. *Computer Methods in Applied Mechanics and Engineering*, 256:132–148, 2013.

[250] R. Vacondio, B. D. Rogers, P. K. Stansby, and P. Mignosa. Variable resolution for sph in three dimensions: Towards optimal splitting and coalescing for dynamic adaptivity. *Computer Methods in Applied Mechanics and Engineering*, 300:442–460, 2016.

[251] A. Valizadeh and J. J. Monaghan. Sph simulation of 2d turbulence driven by a cylindrical stirrer. *European Journal of Mechanics-B/Fluids*, 51:44–53, 2015.

[252] G. D. Van Albada, B. Van Leer, and W. Roberts. A comparative study of computational methods in cosmic gas dynamics. In *Upwind and high-resolution schemes*, pages 95–103. Springer, 1997.

[253] W. M. Van Rees, A. Leonard, D. I. Pullin, and P. Koumoutsakos. A comparison of vortex and pseudo-spectral methods for the simulation of periodic vortical flows at high reynolds numbers. *Journal of Computational Physics*, 230(8):2794–2805, 2011.

[254] R. Verzicco. Immersed boundary methods: Historical perspective and future outlook. *Annual Review of Fluid Mechanics*, 55, 2023.

[255] J. P. Vila. On particle weighted methods and smooth particle hydrodynamics. *Mathematical Models and Methods in Applied Sciences*, 9(02):161–209, 1999.

[256] D. Violeau. *Fluid mechanics and the SPH method: theory and applications.* Oxford University Press, Oxford, UK, 2012.

[257] D. Violeau and R. Issa. Numerical modelling of complex turbulent free-surface flows with the sph method: an overview. *International Journal for Numerical Methods in Fluids*, 53(2):277–304, 2007.

[258] D. Violeau, S. Piccon, and J.-P. Chabard. Two attempts of turbulence modelling in smoothed particle hydrodynamics. In *Advances in Fluid Modeling and Turbulence Measurements*, pages 339–346. World Scientific, 2002.

[259] D. Violeau and B. D. Rogers. Smoothed particle hydrodynamics (sph) for free-surface flows: past, present and future. *Journal of Hydraulic Research*, 54(1):1–26, 2016.

[260] D. Wang and P. L.-F. Liu. An isph with k–ε closure for simulating turbulence under solitary waves. *Coastal Engineering*, 157:103657, 2020.

[261] D. Wang and P. L.-F. Liu. An isph with modified k–ε closure for simulating breaking periodic waves. *Coastal Engineering*, 178:104191, 2022.

[262] P.-P. Wang, Z.-F. Meng, A.-M. Zhang, F.-R. Ming, and P.-N. Sun. Improved particle shifting technology and optimized free-surface detection method for free-surface flows in smoothed particle hydrodynamics. *Computer Methods in Applied Mechanics and Engineering*, 357:112580, 2019.

[263] Z. Wei and R. A. Dalrymple. Numerical study on mitigating tsunami force on bridges by an sph model. *Journal of Ocean Engineering and Marine Energy*, 2:365–380, 2016.

[264] Z. Wei, R. A. Dalrymple, A. Hérault, G. Bilotta, E. Rustico, and H. Yeh. Sph modeling of dynamic impact of tsunami bore on bridge piers. *Coastal Engineering*, 104:26–42, 2015.

[265] H. Wendland. Piecewise polynomial, positive definite and compactly supported radial functions of minimal degree. *Advances in Computational Mathematics*, 4(1):389–396, 1995.

[266] D. C. Wilcox. Reassessment of the scale-determining equation for advanced turbulence models. *AIAA journal*, 26(11):1299–1310, 1988.

[267] C. H. Williamson. Vortex dynamics in the cylinder wake. *Annual Review of Fluid Mechanics*, 28(1):477–539, 1996.

[268] C. H. Williamson and A. Roshko. Vortex formation in the wake of an oscillating cylinder. *Journal of Fluids and Structures*, 2(4):355–381, 1988.

[269] J.-S. Wu and G. M. Faeth. Sphere wakes in still surroundings at intermediate reynolds numbers. *AIAA Journal*, 31(8):1448–1455, 1993.

[270] K. Wu, D. Yang, and N. Wright. A coupled sph-dem model for fluid-structure interaction problems with free-surface flow and structural failure. *Computers and Structures*, 177:141–161, 2016.

[271] Q. Yang, V. Jones, and L. McCue. Free-surface flow interactions with deformable structures using an sph–fem model. *Ocean Engineering*, 55:136–147, 2012.

[272] X. Yang and S.-C. Kong. Smoothed particle hydrodynamics method for evaporating multiphase flows. *Physical Review E*, 96(3):033309, 2017.

[273] X. Yang and S.-C. Kong. Adaptive resolution for multiphase smoothed particle hydrodynamics. *Computer Physics Communications*, 239:112–125, 2019.

[274] X. Yang, S.-C. Kong, M. Liu, and Q. Liu. Smoothed particle hydrodynamics with adaptive spatial resolution (sph-asr) for free surface flows. *Journal of Computational Physics*, 443:110539, 2021.

[275] T. Ye, R. Mittal, H. Udaykumar, and W. Shyy. An accurate cartesian grid method for viscous incompressible flows with complex immersed boundaries. *Journal of Computational Physics*, 156(2):209–240, 1999.

[276] S.-C. Yoon, P. Podsiadlowski, and S. Rosswog. Remnant evolution after a carbon–oxygen white dwarf merger. *Monthly Notices of the Royal Astronomical Society*, 380(3):933–948, 2007.

[277] Y. You, A. Khayyer, X. Zheng, H. Gotoh, and Q. Ma. Enhancement of δ-sph for ocean engineering applications through incorporation of a background mesh scheme. *Applied Ocean Research*, 110:102508, 2021.

[278] Y. L. Young. Fluid–structure interaction analysis of flexible composite marine propellers. *Journal of Fluids and Structures*, 24(6):799–818, 2008.

[279] L. Zhan, C. Peng, B. Zhang, and W. Wu. A stabilized tl–wc sph approach with gpu acceleration for three-dimensional fluid–structure interaction. *Journal of Fluids and Structures*, 86:329–353, 2019.

[280] A.-m. Zhang, P.-n. Sun, F.-r. Ming, and A. Colagrossi. Smoothed particle hydrodynamics and its applications in fluid-structure interactions. *Journal of Hydrodynamics, Ser. B*, 29(2):187–216, 2017.

[281] C. Zhang, M. Rezavand, and X. Hu. A multi-resolution sph method for fluid-structure interactions. *Journal of Computational Physics*, 429:110028, 2021.

[282] D. Zhang, Y. Shi, C. Huang, Y. Si, B. Huang, and W. Li. Sph method with applications of oscillating wave surge converter. *Ocean Engineering*, 152:273–285, 2018.

[283] Q. Zhu, L. Hernquist, and Y. Li. Numerical convergence in smoothed particle hydrodynamics. *The Astrophysical Journal*, 800(1):6, 2015.

[284] O. Zienkiewicz, R. Taylor, and P. Nithiarasu, editors. *The Finite Element Method for Fluid Dynamics*. Butterworth-Heinemann, Oxford, seventh edition edition, 2014.